Atomic Contacts characterized by Force and Current

Till Hagedorn

Department of Physics
McGill University
Montréal, Québec, Canada
August 2010

A thesis submitted to McGill University
in partial fulfilment of the requirements of the degree of
Doctor of Philosophy

© Till Hagedorn, 2010

Acknowledgements

These past years in Montreal have been more than I expected. I had the opportunity to learn a lot about myself, the world of physics and Canada. A huge part of this experience were the people I meet and worked with.

First and foremost my thank goes to Peter Grütter my supervisor who always supported me while traveling this rocky road towards the PhD and gave me the opportunity to follow my interests.

Mehdi El Ouali has been there along the way to get the experiment to work and acquire relevant data, thank you for your skilled work on the machine and all the hours of applying your superb programming skills to the data acquisition of the experiment, not forgetting going through the troubles of Au sample preparation.

I would like to thank Yoichi Miyahara for his guidance in SPM related designes, repairs and visionary ideas regarding interesting experiments that explore exciting physics. Besides his incredible knowledge of SPM, the mental support in really hard times when the appearance of discharges and strange signals did not want to end was incredibly crucial to the success of this thesis.

A big thank you goes to William Paul and David Oliver for giving the system new life and me excellent feedback for the study that is presented here. Good luck for future experiments with the system.

Many people in the group or related to the group did support the work that is presented here. The department is really vivid and everyone is approachable if problems or questions occur. Special thanks in that regard go to Antoine Roy-Gobeil who translated my abstract into French on short term notice.

Nothing works without support and the support by Robert Gagnon and Jon Smeros was outstanding regarding preparation, maintenance and other things that came up in the

context of experiments. Thanks for your reliable, quick and qualified help!

Steve Kecani, Eddie del Campo, and Pascal Bourseguin showed me how to turn a piece of metal into something that can be a crucial part of a measurement. Thank you for explaining and being an excellent source for information regarding any kind of machining problem.

I would like to thank André Schirmeisen, who supervised my diploma thesis, for creating such a nice research environment in his group that I decided to pursue a PhD in physics and came to McGill. Thank you for your continuing support which was key to stay on track for this research project.

Rolf Möller's work on the system during his three month stay at McGill improved not only the system operation in many ways but also my knowledge of SPM techniques, possible experiments and my understanding of their physical nature. Thank you for the continued interest in the work that is done on the FIM-STM/AFM and the fruitful exchange of ideas.

My experience in Montreal would have been less enjoyable if if hadn't been for a bunch of people I met around the department. These people helped me to get through tough times and added to my life. Thank you!

Janna, I would like to thank you for being patient with me and giving me support whenever needed. Thank you for waiting.

Last but not least, my parents have been there all the way – they might be happy that I am finally completing my studies but they never hesitated to support me. Danke!

Abstract

Contacts between atoms present the reduction of an electronic system to the smallest scale accessible at the present. Field ion microscopy (FIM) and simultaneous scanning tunneling microscopy (STM) and atomic force microscopy (AFM) were used to characterize atomic contacts between a tungsten (W(111)) STM-tip and a gold (Au(111)) sample. The STM-tip was imaged with atomic resolution using FIM and reconstructed in a three dimensional ball model. Force and current were measured simultaneously while the tip approached an atomically flat Au(111) sample to form a contact.

A detailed description of the tip production and characterization using an etching setup that was developed for this thesis is introduced. These tips are characterized by field ion microscopy (FIM). The adaptation of a well known three dimensional ball model reconstruction to the tungsten bcc(111) crystal is described and utilized to reconstruct FIM micrographs of W(111) STM-tips. Using several of such tips, the long-range forces of the tip-sample system were analyzed using recent theoretical models, concluding that van der Waals and electrostatic force contributions were negligible for tips with a radius smaller than $r_{tip} = 15$ nm within the precision of the FIM-STM/AFM system that was employed for the experiments.

Force and current data for different structural modifications of the W(111)-Au(111) SPM tunneling junction are presented and discussed. Findings include that the W-Au junction in geometries which were examined in this thesis do not exhibit the conductive properties of a one-atom contact.

A comparison of different theoretical approaches that treat the correlation of force and current in a STM type tunneling junction is presented and the results of this thesis support a $F^2 \propto I_t$ proportionality for a three-atom tungsten tip contacting an atomically flat Au(111) sample.

Résumé

Un contact entre atomes est la réduction d'un système électronique la plus petite échelle actuellement accessible. La microscopie champ ionique (field ion microscopy, FIM) et la microscopie effet tunnel (scanning tunneling microscopy, STM) simultanément la microscopie forces atomiques (atomic force microscopy, AFM) ont été utilisées pour caractériser le contact atomique entre une pointe de tungstène (W(111)), un palpeur pour le STM, et un échantillon d'or (Au(111)). La pointe a été imagée par FIM avec une résolution atomique et reconstruite par un modèle de balle tridimensionnel. La force et le courant ont été mesurés simultanément pendant que la pointe s'approchait de l'échantillon d'or (111) atomiquement plat pour y former un contact.

Une description détaillée de la production et de la caractérisation des pointes par l'utilisation d'un système dattaque électrolytique, développé pour cette thèse, est présentée. L'adaptation de la reconstruction par modèle de balle tridimensionnel au cristal de tungstène ccc(111) est décrite, puis utilisée pour reconstruire les pointes W(111). En utilisant plusieurs de ces pointes, les forces longue portée du système pointe-échantillon ont été analysées en utilisant de récents modèles théoriques, ce qui a permit de conclure que les contributions des forces de van der Waals et des forces électrostatiques sont négligeables pour des pointes de rayon inférieur $r_{pointe} = 15$ nm, compte tenu de la précision du système FIM-STM/AFM employé pour les expériences.

En lien avec les simulations qui prennent en compte les forces d'interaction pointe-échantillon et les propriétés conductrices de la séparation des contacts, des données de force et de courant pour différentes modifications structurelles de la jonction tunnel W(111)-Au(111) sont présentées et analysées. Entre autres choses, il est montré que la jonction W-Au, pour les géométries étudiées dans cette thèse, ne présente pas les propriétés conductrices d'un contact monoatomique.

En comparant différentes approches théoriques qui traitent de la corrélation entre la force et le courant dans une jonction tunnel de type STM, les données pour la jonction W(111)-Au(111) sont mises en relation avec ces lois de puissance. Les résultats de cette thèse indique une proportionnalité $F^2 \propto I_t$ pour une pointe de tungstène 3 atomes faisant contact avec un échantillon dor (111) atomiquement plat.

Statement of Originality

The work presented in this thesis constitute original scholarship and demonstrate a distinct contribution to knowledge. The elements of that contribution are listed below sectioned into the experimental aspects and measured data and its interpretation.

Experimental Setup

- A coarse approach mechanism which is shown in appendix C was designed and implemented based on past group experiences and adapted to the specifics of the FIM-STM/AFM setup. This device is used for about four years now, and proved to be reliable in long term usage.

- The design of a new etching container that improves the quality and reliability of the STM-tip preparation of tips with radii smaller than $r_{tip} = 15$ nm was developed and implemented. Using this method ultra sharp single crystalline (111) oriented tungsten tips were produced with a 90 % yield as described in chapter 3.

Scientific Data

- W(111) STM tips with a radius smaller than $r_{tip} = 15$ nm were produced, characterized and used as electrode in order to form an atomic contact with an atomically flat Au(111) surface.

- The tip-sample force and electric conductivity was measured using three-atom W(111) tips and atomically flat Au(111) samples. The results were related to recent models and reference experiments of similar systems identifying characteristic deviations of the investigated three-atom W(111) STM tip from results that were obtained using trained tips. This motivates further theoretic modeling as presented in chapter 5.

- A change in the conductive behaviour of the tip-sample junction was induced by controlled indentation and characterized as tip training method using current, force and structural information. The results are given in chapter 5.3.

- A sequence of simultaneous force and current data recorded with a W(111) three-atom tip was related to Hofer's, Chan's and Jelinek's scaling model as described in chapter 6, motivating a deeper theoretical treatment of the conductive properties of the investigated W(111)-Au(111) contact and supporting a $F^2 \propto I_t$ relation for the presented contact structure.

Table of Contents

Acknowledgements **i**

Abstract **iii**

Résumé **v**

Statement of Originality **vii**

List of Tables **xiii**

List of Figures **xv**

1 Introduction **1**

1.1 Physics of Atomic Contacts 1
1.2 Atomic Contacts and SPM 2
1.3 Potential for Atomic Contacts in Technology 3
1.4 Thesis Outline 4

2 Experimental Methods **7**

2.1 The UHV chamber 7
2.2 Simultaneous STM/AFM with FIM characterized tips 9
2.2.1 STM 11
2.2.2 AFM 12
2.2.3 Description of the Curve Parameters 14
2.3 The Sample: Au(111) Cantilever Samples 16
2.4 Raw Data and Data Processing 17
2.5 Piezo Properties: Approach Cycle, Creep and Drift 20
2.6 Measurement Uncertainties 21

3 The Probe: FIM characterized W(111) STM-Tips 27
3.1 Etching the tip 28
3.2 Cleaning the tip: Resistive Heating in UHV 33
3.3 Checking the tip radius and fine sharpening by field emission 35
3.3.1 Fowler-Nordheim theory for field emission 35
3.3.2 Refining the tip by annealing/field emission cycles 37
3.4 FIM: Imaging the tip structure at the atomic level 38
3.4.1 Working principle of the FIM 38
3.5 Reconstructing the atomic structure of the tip 47
3.5.1 Image interpretation 47
3.5.2 Image reconstruction 47
3.6 Realistic Tip–Sample Geometry 50

4 Forces, Conductivity and Relaxation 55
4.1 Forces and Relaxation 56
4.1.1 Electrostatic force 57
4.1.2 Van der Waals force 58
4.1.3 Short range forces 59
4.2 Forces in Experimental Data 64
4.2.1 Long range forces characterization 64
4.2.2 Short Range Scaling 67
4.3 Tunneling Current and Relaxation 68

5 Conductive States of the Tunneling Gap 73
5.1 W(111) Three Atom Tip 74
5.1.1 The Concept of Early and Late Tunneling 75
5.1.2 Conductive States of W(111)-Au(111) 77
5.2 Conductive States and STM/AFM Scanning 79
5.3 Contact Training – Switching Conductive States 81

6 Correlation of Force and Conductivity in the Tunneling Regime 89
6.1 Theoretical Models 90
6.1.1 Chen's model 90
6.1.2 Hofer's model 91
6.1.3 Comparative model by Jelinek 91
6.2 Experimental study: W(111)-Au(111) 92
6.2.1 Experimental Data 92
6.2.2 Discussion 95

7 Conclusion and Future Work **97**
7.1 Conclusion . . . 97
7.1.1 STM tips etched and prepared with FIM . . . 97
7.1.2 Atomic W(111)-Au(111) contact . . . 98
7.2 Future Work . . . 99
7.2.1 Tip preparation . . . 99
7.2.2 Atomic contacts . . . 100

References **103**

A Tip Reconstruction **115**
A.1 Construction of a bcc 111 oriented cube . . . 115
A.2 Construction of a bcc 110 oriented cube . . . 116
A.3 Construction of a fcc 111 oriented cube . . . 117
A.4 Tilt for a W(111) one atom tip . . . 117

B Electric Field and Electrostatic Force for two geometries **119**
B.1 Prolate Spheriodal Coordinates . . . 120
B.2 Sphere-Cone geometry . . . 124
B.3 Finite Element Analysis of the Electric Field in FIM . . . 126

C New SPM Coarse Approach **129**

List of Tables

3.1 Results for tips that were characterized with field emission. 32

4.1 Scaling length for different tip-sample systems 68

6.1 Experimental $F^n \propto I_t$ scaling values 96

List of Figures

1.1 Moore's law . . . 3

2.1 Photo of the UHV system . . . 8
2.2 Measurement Overview . . . 10
2.3 Schematic of the signal pathways of the STM/AFM apparatus . . . 11
2.4 Tip-sample separation concept . . . 12
2.5 Data presentation with and without TSS . . . 14
2.6 Presentation of curve parameters . . . 15
2.7 The Au(111) cantilever sample . . . 16
2.8 Filtering process for F and I_t . . . 18
2.9 Approach cycle and drift . . . 19
2.10 Error bar plot for F and I_t . . . 24

3.1 Tip etching setup . . . 29
3.2 Tip etching steps . . . 30
3.3 Tip etching data and tip heating . . . 33
3.4 Potential for field emission . . . 35
3.5 Field emission . . . 37
3.6 Field Ion Microscopy . . . 39
3.7 He ionization process and FIM magnification . . . 40
3.8 Tip modification by field evaporation . . . 42
3.9 FIM resolution . . . 44
3.10 Three dimensional ball modell reconstruction . . . 46
3.11 Tip atom selection . . . 48
3.12 Atomic contact geometry . . . 50
3.13 Tip apex orientation . . . 52
3.14 Tip tilt geometry . . . 53

4.1 Forces in scanning probe microscopy . . . 57
4.2 Cone-sphere geometry and calculated forces . . . 59

4.3 Calculations of force for SPM contacts 60
4.4 Calculations of current for W-Au and Al-Al 63
4.5 Long rang forces characterization for W-Au 65
4.6 Morse and Rydberg fit to experimental data 66
4.7 Simulation of the tunneling current 70

5.1 Ideal contact formation schematic 73
5.2 Early and late tunneling data 76
5.3 STM/AFM images in early and late tunneling conditions 80
5.4 Contact training sequence 84
5.5 Development of the ABH for contact training 87

6.1 $F \propto I_t$ scaling results 93

A.1 Geometry for bcc 111 structure 116
A.2 Geometry of bcc 110 and fcc 111 structures 117
A.3 Tilt for a one atom tip 118

B.1 Electric field for the hyperbolid geometry 120
B.2 Electric field for the cone-sphere geometry 124
B.3 Electric field for the cone-sphere geometry 127

C.1 New STM coarse approach. 130

CHAPTER 1

Introduction

1.1 Physics of Atomic Contacts

Ever since the optical microscope was invented in the early 17th century, mankind was fascinated by revelations that came with the magnification of small objects. The research of fundamental components of matter began in those days. About two hundred years later John Dalton among other scientists gave birth to the atomic theory and the idea that matter consists of stable indivisible parts, which were called atoms [1]. The structure of atoms has been probed by the pioneering work of Thomson [2], who revealed that electrons were parts of the atom, and Rutherford, who discovered the atomic nucleus in his famous scattering experiments [3]. Together with observations and theoretical explanations of phenomena like the photoelectric effect [4], this gave birth to quantum physics and the explanation of the structure and properties of matter.

Richard Feynman proposed in his famous lecture with the title "There's Plenty of Room at the Bottom" in 1959 [5] to use this knowledge and create a new kind of miniature science that would use molecular sized objects and their properties to generate devices with unprecedented precision and performance analogous to biological systems in nature.

If one contacts two pieces of matter, the smallest electrical contact that is achievable between the two should be formed between two atoms that bind and confine the electrical conduction to the "joint" between these two atoms. This thesis goes along these lines of thought, minimizing a contact structure to an atomically sharp tungsten tip with three atoms at the end and an atomically flat gold sample. Physical and chemical aspects of bond formation, electron tunneling and the local electronic properties of the atomic system of

tungsten and gold will be characterized by experimentally acquired force and conductivity data of the junction during contact formation.

1.2 Atomic Contacts and SPM

Since Binnig and Rohrer invented the scanning tunneling microscope (STM) in the early 1980s [6] and a few years later the atomic force microscope (AFM) [7], scanning probe microscopy (SPM) has become a widely used tool in surface science. From structure analysis of surface reconstructions [8] to three dimensional force maps [9], magnetic spectroscopy [10], and bond formation [11], many physical quantities and processes can be characterized with SPM tools [12]. Since the nature and sensitivity of the instrument is due to a measurement of probe and sample interaction, a great desire exists to localize this interaction to only one tip atom and an atomically defined sample structure in the ultimate case. Great resolution has been achieved in SPM by doing so. Molecular orbitals have been resolved in the case of STM [13] and AFM [14]. Resolving the sample structure with subatomic resolution is therefore not impossible anymore, but imaging the tip structure remains a difficult task and has only has only been achieved in special combinations of electron microscopy and SPM techniques [15], [16], [17] and [18]. This is one of the motivations of this thesis. Experiments that will be presented here, have atomic structure information about the tip acquired by field ion microscopy (FIM) before and after each sequence of SPM runs.

Another interesting aspect of SPM is that the simultaneous force and tunneling information reveals the interaction force and the electronic conduction of an atomic structure if the tip and the sample are brought into bonding range or into quantum contact. In the beginning of STM and AFM both interactions have been probed separately. Recently, more and more AFMs employ a tuning fork with an attached metal tip [19]. This gives the opportunity to measure force and current at the same time. A different approach has been used in this thesis, where a STM and AFM were combined in a static mode by using a conventional STM type setup and a flexible sample cantilever that measures the force interaction between tip and sample. This setup reveals simultaneously current and force information of the tip-sample junction. The structure of the tip-sample junction is evaluated with atomic precision using the structural information from FIM micrographs. Structural information of the sample is gained by scans of the surface. In this way the tip-sample contact geometry is evaluated and linked to the electrical conduction, namely the apparent barrier height (ABH), and compared to recent theoretical and experimental results of similar systems.

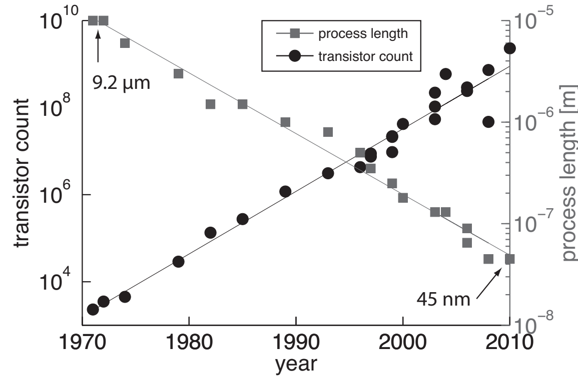

Figure 1.1 Moore's Law for the transistor count on a processor (black) and the process length of a single transistor (red). An exponential increase of transistor counts and therefore computing power is predicted by this law. The solid black line indicates an increase by a factor of 1.39 every year. In order to achieve this progress, the process length has to be decreased. An exponential decrease is seen in the feature size plot as well. The solid red line indicates a decrease by a factor 0.87 per year. (Source: public information on the official Intel, AMD and IBM websites).

1.3 Potential for Atomic Contacts in Technology

The feature size of the transistor that is used in a computer CPU has been miniaturized to tens of nano meters over the course of about four decades. Figure 1.1 shows a plot of Moore's law that predicts a logarithmic increase of the transistor count in a processor and the corresponding exponential decrease of the process length (the actual size of the MOSFET unit). It holds from the 1960s when the law was predicted until now; the actual length between source and drain has been made even smaller since. At the moment (2010) the process length is 45 nm for transistors in regular PCs. Extrapolating the current rate of feature size reduction, a theoretical length of 10 nm will be reached in the year 2022 and 1 nm in the year 2038. Besides fabrication issues, the main problem will be posed by the nature of the transport at these length scales [20], [21]. Quantum effects like tunneling leakage will play a role and the dependence on atomic structural precision will increase dramatically as the feature size decreases to atomic dimensions (Si lattice constant $a_{Si} = 5.4$ Å). Therefore a great interest exists to characterize electronic circuit structures of atomic scales (atom–atom distances) up to the size of molecular structures (few nanometers) in order to be prepared for phenomena and challenges that this length scale poses for technical applications.

Some hope was placed into the application of molecular electronics [22], where a single

molecule is utilized as active device. But the main challenge seems to be the realization of devices of true molecular nature. In the case of carbon nanotubes, success has been achieved and can be characterized with SEM to confirm the measured structure [23]. A scanning probe approach where the molecule of interest is contacted with a scanning tunneling microscope (STM) led to great success as well. Results for C_{60} [24],[25] and contacts to adatoms have been characterized in great detail [26]. In order to properly understand these devices, it is necessary to know the actual path of the current and the geometric configuration of the lead–molecule–lead structure, which is rarely straight forward. For example, the case of a stearic acid molecule deposited with the Langmuir-Blodgett technique between two metal nano–bars that was believed to be a measurement of the electrical properties of the sandwiched molecule [27]. The result turned out to be a measurement of the oxidation states of the metal–metal connection [28].[1]

The measurements of this thesis correlate structure and interaction of an atomic metal-metal contact and emphasize that small deviations in structure lead to a different conductive behaviour of the tip-sample contact. Further sources that need to be investigated are the chemical structure of each lead and the processes that occur during contact formation. Hybridization in the course of the binding process can cause a change in the initial electronic and chemical properties of each lead. These findings are essential if one wants to produce an electronic device of atomic nature with reproducible properties.

1.4 Thesis Outline

Atomic contacts were characterized using a combination of experimental techniques. An overview of all the used methods is given first in chapter 2. The unique combined STM/AFM in static mode is described along with an overview of the data acquisition and processing, concluding with an estimation of measurement uncertainties.

In chapter 3 the specifics of the probe preparation and analysis will be given. The challenges of producing and characterizing an atomically sharp tip are illustrated and followed by a three dimensional structure analysis of the crystallographic nature of the W(111) STM tip.

Forces involved in atomic scanning probe microscopy are described using recent theoretical models that take the atomic nature of the contact into account in chapter 4. These

[1] The realization finally led to the description of the device as a memristor or fourth fundamental circuit element [29].

methods are applied to experimental data that was recorded for the W(111)-Au(111) contact. Recent theoretic findings for SPM forces are then related to the conductive properties of the contact.

In chapter 5 details of the conductive signatures in the simultaneous force and current data for several different W(111)-Au(111) structures are presented and discussed.

A discussion about the relation of the force and current during contact formation is presented and then related to data of the W(111)-Au(111) tunneling junction in chapter 6.

The thesis concludes by summarizing the work and discussing potential future experiments based on the findings in this thesis.

CHAPTER 2

Experimental Methods

In this chapter a broad overview of the experimental techniques will be given. Since the STM tip preparation and characterization are in some way unique to the system and were a substantial part of the work that led to the experimental data, they will be described separately in chapter 3. Further details on the instrumentation can be found in [30], [31], [32] and [33].

2.1 The UHV chamber

All final preparation steps and the data acquisition were performed in a ultra high vacuum system (UHV) with a base pressure of $p \leq 10^{-10}$ mbar. A drawing of the UHV chamber is given in figure 2.1. In order to separate the preparation processes from the actual measurement, the system is divided into two parts, the preparation chamber and the measurement chamber. They are separated by a mechanical UHV valve. This is useful in terms of hindering the contamination of the measurement area with residues from the tip and sample preparation and in the case of a partial repair of the system. In that case, only the part that one wants to repair or maintain needs to be vented and opened.

In the preparation chamber, sputtering and annealing together with Auger electron spectroscopy (AES) equipment were used for the preparation of the sample. The tip was prepared using a custom built tip heating and field emission stage. Both the tip and the sample were made *ex-situ*. Furthermore a residual gas analyzer (RGA) measured the partial pressures of the rest gas components. The option of evaporating molecules onto the sample with a molecular beam evaporator (MBE) exists in the system but it was not used in the context of this thesis.

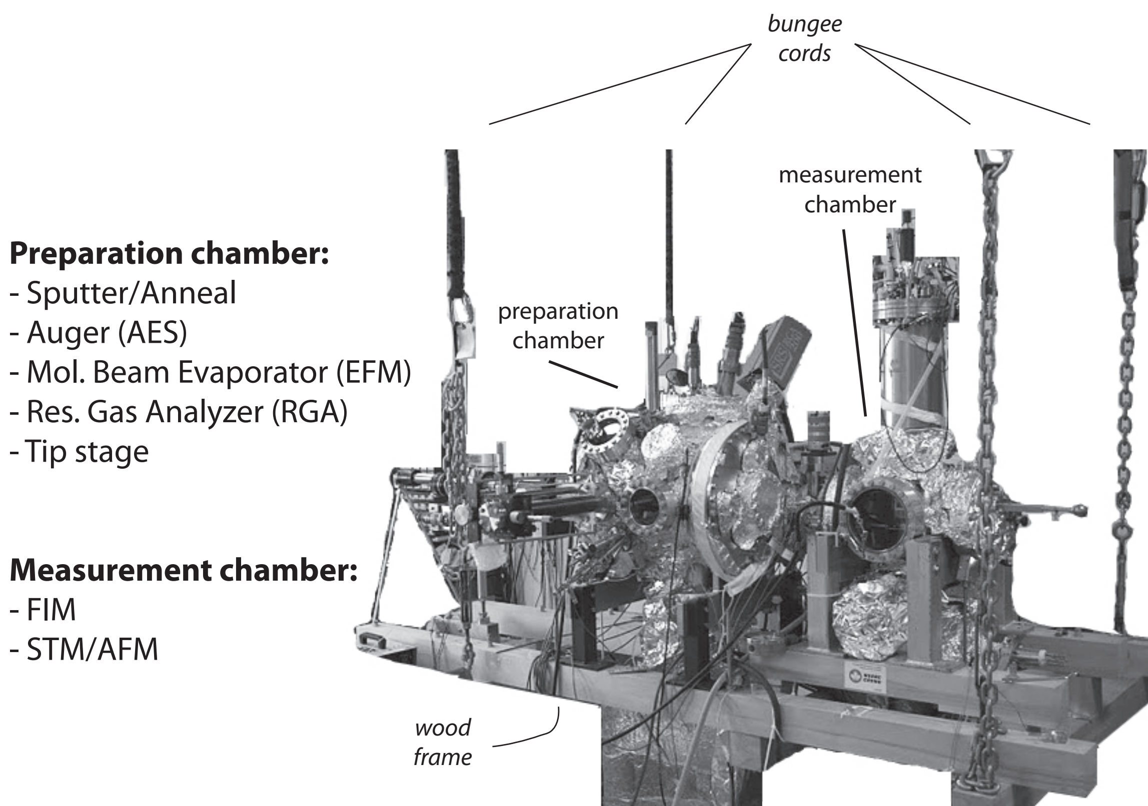

Figure 2.1 Photo of the UHV system. It consists of two chambers that contain the preparation features (preparation chamber) and the measurement equipment (measurement chamber). The instruments are listed on the left side of the figure. The system hangs from the ceiling supported by bungee cords while resting on a wood frame in order to be isolated from building vibrations.

The measurement chamber hosts the unique simultaneous scanning tunneling microscope/atomic force microscope with *in-situ* field ion microscope capability (FIM-STM/AFM system). The initial construction is described in [30] and recent modifications can be found in [32].

2.2 Simultaneous STM/AFM with FIM characterized tips

Figure 2.2 shows the two major components of the measurement. Before and after each experiment a field ion microscopy (FIM) image was taken (fig. 2.2 a)). In order to obtain a FIM micrograph the measurement chamber was flooded with 10^{-5} mbar of ultra pure He. A high voltage between the tip and a screen unit ionized the He gas atoms at the tip apex. The ionized He atoms were accelerated by the electric field towards the screen and produced an image on the screen (details in chapter 3). This image was used to reconstruct the 3D structure of the tip apex. In figure 2.2 b) a drawing of the STM/AFM operation is given. The sample that was placed aside during the FIM procedure is inserted and positioned under the STM tip. The interferometer signal measured the bending of the sample and therefore the force if the spring constant is known. As is common in scanning probe microscopy, the microscope was used in different modes. For example, images were acquired (inset (i)) and spectroscopy curves were taken (inset (ii)). The feedback used the tunneling current for the distance control.

The purpose of the experiments that were performed in the context of this thesis is to characterize atomic contacts formed by the STM tunneling gap of a clean W(111)–Au(111) system. In a complete sequence the following parameters are measured:

1. the tip radius (FIM image)
2. the atomic structure of the apex before the first tunneling approach (FIM image)
3. the sample surface structure before the contact formation experiment (STM image)
4. the tunneling current and the force that are measured simultaneously during STM contact formation (STM distance spectroscopy)
5. the sample surface structure after the contact formation experiment (STM image)
6. the atomic structure of the apex after the last STM image (FIM image)

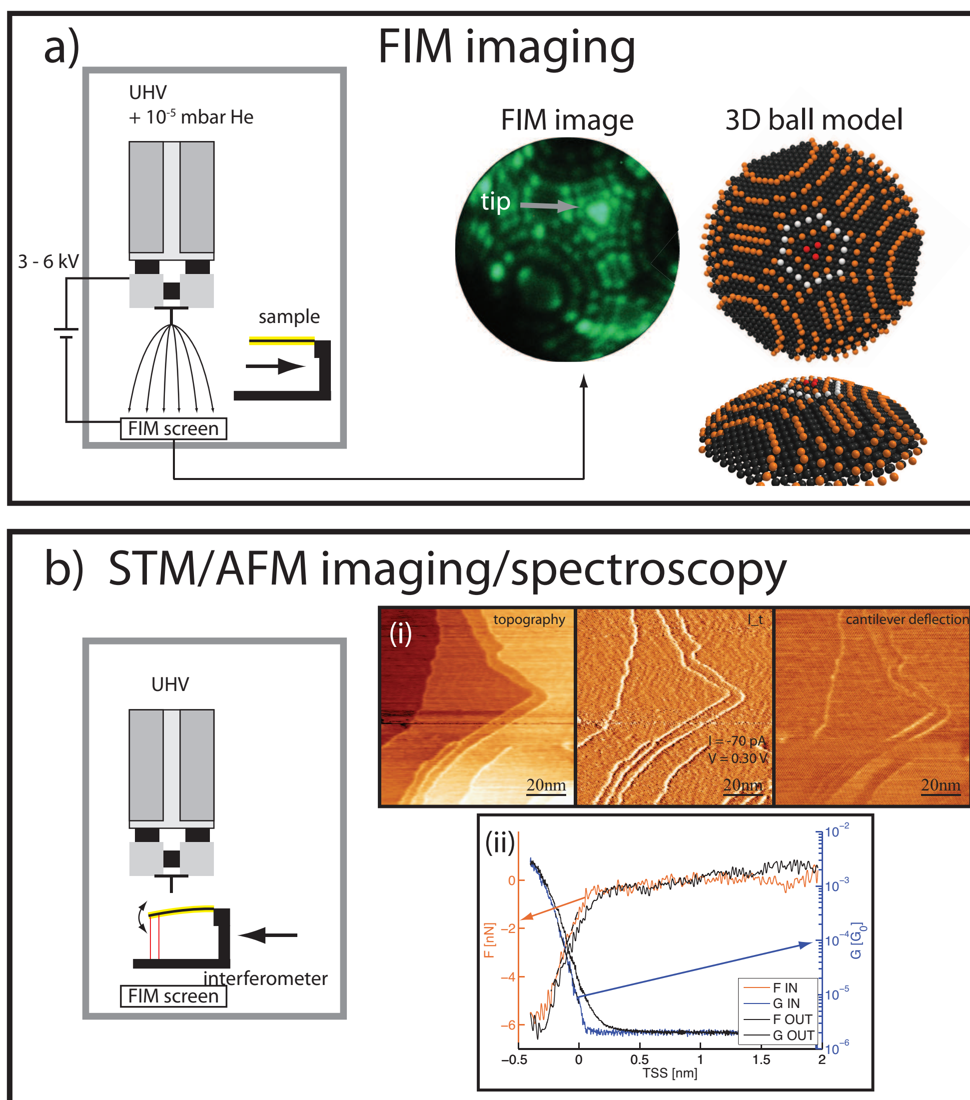

Figure 2.2 An overview of the measurement. a) Before and after the STM/AFM data acquisition, the sample is placed aside to clear the path for the FIM operation. A FIM image is taken and the structure of the tip is determined and represented as 3D ball model. b) The high voltage is switched off and the sample inserted. Now tunneling current and force data can be acquired simultaneously. E.g. scanning (inset (i)) or spectroscopy (inset (ii)).

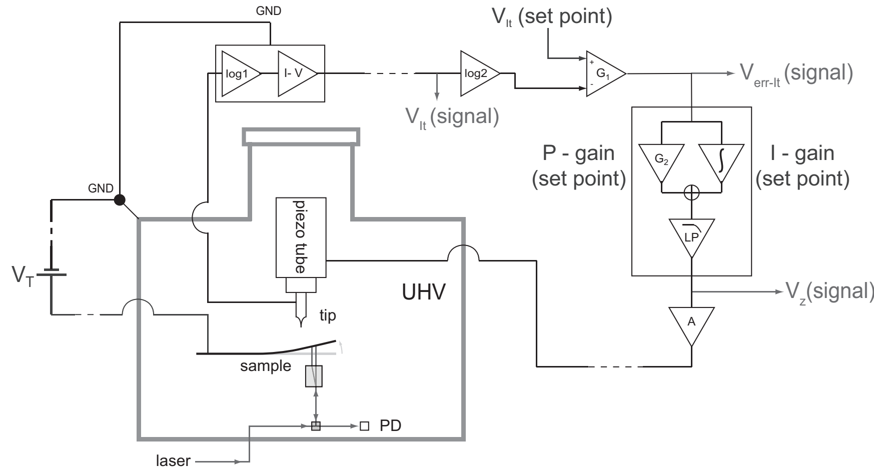

Figure 2.3 Schematic of the signal pathways of the STM/AFM apparatus. The top part describes the feedback loop of the STM circuit and is discussed in section 2.2.1. The interferometer measurement is indicated below the sample and is discussed in section 2.2.2

An overview of the procedures involved is given in figure 2.2. In the following steps 1 to 6 will be called a sequence. Each of the sequences presented in this thesis have the full information that is mentioned here. All experiments have been done in the order of steps 1 through 6. The structure of the analysis is sectioned in parts that concentrate on single aspects of the STM contact.

2.2.1 STM

As mentioned earlier, the tunneling signal was used as feedback signal to control the tip-sample gap. In the top part of figure 2.3 a schematic of the feedback loop is given. Before the tip was approached to the sample, the user set the bias voltage V_t, the feedback V_{It} set point, the I-gain and the P-gain value (as indicated in fig. 2.3). The gain values were evaluated by trial and error. A systematic approach to determine optimal feedback parameters is described in [34], [35], [36]. Bias voltage values below 100 mV were chosen in order to minimize the electrostatic force so the sample cantilever would not snap to the tip, for details on the electrostatic tip-sample force see section 4.1.1.

Once the parameters were set, the tip was approached by the coarse approach. As part of this thesis, a new approach mechanism was designed, built and implemented. For all presented data, the new version was used. A drawing and description can be found

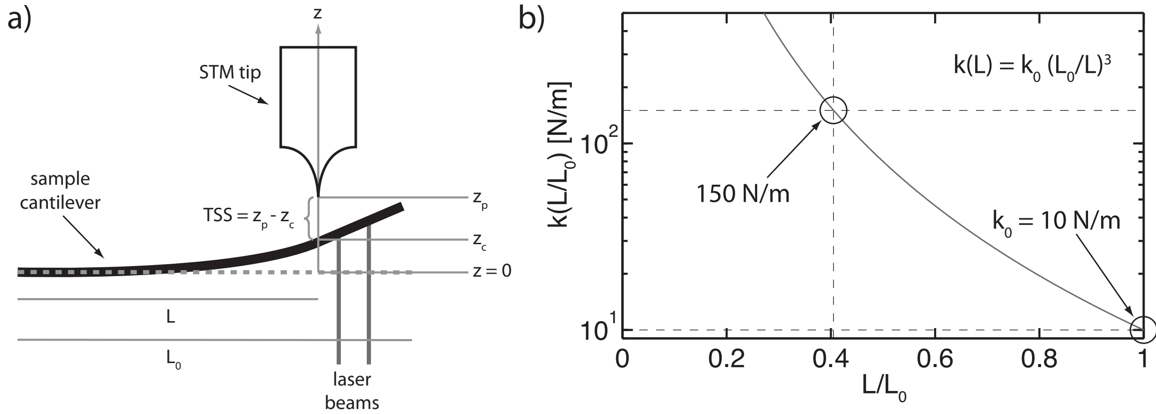

Figure 2.4 a) Distances that need to be known in order to calculate the tip sample separation (TSS). The tip sits at a distance L from the cantilever base. b) Estimation of the spring constant at the distance L from the cantilever base. A value of 150 N/m has been used for most of the experiments

in appendix C. This approach moved the tip in stick slip fashion towards the surface. When the current reached the set point level, the approach stopped and the tip was in tunneling range. Now the user was able to acquire STM scans or distance curves. During the experiments the tunneling current V_{It}, the error signal V_{err-It} and the topography signal V_z were recorded (all designated as signals in fig. 2.3).

2.2.2 AFM

As indicated in figure 2.3, the cantilever deflection was measured by a differential interferometer which is described in [30] and [33]. Laser light was guided into the UHV chamber using a fiber feedthrough. It was split into two beams that were directed to the back of the sample cantilever. The reflected beams had a path difference that corresponded to the amount of beam bending. The signal was recorded by a pair of photo diodes (PD).

Tip Sample Separation

In contrast to the standard STM, a flexible sample was used for the data acquisition for this thesis. That gave the opportunity to acquire force information but made it necessary to measure the cantilever deflection and calculate the correct tip-sample separation (TSS). In the following z_p will be used to indicate the piezo tube position and TSS for the distance that has been corrected for the cantilever bending. Figure 2.4 a) gives an overview of the

concept. As reference in the vertical direction the cantilever without any force interaction between tip and cantilever sample was taken, e.g. when the tip was far away. This vertical level was defined as $z = 0$ at this point. The vertical cantilever deflection at the tip position was called z_c, the vertical tip position measured from $z = 0$ was called z_p. Now the corrected tip sample separation can be calculated with:

$$TSS = z_p - z_c \tag{2.1}$$

Figure 2.4 b) shows how the spring constant at the tip position L can be estimated. By measuring the spring constant at the end of the cantilever k_0 the following simple relation can be used

$$k(L) = k_0 \left(\frac{L_0}{L}\right)^3, \tag{2.2}$$

with the cantilever length L_0. The graph is calculated for a spring constant of $k_0 = 10$ N/m. k_0 and the tip position L at which $k(L) = 150$ N/m are marked in the graph. In SPM systems a snap to contact occurs if the spring constant of the cantilever is smaller than the maximum force gradient of the attractive tip-sample force, which has an approximate maximum value of 40 N/m [30]. Therefore spring constants larger than 50 N/m were used. The interferometer signal measured the path difference between the two spots at which the laser beams reflected off the sample. In order to evaluate the deflection of the cantilever beam at the position of the tip apex, a transformation was used. As further described in [33] a simple formula for the cantilever deflection can be derived by making use of the geometric shape of a cantilever that is bent by the point interaction between the tip apex and the cantilever at the tip position and fixed at one end. Knowing the tip distance from the fixed end L, the laser spot displacement d_0, the wavelength of the laser $\lambda = 780$ nm, the calibration signal amplitude U_{p2p} and the measured interferometer signal S,

$$z_c = \underbrace{\frac{2}{3}\frac{L}{d_0}}_{geom.} \cdot \underbrace{\frac{\lambda}{2\pi U_{p2p}} S}_{interfero.} \tag{2.3}$$

will yield the deflection of the cantilever z_c at the tip position.

A comparison between the current and force signals in dependence of the piezo travel

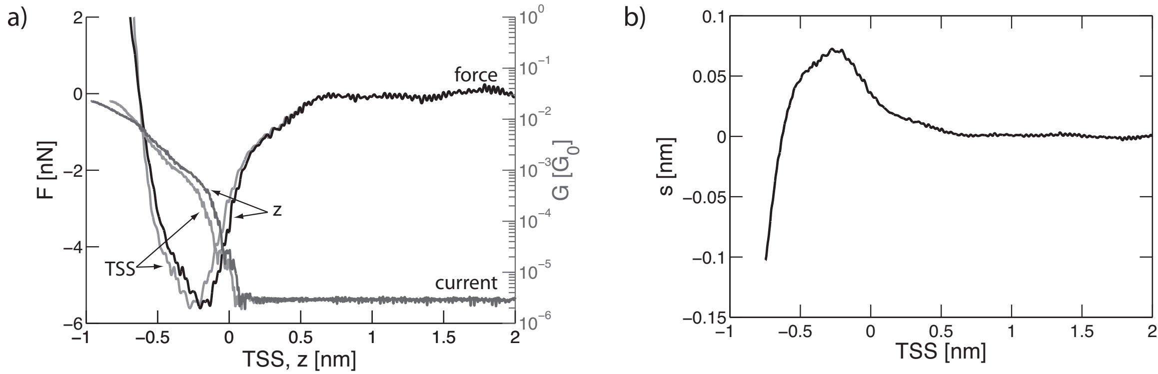

Figure 2.5 a) The effect of the cantilever motion. The difference between $F(TSS)$ and $F(z)$ and for the current traces is easily detectable. The ABH changes if the cantilever motion is taken into account ($ABH_z = (3.07 \pm 0.05)eV$, $ABH_{TSS} = (3.58 \pm 0.06)$ eV). For the local stiffness a change from $k_z = (11.94 \pm 0.17)$ N/m to $k_{TSS} = 12.88 \pm 0.20)$ N/m is detected. b) Cantilever deflection in nm versus distance.

and the tip sample separation is given in figure 2.5 a). Figure 2.5 b) displays the deflection s of the cantilever in nm for this data set. At the maximum force of 5.5 nN in figure 2.5 a) the deflection is about 0.75 nm corresponding to a spring constant of 73 N/m. The correction of the z-piezo extension leads to a shift of the data towards smaller gap values for cantilever motions towards the tip (positive deflection) and larger gap values for negative deflection values in the data presentation. This has an effect on the estimated apparent barrier height (the fitting procedure is defined in equation (4.7)). For the presented data set, the apparent barrier height changed from $\phi_z = (6.0 \pm 0.6)$ eV to $\phi_{TSS} = (3.3 \pm 0.5)$ eV if the tip-sample separation is considered.

2.2.3 Description of the Curve Parameters

In order to avoid misconceptions, a short summary of the data presentation is given in this section. Figure 2.6 shows a typical representation of the data that will be used throughout this thesis.

The current will be displayed in terms of conductance because the conductance is a more universal parameter than the current. Expressed in units of the fundamental conductance quantum G_0, the conductive state of the tunneling gap in relation to G_0 can be immediately read from the graph. A conversion of the current into conductance allows a comparison between different results since the current depends on the bias voltage for the

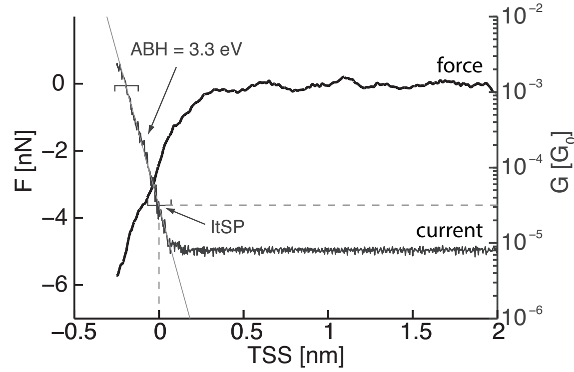

Figure 2.6 An example set of spectroscopy curves. The force and the conductivity are plotted versus the tip sample separation. The fit and the fit region are indicated. At TSS = 0 the tunneling current set point is reached.

same conductance. The conversion from current to conductivity in quantum units follows a simple relation:

$$G/G_0 = R_0 \frac{I_t}{V_t} \tag{2.4}$$

with the fundamental resistance $R_0 = 1/G_0 = h/(2\,e^2) \simeq 12.9$ kΩ, the bias voltage V_t and the tunneling current I_t. In slopes that involve a logarithmic conductance or current axis, e.g. the fit for the apparent barrier height (equation (4.9)), one can use either current or conductance since

$$\begin{aligned} \Delta \log G &= \log(G_2) - \log(G_1) && (2.5)\\ &= \log(R_0/V_t) + \log(I_{t2}) - \log(R_0/V_t) - \log(I_{t1}) && (2.6)\\ &= \Delta \log I_t. && (2.7) \end{aligned}$$

The ABH fit region of the data starts at the conductivity value that corresponds to the tunneling current setpoint and is marked with brackets in the plot.

In this case the tunneling setpoint was set to $I_t = 50$ pA. The conductivity value at the applied bias voltage of $V_t = 20$ mV is then calculated to be $G = 3.3 \cdot 10^{-5} \cdot G_0$. In order to compare different runs, the TSS is set to zero when the conductivity value reaches the set point level. Gray dashed lines mark that point in figure 2.6.

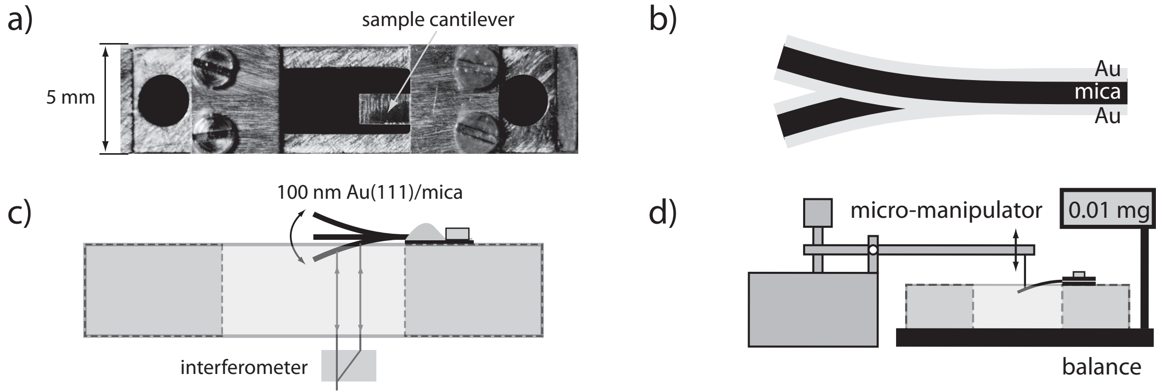

Figure 2.7 a) Photo of the cantilever sample in a sample holder taken as top view. b) Schematic of the cantilever sample. A beam of mica is evaporated with a layer of about 100 nm Au(111) on either side. c) Side view of the sample setup. The laser beam is divided by the interferometer and reflects off the cantilever back side. The sample can deflect and is attached to the sample holder by gluing to a clip system. d) Calibration of the sample cantilever. A micrometer screw is pressing on the sample that sits on a balance

2.3 The Sample: Au(111) Cantilever Samples

As mentioned above, the flexible sample acted as force sensor in the FIM-STM/AFM system. In order to realize a consistent flexibility, which results in a predictable bending behaviour, a piece of mica was cleaved down to a thickness of a several tens of microns. The cantilevers used in this thesis vary from 20 μm to 70 μm. A photo of a real sample cantilever in a sample holder that was used in the system is given in figure 2.7 a). The sample holder was used to fix the sample in the system and allowed the sample to bend up and down for the force measurement. Therefore a cut in the center of the holder was needed to permit this deflection and also to realize the interferometer measurement with laser light from below the sample. The cantilever itself was in this case 2.4 mm long and 1.4 mm wide with a thickness of 50 μm. One can see the clip system that is used to fix the sample to the right of the cantilever. As further described in [33], ceramic glue purchased from Aron Ceramics was used to fix the cantilever to the clip and SPI conductive silver paint to contact the gold layer for the STM measurements. A schematic of the assembly is given in fig. 2.7 b). The mica beam was evaporated with a layer of Au(111) which was 100 nm thick on both sides to ensure both a good sample quality on the side that was measured with the STM and a good back reflection on the other side. In fig. 2.7 c) the force measurement process is illustrated.

The laser beam coming from below gets split into two beams by a calcite crystal and hits back side of the sample. A motion of the sample induces a path length difference which the interferometer detects. The calibration is illustrated in fig. 2.7 d). In order to obtain the spring constant at the end of the cantilever k_0, a micrometer screw setup was used to press a known distance into the cantilever end which sits on a balance. The spring constant is found by using

$$k_0 = \frac{m\,g}{x} \tag{2.8}$$

with the mass m measured by the balance, the gravitational constant g and the traveled distance x. Details on aspects concerning the sample like the mica preparation, the gold evaporation, the sample fixation and details on the interferometer can be found in [33].

2.4 Raw Data and Data Processing

This section is meant as a concise overview of the data treatment. In figure 2.8 an example filtering process is shown. The graphs represent a set of simultaneous force vs. tip-sample separation and tunnelling current vs. tip-sample separation curves. Figure 2.8 a_1) shows the force curves for different filtering parameters and fig. 2.8 a_2) the corresponding power spectral densities (PSD). In the case of the force curves, the original curve and the first filtered curve mark the original signal level, later curves are shifted for a better comparison. Likewise, the corresponding PSD traces have been offset. The initial, unfiltered signal is shown in black and the successive steps are numbered. As the PSD indicates, the original force signal contains peaks at 20 Hz, 22 Hz, 27 Hz, 31 Hz, 60 Hz, 180 Hz and the first flexural resonance of the cantilever at about 1.3 kHz. Since a eighth order low pass filter with a cut off frequency of 100 Hz is used, only the peaks until 60 Hz are filtered with a multiple band stop filter.

The current was treated in similar fashion. The current versus tip-sample separation data are given as semi-logarithmic plots in figure 2.8 b_1) and the according PSDs in fig. 2.8 b_2) using the same offset method for the representation as in fig. 2.8 a_1) and fig. 2.8 a_2). As the original, unfiltered PSD demonstrates, the current signal has a different nature than the force data. Only peaks at 30 Hz, 60 Hz, 180 Hz are present. These peaks are filtered with a band stop filter after applying a eighth order low pass filter with a cut off frequency of 100 Hz.

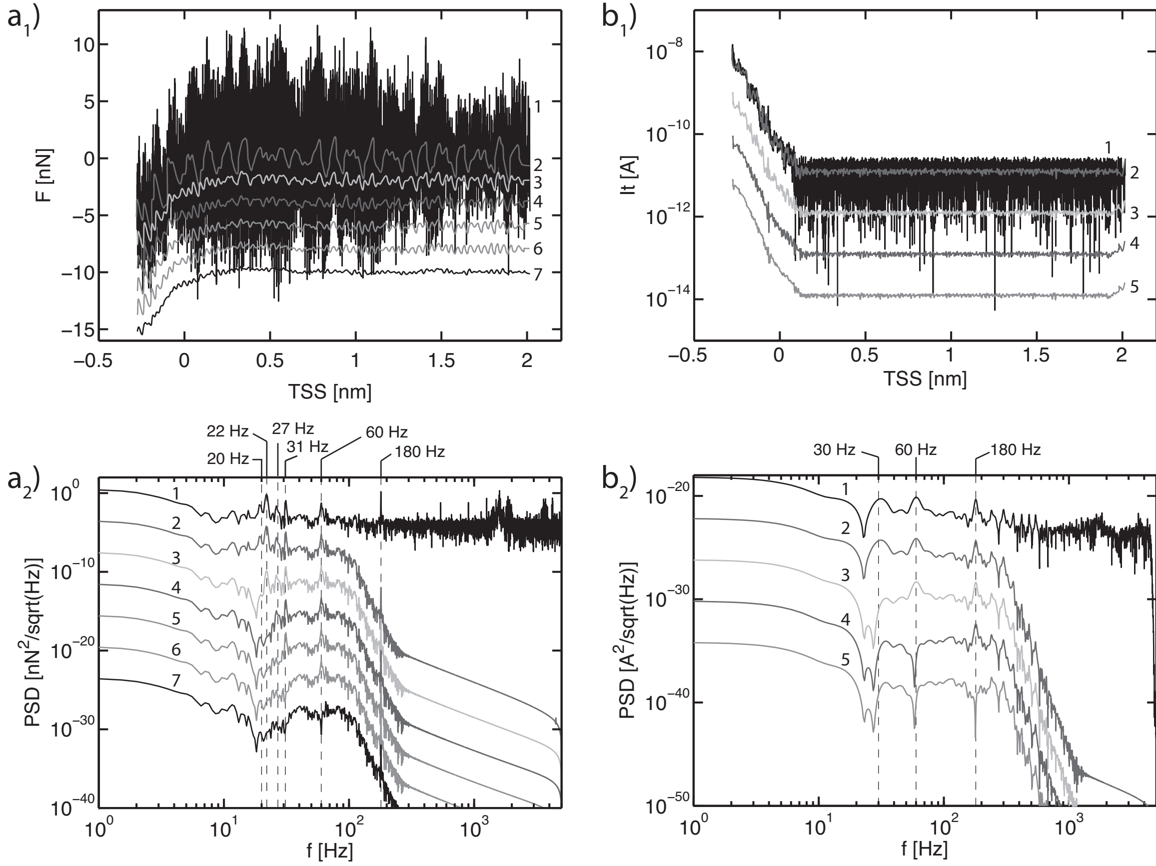

Figure 2.8 a_1) Force curves resulting from the filtering. The original curves mark the signal level. For a better comparison later curves have been offset in all graphs. a_2) PSD of the F(TSS) curves in a_1). Starting with the unfiltered data, then the following filters are added: low pass (LP) at 100 Hz, band stop (BS) at 22 (8), 22 (4), 27 (2), 31 (2), 60 (4) Hz – the value in brackets gives the filter widths the value without brackets is the filter position. b_1) Current curves resulting from the filtering. b_2) PSD of the I_t(TSS) curve that was acquired with the force curve in a). Starting with the unfiltered data, then the following filters are added: low pass (LP) at 300 Hz, band stop (BS) at 30 (12), 60 (14), 180 (20) Hz.

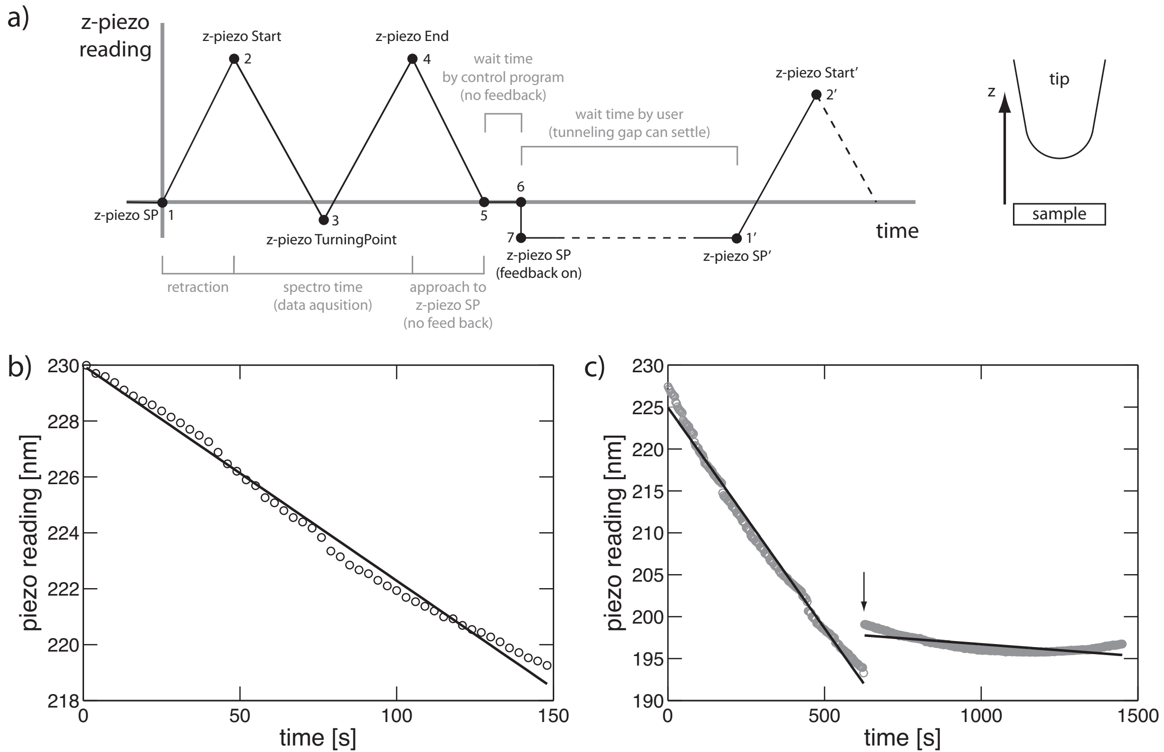

Figure 2.9 a) Schematic of a typical approach and retraction cycle indicating the piezo extension stages. b) Piezo positions for a sequence of 50 runs of 3 s each for a total of 150 s. The drift of the piezo can be extracted from the shift in the starting position. c) Piezo positions for a sequence of about 500 runs of 3 seconds each. Runs 45-252 are taken in series, then STM imaging was performed – the interruption by STM is marked with an arrow.

The reason for the variation of the noise between the force and the current data is the different acquisition of the data. Both channels were recorded via different paths and the components for conversion and amplification affected the signals in different ways. A short summary of the signal paths can be found in section 2.2.1. While the current only shows noise peaks at locations that correspond to electric line noise of 60 Hz and its harmonics, the force/cantilever deflection signal contains these peaks with additional mechanical peaks, like building vibrations at 20 Hz. A more detailed analysis of the noise structure is elaborated in [33].

2.5 Piezo Properties: Approach Cycle, Creep and Drift

All data traces shown in this thesis were measured in the same way. The user set parameters like the amount of retraction and the indentation with respect to the piezo extension value that corresponds to the tunneling set point. A schematic of the voltage versus time sequence is shown in figure 2.9 a). Once the approach was started (1), a triangular voltage profile first retracted the piezo with the tip to the stating position (2) and the data recording began. Then the tip approached towards the sample until the turning point (3) was reached. A reverse voltage profile brought the tip back to the starting position and the data recording stopped (4). Now the tip was brought back to the original set point position (5) and left there for a waiting time set by the system until the feedback was turned on again (6) and (7). This was not an ideal solution since drift might have caused the tip to be closer to the surface for the same applied voltage at point (5) than it had been before the approach cycle (1). This unwanted feature cannot be changed easily in the scanning program. At point (7) the system was ready for a new approach cycle. In cases where several runs were taken in sequence, a waiting time was specified between runs so the system could settle between runs.

Since the piezo tube was not studied in detail for its drift and creep properties, these parameters were evaluated from data that was recorded during the experimental runs. One would not expect a large contribution of the creep for the reason that a creep check was carried out before each approach/retraction sequence. Each time the piezo was fully retracted and then approached to the tunneling setpoint, like it was done to change the location on the sample, the feedback was switched off while the tunneling current was monitored. Once the current did increase due to the piezo creep, the feedback would be switched on again by the experimenter. After about 5–10 minutes the creep would be low enough so that the feedback could be switched off for about 45 seconds without an increase in the current. Since this check has been performed, it is assumed that most of the positional shift in the following is due to drift.

The drift of the setup under approach/retraction data acquisition conditions can be quantified by a plot of the piezo starting position (positions 1 and 7 in figure 2.9 a)) versus the elapsed time for a given sequence. Figure 2.9 b) illustrates the drift for a sequence of 50 runs. The tip was approached and scanning before the curves were taken. In the plot the starting position of the piezo for each curve is displayed and knowing that the waiting time

between runs was set to 1 s (total run time = 3 s), a drift rate of 0.08 nm/s = 272 nm/h for this sequence has been evaluated to first order from the slope of the data. Another sequence is given in figure 2.9 c) for comparison. It is obvious that the piezo drift settles in the second part of the data. Fitting a slope to runs 45–252 yields a drift rate of 0.05 nm/s = 180 nm/h and for the second part, runs 253–528, in a simple linear approximation a drift rate of 0.004 nm/s = 14 nm/h has been calculated.

The drift in the x and y direction cannot be monitored in the same way since the feedback does not have a reference in the x-y plane that is adjusted to after each cycle. From STM images a maximum drift of 0.004 nm/s = 15 nm/h in x-y direction has been deduced.

2.6 Measurement Uncertainties

In the analysis force versus tip-sample separation plots as well as current versus tip-sample separation plots are investigated. Therefore the uncertainties of the measured physical quantities are of interest. First the errors on the force and tip-sample separation will be discussed, followed by a description of the current uncertainties.

The measurement uncertainties are calculated with the Gaussian calculus for error propagation using the quadrature formulation:

$$\delta f = \sqrt{\sum_{i=1}^{n} \left(\frac{\partial f}{\partial x_i}\right)^2 (\delta x_i)^2} \tag{2.9}$$

for the absolute uncertainty of a physical quantity $f = f(x_1, \ldots, x_n)$ that is calculated from the measured parameters x_i with the uncertainties δx_i. In this approach only uncertainties due to initial precision are considered. The purpose of this section is the presentation of upper boundary conditions for each data point and on this basis the presented approach is justified.

Uncertainty of F

The force is calculated by using

$$F = k(L) \cdot z_c. \tag{2.10}$$

Using equation (2.9) one obtains for the absolute uncertainty of the force

$$\delta F = F\sqrt{\left(\frac{\delta k}{k}\right)^2 + \left(\frac{\delta z_c}{z_c}\right)^2}. \tag{2.11}$$

As indicated above, a number of parameters have to be measured in order to obtain the spring constant k and the cantilever deflection z_c. In the following the components of the equation will be investigated. With the definition of $k = k(L)$ in equation (2.2), the relative uncertainty for the spring constant is calculated to be

$$\frac{\delta k}{k} = \sqrt{\left(\frac{\delta k_0}{k_0}\right)^2 + \left(3\frac{\delta L}{L}\right)^2}. \tag{2.12}$$

Calculating the uncertainty of k_0 from equation (2.8) one obtains

$$\frac{\delta k_0}{k_0} = \sqrt{\left(\frac{\delta m}{m}\right)^2 + \left(\frac{\delta x}{x}\right)^2}. \tag{2.13}$$

Remembering that k_0 is the spring constant at the end of the cantilever and that the calibration is performed as described in section 2.3, the upper boundary on the first term is estimated by assuming a deflection of 50 μm at the end of the cantilever. For a cantilever with a spring constant of $k_0 = 10$ N/m, the balance used for calibration would show 0.5 mg. Since the balance has an accuracy of 0.001 mg the relative error on m is 2 % from the first term. The accuracy on x is 1 μm and therefore the second term would have a contribution of 2 % in this case. In reality the spring constant is evaluated by a fitting procedure. With these numbers the uncertainty of k_0 becomes

$$\frac{\delta k_0}{k_0} = \sqrt{(0.01)^2 + (0.01)^2} = 0.0141, \tag{2.14}$$

and for k one one obtains

$$\frac{\delta k}{k} = \sqrt{(0.141)^2 + (3 \cdot 0.033)^2} = 0.172. \tag{2.15}$$

The length from the cantilever base to the position of the tip L is estimated by measuring pixels of digital photographs and using a known reference in the picture for calibration. The accuracy on the length is $\delta L = 0.05$ mm and for distances of about 1.5 mm the relative

error for L becomes 3.3 %.

For the cantilever position the uncertainties are calculated from

$$\frac{\delta z_c}{z_c} = \sqrt{\left(\frac{\delta L}{L}\right)^2 + \left(\frac{\delta d_0}{d_0}\right)^2 + \left(\frac{\delta U_{p2p}}{U_{p2p}}\right)^2 + \left(\frac{\delta S}{S}\right)^2} \tag{2.16}$$

based on equation (2.3). The value for the first term is taken from above. Since d_0 is measured through a digital picture in the same way as L, the deviation is $\delta d_0 = 0.05$ mm for a value of $d_0 = 1.00$ mm. The value for the calibration signal U_{p2p} has been read from an oscilloscope with an accuracy of $\delta U_{p2p} = 0.05$ V. In the measurements presented here, U_{p2p} had a value of 5 V or more, which leads to an error of 1 % or less. The signal of the interferometer S has noise on it in the raw data. Since the data are filtered with a low pass filter, an estimate of the uncertainty from the final noise level should be good enough and the peak to peak value of the deflection signal is evaluated and used for δS. Taking the results from above the relative uncertainty of z_c is calculated to be

$$\frac{\delta z_c}{z_c} = \sqrt{(0.033)^2 + (0.050)^2 + (0.010)^2 + \left(\frac{\delta S}{S}\right)^2} = \sqrt{0.0037 + \left(\frac{\delta S}{S}\right)^2} \tag{2.17}$$

Now the uncertainty of the force data can be calculated with

$$\delta F = F\sqrt{0.0333 + \left(\frac{\delta S}{S}\right)^2}. \tag{2.18}$$

An example plot with error bars for the force is given in figure 2.10 a). As seen from equation (2.18), the error on F has a portion that is directly related to the value of the force which is noticeable in the plot.

Uncertainty of TSS

According to equation (2.1) the tip sample separation would have the following uncertainties:

$$\delta TSS = \sqrt{\delta z_p^2 + \delta z_c^2}. \tag{2.19}$$

The upper boundary of the piezo uncertainty has been estimated from figure 2.9 c). A creep at a rate of 0.05 nm/s has been evaluated for runs 45-252. Now an uncertainty for any data

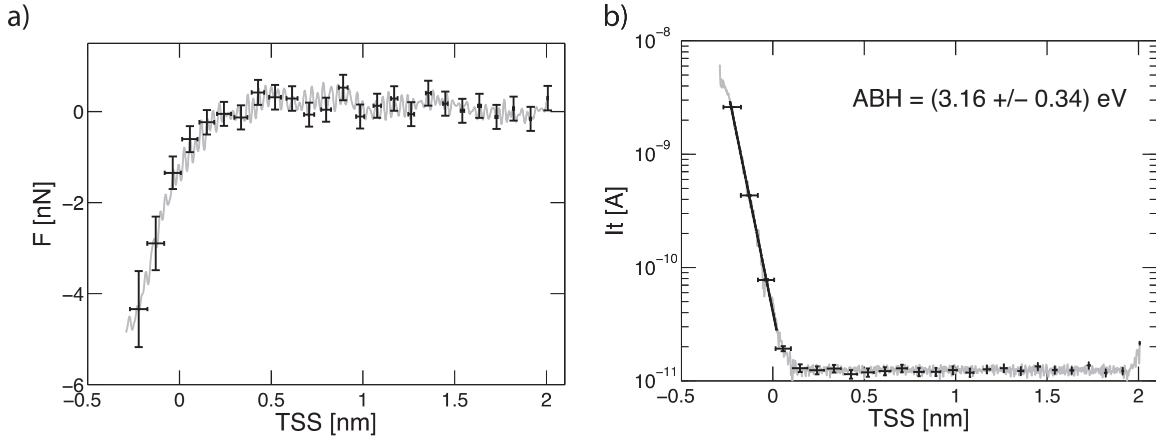

Figure 2.10 a) Force versus tip-sample separation plot with error bars that have been calculated with eqs. (2.21) and (2.18). Only every 200th point is shown with its individual error. The original signal is drawn in gray. b) Same plotting for the current versus tip sample separation plot with error bars that were calculated with eqs. (2.21) and (2.23). The fit for the ABH is drawn in black and calculated using the method presented in [37].

point n that has the associated time $n_t = 2\ \mathrm{s} \cdot n/10^4$

$$\delta z_p = 0.05\ \mathrm{nm/s} \cdot n_t \tag{2.20}$$

can be defined using the data acquisition rate of 10^4 pts/s and a total run time of 2 s which was used in this thesis. A drift compensation has not been performed since the effect was small. With all the above, the relative uncertainty of the tip sample separation becomes

$$\delta TSS = \sqrt{(5 \cdot 10^{-6}\ \frac{\mathrm{nm}}{\mathrm{s}} \cdot n_t)^2 + z_c^2 \left(0.0037 + \left(\frac{\delta S}{S}\right)^2\right)}. \tag{2.21}$$

Figure 2.10 illustrates the resulting error bars in force and current versus tip-sample separation plots. As the formula indicates, the uncertainty increases slightly as the acquisition progresses.

Uncertainty of I_t

In the case of the current versus tip sample separation plots, the uncertainty for the distance data is already calculated in equation (2.21). The absolute uncertainty for the current has

been estimated from the electronic noise level and set to

$$\delta I_t = 10^{-12}\ \mathrm{A} \tag{2.22}$$

Figure 2.10 b) shows a graph of the current versus tip sample separation (TSS) with error bars based on the description. The fitting result for the apparent barrier height (ABH) is presented as solid line. In order to realize this fit, the natural logarithm of the data was used to linearize the data in the fit region. The uncertainty used for the error bars in a $\ln(I_t)$ versus TSS plot becomes

$$\delta \ln(I_t) = \frac{\delta I_t}{I_t} \tag{2.23}$$

by using equation (2.9) on $f = \ln(I_t)$. Since both coordinates have non-negligible uncertainties associated with them, a fitting algorithm that considers an uncertainty input for both coordinates is needed. The weighted total least square fit algorithm by Krystek [37] (available as Matlab function `wtls_line.m` on the MathWorks file exchange website[1]) has been used throughout this thesis for the fit to the current data and to estimate the uncertainty of the fit. As input for the fitting algorithm the standard error of both coordinates is used for each point individually. Therefore the convention

$$\sigma_f = \delta f \tag{2.24}$$

for the conversion of the measurement uncertainty δf into the standard deviation σ_f has been used. A full statistical approach for this fit including a standard deviation from data averaging and systematic errors on both coordinates can be found in [38]. Finally, the resulting value of the apparent barrier height ϕ derived from the fitted slope m (equation 4.9) has a standard uncertainty of

$$\sigma_\phi = \frac{2\sigma_m}{m}\,\phi. \tag{2.25}$$

[1] http://www.mathworks.com/matlabcentral/fileexchange/17466

with the result σ_m from the covariance matrix of the the fit algorithm using the Gaussian error propagation for statistically independent parameters x_i

$$\sigma_f = \sqrt{\sum_{i=1}^{n} \left(\frac{\partial f}{\partial x_i}\right)^2 \sigma_i^2}. \tag{2.26}$$

σ_m is usually about 10 % of m. By far the largest contribution to a variation of the ABH value from run to run is the selection of the fit region. Obviously the slope varies if a region with data that deviate from a linear behaviour is included into the fitted data range. This variation can lead to changes on the order of 1 eV if the fit is not visually checked. Using a visual check to identify linear regions, this deviation can be limited to a relative uncertainty of $\delta\phi_{range}/\phi = 20$ %. A test for several curves was performed to acquire these numbers. This error due to the range selection is added to the total uncertainty of the result for ϕ. The stated error is calculated as

$$\delta\phi = \sqrt{\sigma_\phi^2 + (\delta\phi_{range})^2}. \tag{2.27}$$

In the following plots the error bars are not plotted for a better overview. Nevertheless, the uncertainties resulting from the fit, considering uncertainties on both coordinates, are given.

CHAPTER 3

The Probe: FIM characterized W(111) STM-Tips

In all scanning probe microscopy (SPM) methods the tip that probes the sample plays a key role in understanding the results [12], [39]. Recent simulations show that both the tunneling current and the short range force interaction between a STM tip and an atomically flat sample is strongly affected by small structural differences in the gap. Comparisons between approaches at different sample sites and tips with different terminations show this [40], [41], [42], and especially in [14], where the contrast of pentacene molecular orbitals for a Ag, Cl and CO terminated tip are directly compared. A study of other molecules showed that molecular orbitals can only be resolved completely in the case of pentacene and partially in the case of PTCDA [43]. Therefore a great need exists to describe the tunneling junction as precisely as possible. Here, the STM tip structure has been characterized with great detail before it was used in the actual experiments. The sample structure is characterized by STM scans and the images can be compared to the extensive research that has been performed on Au(111) [44], [8].

Tip preparation and characterization is therefore vital for a quantitative and qualitative interpretation of SPM results. In scanning tunneling microscopy (STM) most researchers use tips that are electrochemically etched from cold-drawn polycrystalline tungsten wires [39]. More and more groups use quartz tuning forks with attached tungsten tips for atomic force microscopy (AFM) like the q-plus sensor [45]. These tips are also electrochemically etched. Consequently a reliable tip etching method is highly desirable. Many different methods were developed. In this chapter a modified version of the *drop-off* tech-

nique, introduced by Ibe et. al. [46] and further developed by other authors like Melmed et. al. [47], is described. Lately, the lamella technique [48] has become more popular. This lamella technique uses a wire loop or a hole in a metal plate to hold the etching solution as liquid layer by surface tension instead of a container. Another 3 step process using the *drop-off* technique has been proposed recently [49]. This technique delivers tips with radii of about 3 nm before *in situ* heating in UHV.

In the context of this thesis the *drop-off* method has been used and in this chapter it is demonstrated how well the electrochemical etching works once the liquid cell is divided into a tip part and a counter electrode part with a large opening for the ion current. The etching process is monitored and traces of the etching current versus time are given. Field emission data (in the form of Fowler-Nordheim plots) are used as *in situ* sharpness test after resistive heating cycles. Finally atomically resolved field ion microscopy (FIM) images [50], [51] are presented. By analyzing the FIM images it is shown that the presented method produces tips with a radius of about 3 – 10 nm in a highly reproducible way after *in situ* UHV cleaning. These tips do not need any further treatment before being used in the STM.

As a reference for the work that has been done by former members of the FIM-STM/AFM research group on this topic the author suggests references [50], [51] and [52].

3.1 Etching the tip

In order to obtain an atomically sharp tip which can be used for the STM/AFM setup a tungsten wire with a diameter of 100 μm (for polycrystalline wire) or 127 μm (for single crystalline wire) in a KOH solution was electrochemically etched. This preparation method is well known and used by almost all research groups that use UHV STMs. Several publications describe various methods on how to use the electrochemical etching process for various materials [50], [53], [48].

For this thesis the most common method for tungsten was used: a cup that contains a KOH solution as well as some device to dip the tip into the solution and a counter electrode to complete the circuit. Figure 3.1 a) shows the electrochemical tip etching setup. The wire that one wanted to etch was dipped into an electrolyte solution that etcheed the wire at point A (*dip-in* length 0.65 mm – defined as the distance that the wire was introduced in the solution after the liquid makes contact with the wire). The *dip-in* length is critical and the optimal length has to be found for each setup, concentration and wire diameter as further discussed in [49]. A micrometer screw (F) was used to realize and to measure

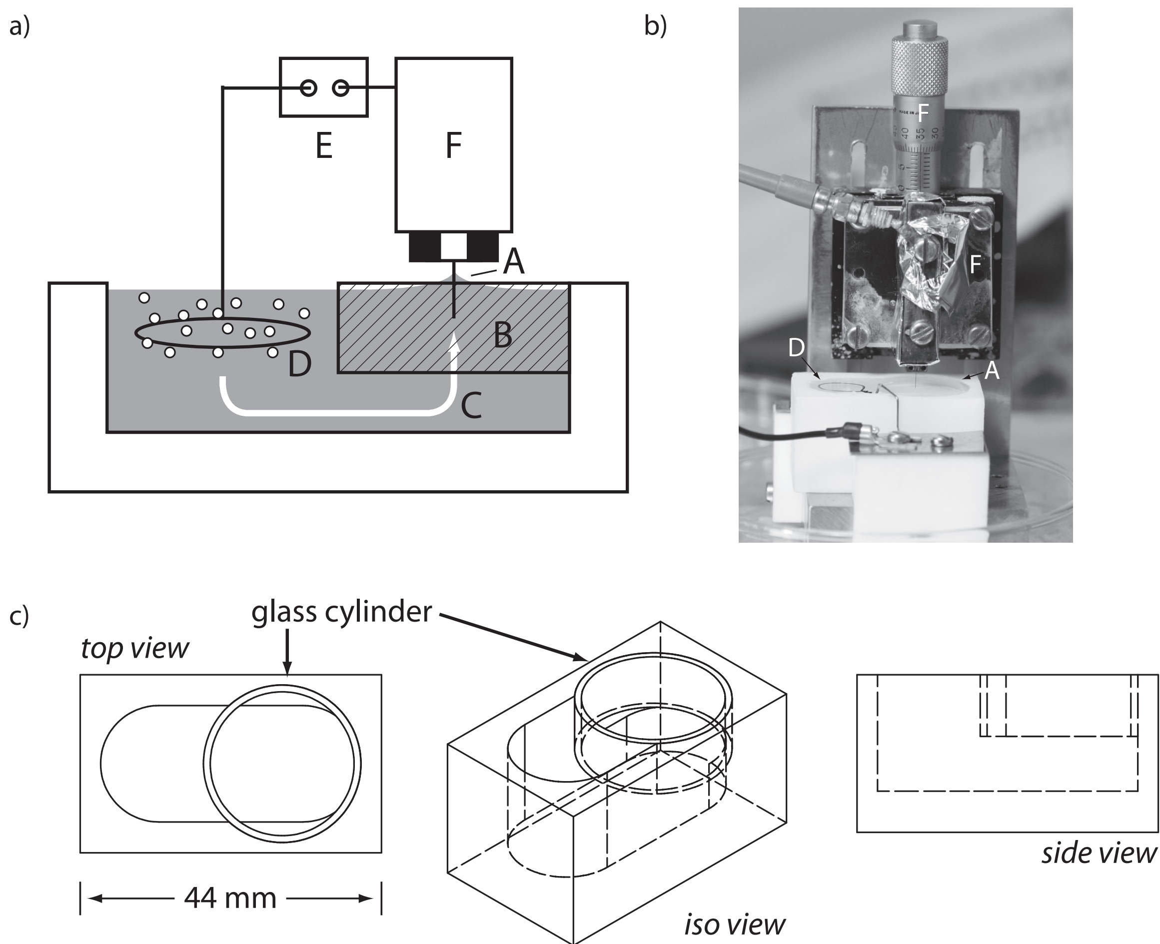

Figure 3.1 a) The tip etching setup. In this configuration the meniscus region (A), where the wire gets etched, is shielded from the cathode (D) by a glass cylinder (B). This leads to a mechanical isolation of the liquid surface from the hydrogen bubbles that build up at the cathode. b) A photo of the tip etching setup. c) The etching container: Top view, isometric view and side view with inserted glass cylinder. Hidden lines are drawn as dashed lines.

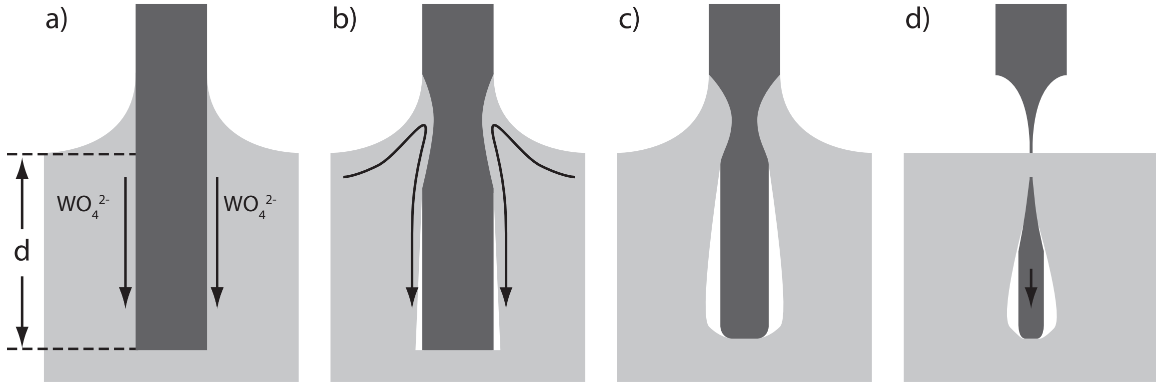

Figure 3.2 Etching steps: a) the reaction begins and the WO_4^{2-} among other tungsten oxides and hydroxides starts to build as reaction product. b) A flow brings OH^- ions to the meniscus region and coats the bottom part of the wire with the reaction products. c) The wire region at the meniscus is etched much faster than the bottom part that is covered with the reaction products. d) Once the most aggressively etched wire part is very thin the bottom falls of and we are left with a an atomically sharp tip.

the vertical motion. A counter electrode (D) was immersed in the solution as well. This electrode consisted of a loop of stainless steel wire with a wire diameter of 0.55 mm. The power was provided by a DC power supply (E), which had a differentiator circuit inside. The whole setup was placed on a large steel plate that had a foam layer underneath. This isolated the system from mechanical vibrations.

Once the power was switched on, a constant voltage of +3.0 V was applied to the tip and the well known etching reaction started:

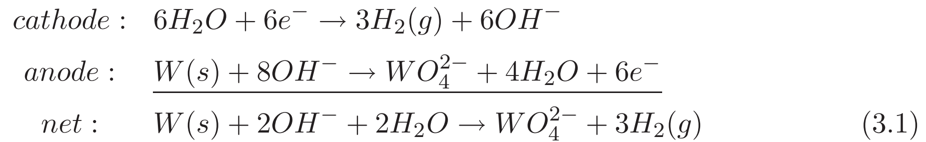

$$\begin{aligned} cathode: &\quad 6H_2O + 6e^- \rightarrow 3H_2(g) + 6OH^- \\ anode: &\quad \underline{W(s) + 8OH^- \rightarrow WO_4^{2-} + 4H_2O + 6e^-} \\ net: &\quad W(s) + 2OH^- + 2H_2O \rightarrow WO_4^{2-} + 3H_2(g) \end{aligned} \tag{3.1}$$

As seen from this equation KOH in DI-water was used as etching solution ($c \simeq 9.85$ mol/l). Johnson et. al. [54] found that the reaction which etches tungsten in a KOH environment consists of several oxidation steps. Therefore equation (3.1) only gives the net reaction of the process. Some researchers use NaOH to etch tungsten. For noble metals like Ir or Pt a more reactive etching solution is needed [47].

A crucial difference between the setup presented here and most of the setups using a divided liquid cell that were published [46], [47], [53] is that a glass cylinder with a large diameter (21.0 mm) compared to the wire diameter (0.100 – 0.127 mm) was used. This ensured a good ion current flow (C in figure 3.1 a)) and minimum disturbance due to turbulence around the meniscus (A in figure 3.1 a)). A photo of the setup is shown in figure 3.1 b).

A technical drawing of the container is shown in figure 3.1 c). It is a block of teflon that is 26.0 mm wide, 44.0 mm long and 23.0 mm high. A 37.0 mm long and 17.0 mm deep slot was milled (17.0 mm diameter end mill) first into the material. Then a hole (37.0 mm diameter) was drilled 9.0 mm deep at one end to hold the glass cylinder as indicated in figure 3.1. The exact measurements are not critical and can be adjusted to any available glass cylinder of similar dimensions. The glass cylinder was cut from a cylindrical storage container.

The process of the tip formation is displayed in figure 3.2. In part a) the initial situation is illustrated. The wire was inserted with the *dip-in* length $d = 0.65$ mm. Once the power was switched on, the reaction started and WO_4^{2-} was produced among other reaction products. Since these oxides and hydroxides were heavier than the initial $H_2O + KOH$ solution, they slided downwards along the wire surface. As b) displays, a flow was established by the reaction and reaction products accumulate at the bottom of the inserted wire. This shields the bottom part and the meniscus region was etched at a much higher rate. Part c) of figure 3.2 demonstrates the effect on the wire shape. As the etching progressed, the wire become very thin at the meniscus and the bottom part of the wire broke off due to gravity as illustrated in part d). This produced a tip that had only a few atoms at the point of rupture [49], [50], [51]. In order to stop the etching right after the *drop-off* and prevent blunting due to further etching, the power supply had to switch off just after the wire breaks. Descriptions of suitable power supply designs can be found in the literature [46], [55], [56].

In order to have a better understanding of the stability of the etching process, the etching current was recorded. Two traces of the etching current vs. time can be found in figure 3.3 a) for a single crystalline tungsten wire (SW) ((111) orientation) and a polycrystalline tungsten wire (PW). The graphs show a spike at the beginning (A) (12.2 mA for SW and 12.6 mA for PW) and after 1.5 – 3 seconds the process stabilized (B) (9.4 mA for SW and 7.0 mA for PW). The spike originated from the fact that the bottom part of the wire was

Table 3.1 Results for tips that were characterized with field emission.

type	$\overline{I}_{drop}$	σ_I	$\overline{t}_{etch}$	σ_t	FE success
PW	3.5 mA	0.9 mA	49.1 s	6.9 s	9/12 = 75 %
SW	4.8 mA	2.2 mA	79.0 s	9.8 s	18/20 = 90 %

bare at the beginning and OH^- ions could reach the whole bottom part. As the etching progressed the bottom part of the wire was covered with WO_4^{2-} and only the meniscus region contributed to the current. Therefore the current decreased quickly back to a more stable value. Then the current decreased almost linearly (C) (the slope for both traces was $s = -0.1$ mA/s) until the bottom part dropped off (D) (at 2.3 mA for SW and 2.8 mA for PW). The *drop-off* current and the etching time was very reproducible for a given concentration, counter electrode cleanliness and wire diameter. Compared to other methods a rather high concentration (9 – 10 mol/l) was used here and therefore the etching time was very short (84.0 s for SW and 43.0 s for PW for the shown traces; the difference in the etching time is due to the different wire diameter – see the table 3.1 for average values of the etching time).

Right after the *drop-off* the tip was retracted, cleaned with a DI-water, ethanol, acetone and ethanol sequence to remove etching residues and the macroscopic shape was checked in an optical microscope (insets (SW) and (PW) in figure 3.3). At this point it is useful to point out an advantage of this method over the lamella technique [48]. The wire can be pre-etched with the *drop-off* technique which leads to reduced surface roughness in the meniscus region at the start of the tip etching, leading to a more defined tip shank. Another advantage is the small amount of wire that is used which is important when working with expensive single crystalline wires (200 $/cm).

The following disturbances have to be eliminated in order to obtain similar results to what is presented here.

- Flakes from the PW wire surface by pre-etching.
- Air turbulence (e.g. building ventilation or people passing by) disturbs the liquid surface. As consequence of the oscillating liquid surface the etching current will show

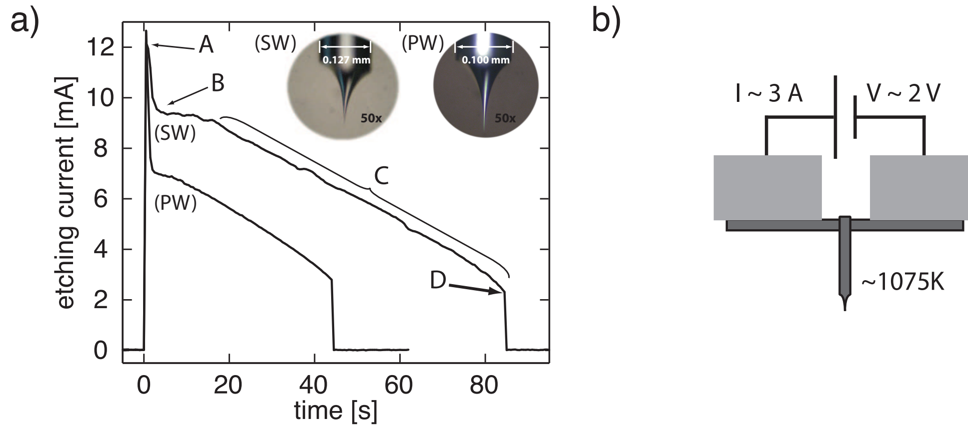

Figure 3.3 a) Etching current versus time shown for a single crystalline tungsten wire (SW) and for a polycrystalline wire (PW). The insets show optical microscopy images (magnification (50x)) of the corresponding tips. b) Resistive heating of the tip to red glow in UHV.

a 1 – 5 Hz modulation.

- Fibers stemming from the air of the laboratory and dust on the liquid surface might force the meniscus to drop. As a consequence a sharp drop in the etching current will cause the electronics to switch off before the *drop-off*.
- A large tilt of the wire will result in an angled tip and should be avoided.
- Air bubbles at the wire surface will move up the wire surface and cause severe disturbances – pre-etching helps since the wire surface gets less rough and the chance of producing these small bubbles during the dipping process is reduced.

3.2 Cleaning the tip: Resistive Heating in UHV

It is a well known fact that several contaminations are left on the tungsten surface after the electrochemical etching besides the native oxide layer that forms on tungsten under atmospheric conditions. Therefore a number of oxides (mainly in the form of WO_3) and residues of KOH are present [57]. Heating the tungsten tip surface to temperatures above 1075 K in UHV causes the following reaction

$$2\,\mathrm{WO_3} + \mathrm{W} \rightarrow 3\,\mathrm{WO_2} \uparrow .$$

This process sublimes the oxide layer along with other contaminations [39] , [50] and thermal diffusion heals structural imperfections. Since a conductive and stable tip for STM operation is needed, these effects are advantageous. In order to realize the heating process, a system was developed in which the tip sits at the end of a spot welded wire T-cross as seen in figure 3.3 b). Stainless steel was chosen for the base of the wire cross, since the spot welding contact is more stable between stainless steel and tungsten than for a tungsten-tungsten weld for the reason that stainless steel has a lower melting temperature (1400 ^{o}C - 1450 ^{o}C for the used type 304, source: British Stainless Steel Association[1]) than tungsten (3422 ^{o}C, source: American Chemical Society[2]).

The resistive heating was performed by running a current through the wire base. Before heating to high temperatures (flash heating) a current of 2 A with a voltage of about 1.5 V was applied for about 5 min in UHV. This degassed the tip and pre-cleaned it from etching residues and air contaminates [58]. Finally the voltage was increased slowly (about 15 – 30 seconds from the degassing voltage to the voltage needed for red glow) until the red glow of the T-cross was observed. The power was left constant for 3 – 5 s and then reduced and switched off (the voltage reduction can be fast).

The voltage was controlled during the heating process and therefore the dissipated power was limited as one can see from $P(V) = V^2/R$. The voltage was controlled and constant unless changed by the user. But the resistance of a metal wire increases with increasing temperature. Therefore the power is limited when controlling the voltage (if the current was controlled, the dissipated power could increase with increased resistance since $P(I) = I^2\,R$). This is important since a rapid increase in the heating power could easily blunt the tip [59]. A change in the resistance of the spot welding contacts during the resistive heating can also lead to a spike in the heating power. A lowering of the resistance due to the improvement of the conductivity of the spot weld junctions has to be expected for the first heating cycle after the tip is introduced into UHV in our setup.

Resistive heating is a useful tool since it cleans the whole tungsten wire. Local heating techniques, such as electron bombardment, cleans the tip only in the apex region and increases the likelihood that residues from the tip shank diffuse towards the tip apex during the STM measurement. Examples of blunted tips and a comparison of different tip cleaning methods can be found in [53]. For the system presented in this thesis, the actual voltage and

[1] http://www.bssa.org.uk/
[2] http://portal.acs.org/portal/acs/corg/content

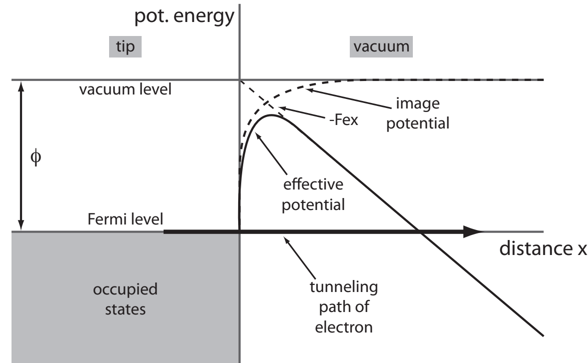

Figure 3.4 Potential diagram for the tunneling process during field emission.

current values for the flash heating varied from tip to tip since the resistance was different for different spot welding contacts. Therefore a visual check was the most reliable control of the process. Mostly a current of about 2.5 – 3.0 A at about 3 – 4 V was used, as shown in figure 3.3 b).

3.3 Checking the tip radius and fine sharpening by field emission

3.3.1 Fowler-Nordheim theory for field emission

Field emission measurements are a well known method to check the tip radius as well as the surface cleanliness and structural stability of the tip. In order to measure a field emission current, electrons were extracted from the STM tip by applying a high voltage between the tip and a counter electrode. The tip was set on negative bias with respect to the counter electrode. Figure 3.5 a) shows the setup for this measurement, the potential energy diagram is illustrated in figure 3.4. The effective potential (the potential an electron sees on the vacuum side) is made up by three major parts: 1) the vacuum level (ϕ) of the tip material (in our case tungsten) 2) the applied electric field ($-Fex$) 3) the image potential of the electron ($-\frac{e^2}{4x}$). By taking the Fermi level as zero level we get

$$U_{eff} = \phi - Fex - \frac{e^2}{4x}. \tag{3.2}$$

The real situation deviates from this formula near x = 0, because short-range interactions set in. However, equation 3.2 is a good enough approximation describing field emission.

As indicated by the red arrow in figure 3.4 an electron could tunnel through this barrier once the barrier is small enough, in other words once the applied voltage is high enough. A very useful description of the resulting field emission current was developed by Fowler and Nordheim in 1928 [60]. The following Fowler-Nordheim equation expresses the process in terms of the emission current:

$$I = \alpha F^2 \exp\left(-0.68\,\frac{\phi^{3/2}}{F}\right) \tag{3.3}$$

where I the emission current (in nA), α a correction parameter, ϕ the workfunction (in eV), $F = V/kR$ the applied field (in V/Å) with tip radius R, k a geometric tip factor. Substituting for the applied voltage, rearranging and taking the natural logarithm gives us the following expression

$$\ln\left(\frac{I}{V^2}\right) = \underbrace{\ln \alpha (kR)^2}_{offset} - \underbrace{0.68\,\phi^{3/2}\alpha kR}_{slope} \cdot \frac{1}{V} \tag{3.4}$$

which is useful for the analysis since we can plot $\ln(1/V^2)$ vs. $1/V$ to extract some information about the tip radius. The slope is used for the radius estimation. Still, two unknowns in this equation which cannot be measured remain. These are α and k. By setting $\alpha = 1$ and the work function to an average value of $\phi = 4.5$ eV of different crystalline planes, kR can be extracted (which is justified in more detail in [51]). The main reason for the complications in the analysis of the field emission current is caused by the fact that the tip shape is not well known when using this method. This results in a great uncertainty in predicting the electric field and thus predicting the shape factor k. For that reason we will only get a range of values assuming the shape factor between 3 and 35 (you will see R_{min} and R_{max} in the Fowler-Nordheim plots according to $k_{min} = 35$ and $k_{max} = 3$). So finally the field emission current will give a good estimate of our tip radius and shows if the tip is worth further treatment. The following conclusions can be drawn from a field emission experiment: 1) stable field emission implies a clean and structurally healed tip surface with no sudden changes due to diffusion or structural rearrangements 2) reaching the threshold emission current (10 nA) at low applied voltage (below 1300 V) means that our tip is sharp

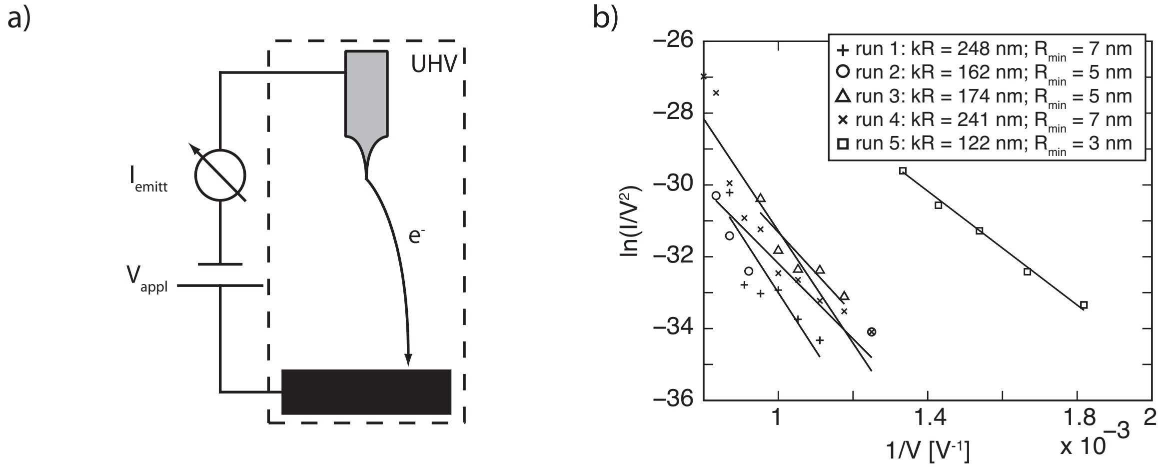

Figure 3.5 a) Field emmission setup. b) A typical Fowler-Nordheim plot.

(high field due to geometry) and clean (low work function). The field ion microscope (FIM) gives us much more accurate information about the tip radius and the atomic structure as discussed below. Actual values of the threshold current and voltage are a function of the geometry of the apparatus.

3.3.2 Refining the tip by annealing/field emission cycles

Figure 3.5 b) shows a set of field emission curves of a single crystalline tip (W(111)) plotted as a Fowler-Nordheim plot [50]. A cycle of several combined field emission and heating runs is shown. It is necessary to do several runs since good tip properties are rarely achieved in the first run. The exact procedure for the 5 curves is:

1. flash heating for 3 s
2. field emission run 1 (up to 1.2 kV)
3. flash heating for 3 s
4. field emission runs 2 (up to 1.7 kV) and 3 (up to 1.1 kV)
5. field emission runs 4 (up to 1.4 kV) and 5 (up to 0.8 kV) one day later

High applied fields, as used in runs 2,3 and 4, improve the tip structure in many different ways. The field enhancement at the tip apex is great and therefore diffusion is enhanced

which leads to an overall smoother tip and might build well structured tip apexes as shown in [61]. Field evaporation of tungsten oxide that was not cleaned by resistive heating is another process which further cleans the tip [50].

The graph for run 5 shows a fit line that has a smaller slope and is shifted to greater 1/V values. In other words the tip was sharper (see the kR and R_{min} values in figure 3.5 b)) and field emitted at lower applied voltages. Additionally, the field emission behavior was more stable, as seen by the small scattering around the fit line. Therefore the tip structure was more stable.

3.4 FIM: Imaging the tip structure at the atomic level

The field ion microscope (FIM) was invented by Erwin Müller as an extension to the field emission microscope (FEM) and gave atomically resolved images in 1956 for the first time [62]. It is very easy to use and provides routinely atomically resolved images of sharp metal tips. It was the first experimental method that allowed to image individual atoms in real space. The method is very useful for the purpose of this work since the tip that is used can be imaged just before and just after the STM/AFM experiment with atomic resolution.

3.4.1 Working principle of the FIM

The operation of the FIM is very simple. An imaging gas (He) was introduced through a diaphragm into the vacuum chamber up to a partial pressure of 10^{-5} mbar. Then a tip was placed in front of a phosphorous screen unit about 5 cm away as shown in figure 3.6 a). Subsequently the voltage applied between the tip and the screen unit was slowly increased until an image was detected. This imaging voltage was usually around 3 - 6 kV and will be mentioned for each image. Sharper tips gave images at lower voltages as explained below. For clean and sharp STM tips FIM is a very reliable and quick method for the analysis of the atomic structure. The whole measurement can be completed within 20 min.

The image contrast is a consequence of selective He ionization at atomic protrusions and not as trivial as the operation of the apparatus. Figure 3.6 b) summarizes the key aspects of the ionization process during a FIM measurement. He gas atoms in close proximity to the tip were polarized and attracted to the tip surface and adsorbed there. The adsorbed He atoms (drawn in cyan) diffused towards local atomic protrusions like step edges (tip surface edge atoms are drawn in white). At these positions they were stabilized by the electric field and caused an additional field enhancement. He atoms close to the tip were

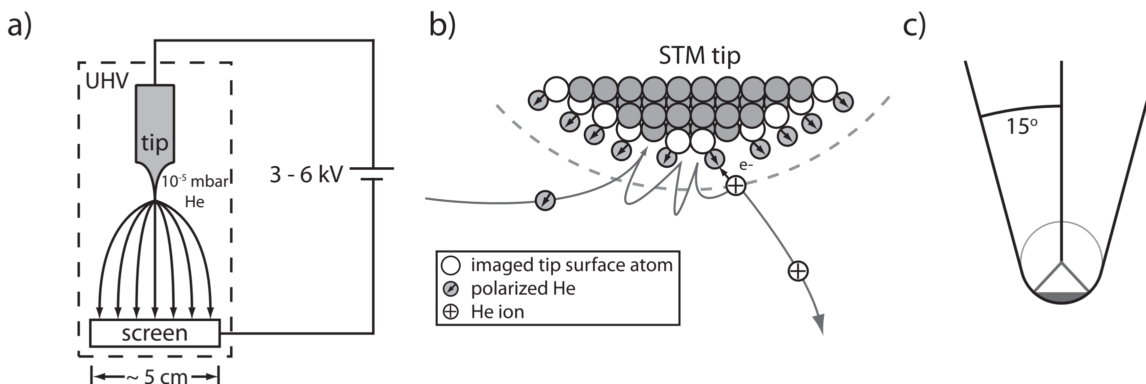

Figure 3.6 a) A schematic of the FIM setup. b) Details of the ionization process during FIM operation. c) Visible area (gray shade at the end of the tip) of a typical STM tip in FIM.

continuously polarized and accelerated towards the tip surface by the electrostatic force. Once these atoms hit the tip surface, the kinetic energy of the atoms was be dissipated via a hopping motion on the tip surface. If the He atom was slow enough after some hopping and was close enough to a local field enhancement, it was ionized and accelerated towards the screen unit by the electric field. There, it triggered an electron avalanche which led to an image spot on the phosphorous screen that sat underneath the multichannel plate. Since the field lines that ran between the screen and the tip all originated from the sharpest point of the tip namely the tip apex, as indicated in figure 3.6 a), a highly magnified image of the tip was obtained on the screen (magnification on the order of 10^7). The gray shade in figure 3.6 c) visualizes the area that was imaged by the FIM for a typical STM tip in the system that is discussed here. Only the very first part of the tip was imaged due to geometric constraints. The drawing represents the field of view of the FIM data shown in figure 3.10. In the following the main aspects of the FIM will be discussed, the ionization process, field evaporation of tip surface atoms, the resolution, imaging gas choice and the temperature dependence. Details and many more aspects of FIM can be found in the books by Miller [63] and Tsong [64].

He ionization

As mentioned before and illustrated in figure 3.6 b), He atoms were ionized at certain ionization sites only. Two conditions constrained the process. First, the He atom had to stay at the position for a sufficient time due to a finite tunneling probability, so the kinetic

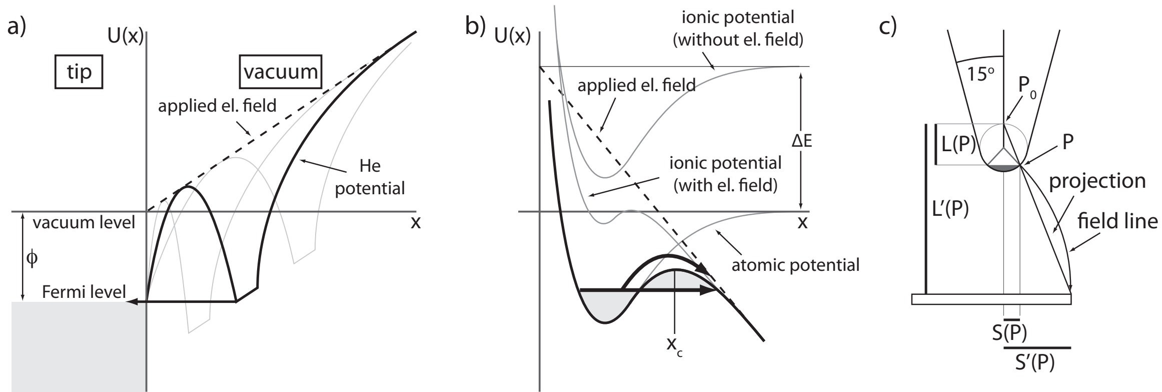

Figure 3.7 a) Potential diagram for the He ionization process. b) Potential diagram for the field evaporation process. c) Magnification of the FIM.

energy had to be low, in other words the atom had to be thermalized. The second constraint was that the ionization took place only at a certain distance from a polarized He atom. Since the STM tip surface was spherical at the apex, a shell can be defined in which ionization took place. This so called ionization disc had a distance from the surface of about 0.4 nm and a thickness of 0.02 nm [64]. The reason for that can be found in the potential diagram for the ionization process, illustrated for the one dimensional case in figure 3.7 a). The solid black line on the vacuum side represents the potential of the electron in the He atom. It is possible for the electron to tunnel into the tip surface in this situation, indicated by the arrow. For a position closer to the sample, drawn in gray, the barrier is even smaller and can be tunneled through except for the problem that all states at that energy are filled, since the energy of the electron is below the Fermi level. Positions that are further away, sketched in gray as well, result in a barrier that is too wide to penetrate.

Field evaporation

In addition to the ionization of the imaging gas, the tip material can be ionized as well and expelled from the tip surface. This process is called field evaporation. Atoms adsorbed on the tip surface can be removed in the same way, the so called field desorption, which follows the same physics as field evaporation. The process is complex and many theories were tested in order to understand the process in detail (chapter 2.4 in [63] and chapter 2.2 in [64]). A brief summary is given here to describe the fundamentals. The initial condition, the neutral bound or adsorbed atom, and the final condition are well established, while

different pathways can lead to the ionization of the surface or ad-atom and seem to depend on the nature of the tip material.

Figure 3.7 b) illustrates the potentials involved in a one dimensional fashion. The initial state in which the atom is bound to the surface, is represented by a binding curve that describes the atomic potential. A similar curve can be drawn for the ionic potential of the ion, offset by an energy

$$\Delta E = \sum_n nI_n - n\phi \tag{3.5}$$

that contains the ionization energy of each ionization of a ion in the nth ionization state and the workfunction contribution that each electron requires to leave the atom. Both curves represent the situation in the absence of an electric field. If an electric field is applied, the potential will be the result of the superposition of the potential of electric field and the ionic/atomic potential. A so called Schottky hump develops through the influence of the electric field. Since the field is gradually increased the position of the hump is appearing on the right of the atomic potential. The position can be estimated by the assumption that only the image potential $U_{im} = (n\,e)^2/(16\,\pi\,\epsilon_0\,x)$ and the energy of the electric field $U_{el} = -n\,e\,F\,x$ influence the situation. Then the position of the hump is at the point where they cancel each other

$$x_c = \frac{1}{2}\sqrt{\frac{n\,e}{4\,\pi\,\epsilon_0\,F}}. \tag{3.6}$$

This is called the critical distance since an atom that reaches the hump is classically allowed to leave the surface and be ionized. Clearly this classical path is influenced by the temperature of the tip surface. If the temperature is large enough so that thermally induced vibrations reach amplitudes of the order of the critical distance, the surface atom can escape. Another pathway besides the classical escape would be the tunneling through the barrier as indicated in the drawing. This process is not discussed here and can be found in detail in [63] and [64]. In both models the hump or the tunneling barrier are influenced by the electric field. Another fact that was characterized experimentally is the post ionization of ions. In the case of tungsten the third ionization state, W^{3+}, was measured as the most common one.

An important check has to be performed before investigating a new tip material with

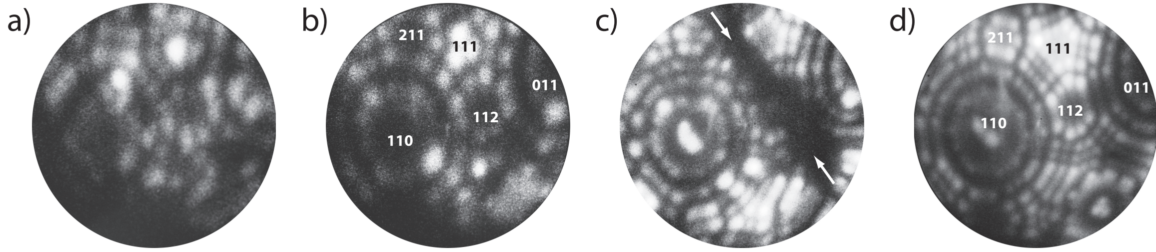

Figure 3.8 a) FIM image of a single crystalline tungsten tip (W(111)) after an initial cleaning and one day of storage in UHV. The image is taken at 3.0 kV. b) The same tip after cleaning with field evaporation at about 5.0 kV. The image is taken at 3.0 kV and a tip radius of $r_{tip} = 3.7$ nm is estimated by the ring counting method. c) Same tip after a tip crash. The dark areas show that the impact has deformed the tip. The imaging voltage was 5.4 kV. d) Same tip after field evaporation (imaging voltage again 5.4 kV, $r_{tip} = 6.1$ nm). The displaced layers were evaporated and the single crystal apex structure is re-gained.

FIM. Since the image gas ionization and the field evaporation depends on the field strength, a scenario is possible in which the field evaporation happens before the image gas ionization. In that case no image would be detectable as the surface atoms are evaporated before they can be imaged. For tungsten the imaging field at which ionization occurs has a value of $F_{evap.} = 57$ V/nm, helium is ionized at 44 V/nm and therefore tungsten can be imaged with helium. But gold for example is field evaporated at $F_{evap.} = 35$ V/nm and would need to be imaged with an imaging gas like hydrogen which is ionized at 22 V/nm [51].

Figure 3.8 shows how field evaporation can be used to clean a tip from adsorbates and restructure the surface. The initial structure shows large dots that can be attributed to adsorbates as they protrude from the surface and therefore ionized the imaging gas at a higher rate due to the local field enhancement. Step by step the evaporation took layers off the tip which is monitored visually. Once a clean and stable structure was obtained, the voltage was lowered and the structure is checked for stability. That means it was left for a few minutes at a low imaging voltage and visually checked. In the example the initial imaging voltage was $V = 3.0$ kV in fig. 3.8 a), then the voltage was raised to about $V = 5.0$ kV for the evaporation process and finally the stability check was performed at $V = 3.0$ kV for the image in fig. 3.8 b). The ring counting method, see equation (3.9), was employed to estimate the tip radius. Counting the number of steps between the [1 1 1] and the [1 1 0] plane, one obtains $n = 3$ and a tip radius of $r_{tip} = 3.7$ nm. The crystal planes are labeled in the figure. As figure fig. 3.8 c) and fig. 3.8 d) show, this procedure can even re-gain the

original structure after a mild tip crash. The tip shown in fig. 3.8 b) was approached to the sample and a during STM operation a tip crash occurred. Still a FIM image was obtainable for this tip and it is shown in fig. 3.8 c). The imaging voltage needed to ionize the imaging gas increased to 5.4 kV due to the blunting of the apex structure. Still single atoms were resolved. A dislocation line indicated by the white arrows is clearly visible. This dislocation structure was field evaporated and the underling single crystal structure was exposed. The final structure had a radius of $r_{tip} = 6.1$ nm with a layer count of $n = 5$ between the [1 1 1] and the [1 1 0] pole.

Magnification

The magnification of the field ion microscope can be estimated very easily by a simple geometric approach. Since the imaging of a given point P on the tip surface can be approximated by a stereographic projection, the definition for the magnification of a microscope can be directly applied. Figure 3.7 c) illustrates the process. The black curved line exemplifies the real trajectory along the electric field line of an ion that leaves the tip surface at point P. This process can be approximated by a stereo projection of that point on the screen which is illustrated as straight black line in the figure. In a stereo projection the projection line is drawn from a point which lies where the back side of the tip apex sphere cuts the tip sample distance axis, marked as P_0 in fig. 3.7 c), through the point that is projected. The proportions of the drawing do not match the real situation, in reality the dimensions of the tip radius ($r_{tip} \simeq 5$ nm) and the distance (tip-screen distance = 5 cm) differed by seven orders of magnitude. A distribution of the electric field lines for two geometries can be found in appendix B. Labeling the distance from the tip apex center perpendicular to the tip–screen distance axis $S(P)$ and the imaged point $S'(P)$, the distance of P from the stereo projection point $L(P) \simeq r_{tip}$ and the distance of the screen to the projection point $L'(P)$, the magnification M can be estimated using:

$$M = \frac{S'}{S} = \frac{L'(P)}{L(P)} \simeq \frac{5\text{ cm}}{5\text{ nm}} = 10^7. \tag{3.7}$$

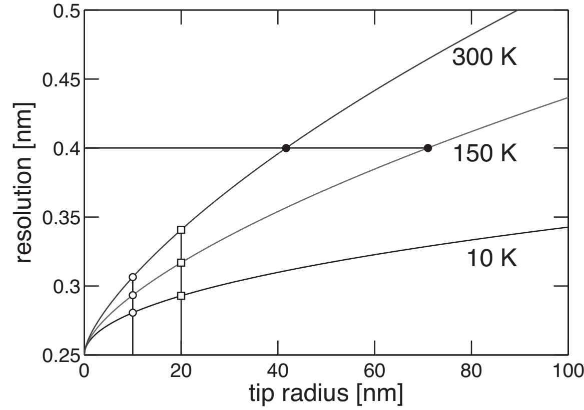

Figure 3.9 The resolution of FIM in dependence of the tip radius for three temperatures.

Resolution

Another characteristic parameter of the FIM instrument is the resolution. As described in [64], the resolution δ of the FIM can be characterized with

$$\delta = \sqrt{\delta_0^2 + \frac{4\,\Lambda\,\hbar\,r_{tip}^{1/2}}{(2\,m_{IG}\,k\,e\,F_0)^{1/2}} + 16\,\frac{\Lambda^2\,k_B\,T r_{tip}}{k\,e\,F_0}} \tag{3.8}$$

where δ_0 is the diameter of the imaging disc above each imaged atom, which can be approximated as 0.25 nm [63]. Its value has been calculated in two ways in [65], here for simplicity we assume that the value is only dependent on the atomic species and that it is constant. The second term expresses the contribution from the Heisenberg uncertainty principle and the third term takes the lateral movement due to the thermal motion into account. The used parameters are: Λ a geometrical factor linked to the magnification, using formula (2) in [65] and equation (3.7) it is evaluated to be 1, $\hbar$ is Planck's constant, r_{tip} the tip radius, $m_{IG} \simeq 3.2 \cdot 10^{-27}$ kg the mass of the helium gas ion, k a geometric factor that can be approximated to be 6 according to [65], e the charge of an electron, $F_0 = 44$ V/nm the ionization field for helium, k_B Boltzmann's constant, T the temperature. Figure 3.9 shows a plot of the resolution in dependence of the radius for three temperatures. For the limit of $r_{tip} \rightarrow 0$ nm the resolution approaches the value of the local ionization disk for all temperatures and with increasing tip radius the resolved feature size increases. Since the

smallest inter-atom distances in the tungsten (111) projection are about 4 Å = 0.4 nm as indicated in figure 3.14 b), this would be the threshold resolution for atomic resolution in the FIM system and is marked in figure 3.9 with black circles. According to this estimate, the resolution criteria would allow FIM with atomic resolution of tips with a radius of about 40 nm at 300 K and about 70 nm at 150 K. A limitation on the tip radius is posed by the critical field for the ionization of the He gas atoms $F_0 = 44$ V/nm. Since apparatus properties limit the maximum applied tip voltage to about 7 kV, only tips with a radius smaller than 20 nm have a local field at the tip apex of about 44 V/nm in an applied tip voltage range of 4–7 kV. Keeping this restriction in mind, a check of the resolution behaviour for $r_{tip} \leq 20$ nm leads to the conclusion that even at room temperature atomic resolution is achievable. Empty squares mark the resolution values for $r_{tip} = 20$ nm and empty circles the values for $r_{tip} = 10$ nm in figure 3.9.

FIM imaging of tungsten at room temperature is therefore possible and was done throughout the work presented here. The apparatus allowed cooling of the FIM/STM/AFM measurement system with liquid nitrogen down to temperatures of $T = 150$ K. This would have been advantageous for two reasons. First, the resolution would have been increased as shown in the third term of equation (3.8). Another benefit of low temperature conditions is the increased barrier for field evaporation and field desorption. The complete experimental sequence used in this work consists of the FIM imaging, then a STM/AFM imaging and spectroscopy session followed by the characterization of the tip. This final FIM imaging showed the amount of structural modification that the tip experienced. Adsorbates and minor structural changes are expected. In the procedure of FIM imaging the tip bias voltage was increased until the imaging gas was ionized and an image was detectable on the screen. Field desorption of loosely bound adsorbates might happen in the field region where no image is detected and therefore leave the tip surface unnoticed at room temperature. Cooling of the system with liquid nitrogen would increase the likelihood to visualize the adsorbates for the reason that the critical field for field desorption is enlarged at lower temperatures. All the experiments presented here were measured at room temperature due to practical constraints.

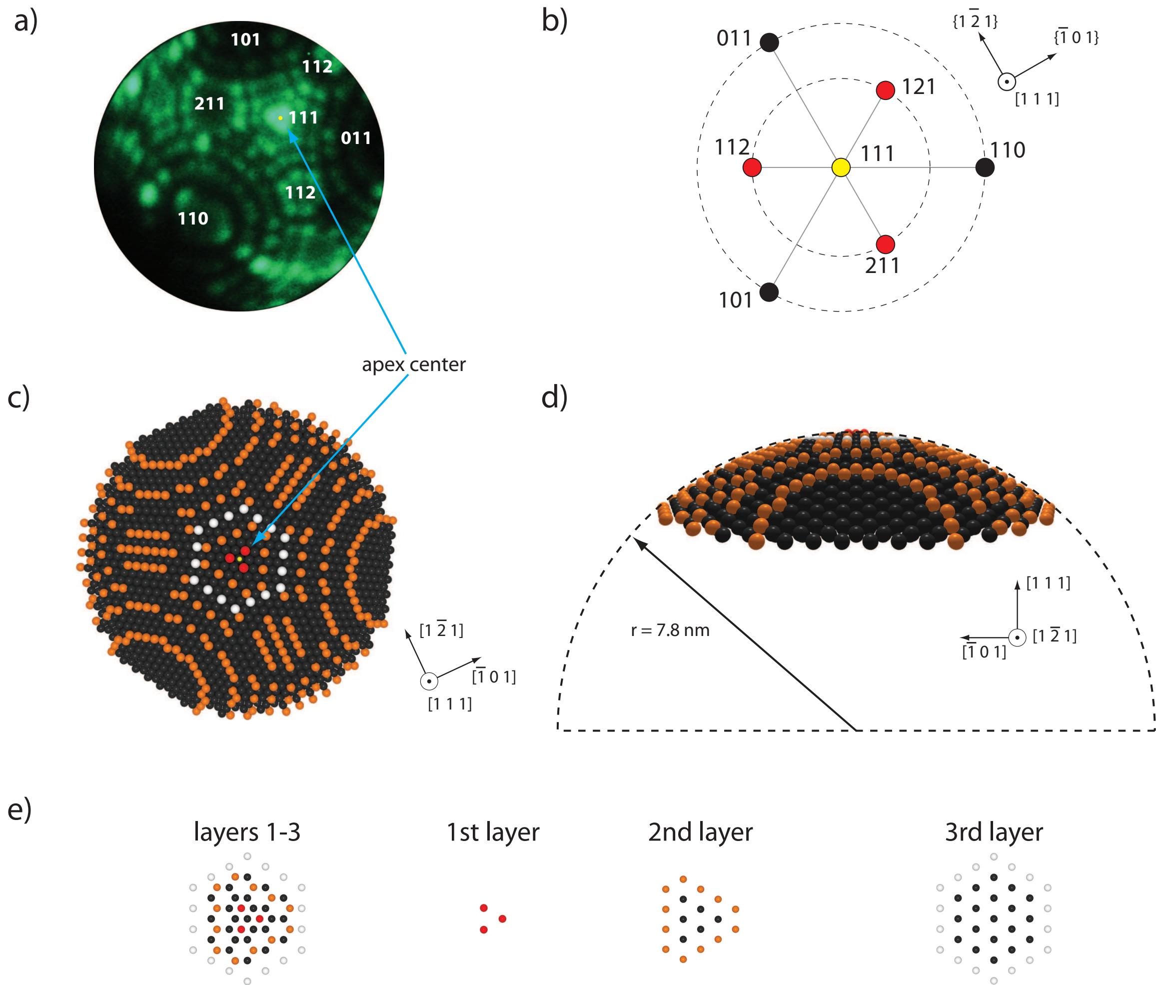

Figure 3.10 a) Typical FIM image of a W(111) tip acquired at 4.8 kV and room temperature. Low index crystal planes are labeled. The apex center is marked with a yellow dot. b) Reduced facet projection map for a bcc(111) FIM tip. c) Three dimensional ball reconstruction of the FIM image shown in a) as top view. The apex is marked with a yellow spot as well. The crystallographic directions are given on the lower right. d) Side view on the ball model from the $[1\bar{2}1]$ direction. The radius of $r = 7.8$ nm is illustrated by the dashed line. e) Decomposed layers one through three.

3.5 Reconstructing the atomic structure of the tip

3.5.1 Image interpretation

A typical result of a FIM measurement of a W(111) single crystalline tip can be found in figure 3.10 a). The image shows a green contrast where the imaging gas ions hit the screen unit. If the tip is clean and some layers have been field evaporated, the pattern on the screen resembles certain characteristic patterns that represent crystallographic planes of the tip. The low index planes close to the apex center were identified and labeled. The center is marked with a yellow dot. The fact that the center of the tip is not in the center of the image was an artefact due to the apparatus that was used. Moving the tip allowed us to center the apex structure but bared the risk of destroying the tip due to the manipulator action. The path of the electric field lines was not symmetric and therefore the image was displaced and distorted. Another apparatus induced effect was the limitation on tip radii. Only tips with a radius $r \leq 15$ nm could be imaged due to the limitation of the tip voltage. The wire that connected the tip to the feedthrough was used for both the high voltage for FIM and the low current of the STM. For that reason a compromise had to be found and the result limits the voltage to 7 kV. For tips with $r \geq 15$ nm the image gas ionization cannot be achieved at $V \leq 7$ kV.

In figure 3.10 b) the reduced facet map for a W(111) tip, a bcc (111) oriented crystal, is given. The map is obtained by stereo projection. Details on the procedure can be found in [64], [52] and [51]. As already obvious from a), the structure has a three fold symmetry. Part c) of the figure illustrates the three dimensional ball model reconstruction of the FIM image shown in a) as top view. The apex center is marked with a yellow dot as well. The crystallographic directions are given on the lower right of the figure. In part d) a side view of the reconstructed tip from the $[1\bar{2}1]$ direction is displayed. The spherical shape of the tip apex is indicated with a dashed line for a radius of $r = 7.8$ nm. The following section explains the procedure of tip reconstruction.

3.5.2 Image reconstruction

Figure 3.11 illustrates the selection process for the tip atoms that formed the three dimensional ball model. The principle behind the reconstruction is quite simple and relies on a method first introduced by Moore [66]. It was assumed that the tip apex had a spherical shape. Since the crystal orientation was known, a cube with the dimensions $2\,r_{tip}\times 2\,r_{tip}\times r_{tip}$

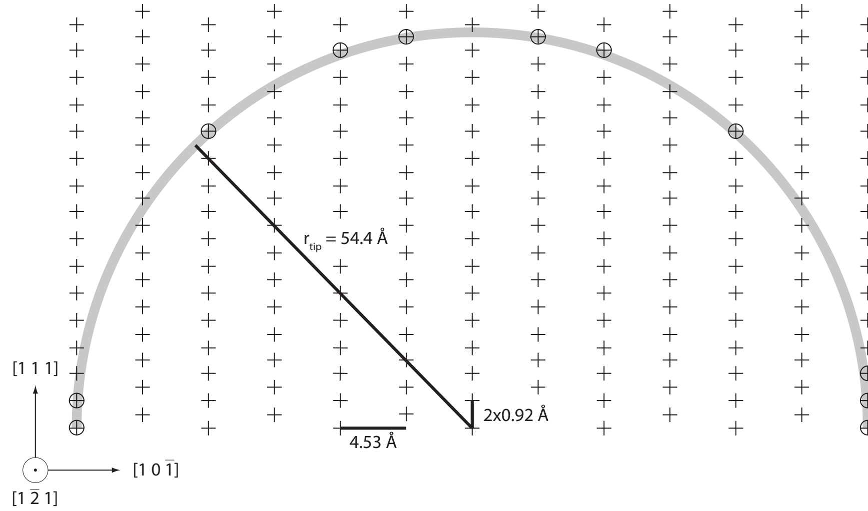

Figure 3.11 Tip atom selection for tip reconstruction for a radius of $r_{tip} = 5.4$ nm.

was constructed and the positions inside the cube were calculated for the crystallographic orientation of the tip material. For tungsten (111) oriented tips a bcc(111) crystal structure was needed. In reality one would choose a cube that is slightly larger to have a greater choice on the sphere center coordinates. In order to obtain a tip from this cube, a shell of a certain thickness was defined, so that all atomic positions that fell into this shell were sorted out and assumed to be tip atoms that were imaged by FIM. For simplicity the diagram contains only one layer. The shell is drawn a gray semicircle and selected atoms located inside the shell are circled.

The example diagram is done for a tip with a radius of $r_{tip} = 5.44$ nm and a shell thickness of $\delta r_{tip} = 0.07$ nm which is drawn as a gray semicircle contour. The radius was chosen so that the sphere contains six atomic translations of 0.45 nm in the $[10\bar{1}]$ and about 30 layers with a plane spacing of 0.09 nm in the [111] direction. Details on vector translations and characteristic distances for bcc(111) oriented layers are given in the appendix. The description above was given in order to visualize the selection process. The next step would be to discuss a real example.

In an attempt to reconstruct a real tip from a FIM image, e.g. the one shown in figure 3.10 a), the first step was to estimate the tip radius from the distances of the plane centers in the FIM image by using the so called ring counting method [50], which states

that

$$r_{tip} = \frac{n\,s}{1 - \cos\theta} \tag{3.9}$$

yields the tip radius. Using a layer count of $n = 6$ between the apex pole [1 1 1] and the [1 1 0] pole with $s = 2.23$ nm and an angle of $\theta = 30^o$ between the pole directions, a radius of $r_{tip} = (7.3 \pm 1.2)$ nm was obtained. Included in the result was a counting error of $n = 1$ with the resulting uncertainty of the tip radius $\Delta r_{tip} = 1.2$ nm. A three dimensional ball model that matched the original FIM image was obtained by using a tip radius of $r_{tip} = 7.8$ nm and a shell thickness of $\delta r_{tip} = 0.03$ nm for the reconstruction. The resulting structure is illustrated in figure 3.10 c) and d). Manual corrections were necessary in order to match the real image for the first three layers. The origin for this is that desired tip shapes with a three atom termination can be achieved by careful use of the field evaporation method but tips reconstructed in a spherical manner produce structures that miss the apex structure for reasons of geometry – a spherical cut for large radii excludes the three atom apex since the curvature of the three atom structure is higher than the curvature of the spherical shell. Different cutting shapes can be used. In [67] a Lame shape that resembles a spherical to triangle cross section has been tested for bcc(110) orientations. These structures have cylindrical symmetry and the reconstruction result was improved. But in the case of the bcc(111) tips the difference between the real structures and the reconstructed ones were still present and made adjustments of similar effort necessary. Therefore the spherical cut is used for the analysis here.

In the final result several differences between the original FIM image and the ball model are still visible. The differences in the original FIM image in figure 3.10 a) hints to another difference between the perfect spherical and symmetric situation of the model and the real tip. A comparison of the [1 1 2] and the [2 1 1] plane in in figure 3.10 a) indicates that the field evaporation process for different positions on the tip surface was not always symmetric. An atom by atom reconstruction of the whole tip structure that is visible in the FIM image would be too costly in terms of time. Since the tip radius and the apex structure of the first three layers are the most important tip parameters in the case of simultaneous STM/AFM non-contact approach curves, the reconstruction has been accepted once the radius of the ball model matched the result from the ring counting method [50] and the structure of the first three layers matched the original FIM image.

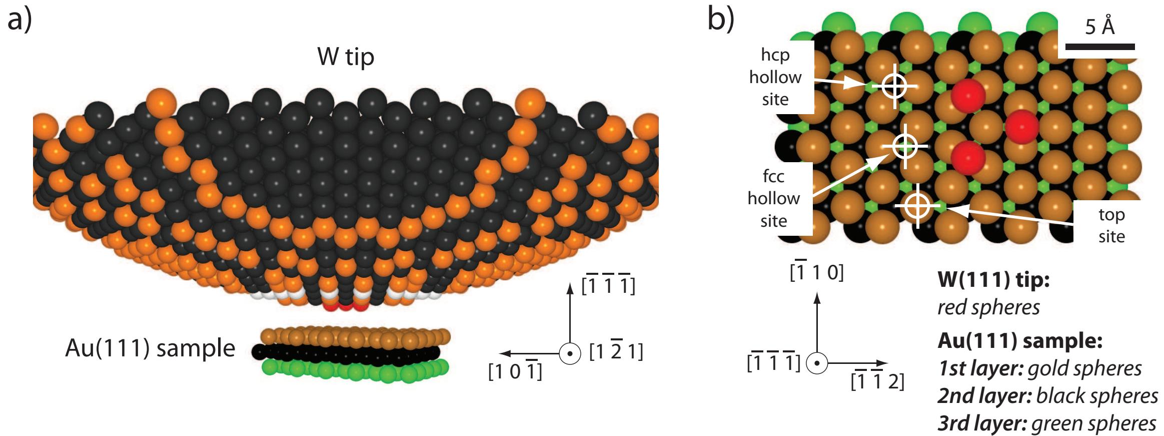

Figure 3.12 a) Reconstructed tip from figure 3.10 facing three layers of Au(111) sample atoms (side view). The tip sample distance is 5 Å. b) Top view of the three terminating tip atoms centered around the top site. The three high symmetry points on unreconstructed Au(111) – the top site, the hcp hollow site and the fcc hollow site – are shown in the drawing.

3.6 Realistic Tip–Sample Geometry

As described in section 3.4, FIM images were taken at room temperature just before the STM experiments. These images were reconstructed as three dimensional ball models. Figure 3.10 shows an example analysis. The acquired FIM image is presented in fig. 3.10 a). A yellow dot marks the apex center. Figure 3.10 b) displays the three dimensional ball model of the tip that was imaged with FIM. Again, the apex center is marked with a small yellow marker for orientation. Technical details on the reconstruction and on the crystal plane patterns can be found in section 3.5. The crystallographic directions are indicated by vectors to the lower right of each image. The reconstruction for a tip radius of $r_{tip} = 7.8$ nm matches the FIM image. The side view from the $[1\ \bar{2}\ 1]$ direction, that is presented in fig. 3.10 c), exhibits the spherical shape of the tip. An unrelaxed STM tunnel junction using this tip and three layers of unreconstructed and unrelaxed Au(111) is shown in figure 3.12 a). In order to judge the area covered by the three atom apex, a simplified version of the gap is shown in fig. 3.12 b) as top view. The tip has been reduced to only the three apex atoms (in red) and the view from the $[\bar{1}\ \bar{1}\ \bar{1}]$ direction illustrates that a STM image taken with this tip would not yield atomic resolution, since the apex stretches over three hollow sites and a top site while being centered on a top site. The symmetry

positions on the unreconstructed Au(111) surface – the hcp hollow site, the fcc hollow site and the top site – are also displayed in the figure. Another interesting point can be made. Since the sample and tip have most likely a rotation against each other in the experiment, it is highly unlikely for the apex atoms to approach simultaneously on top of one of the symmetry sites. In this case a rotation is defined as a rotation around the long axis of the tip assuming an alignment of the tip (111) direction with the sample surface normal the case in which the sample surface normal is not aligned with the (111) direction of the tip will be discussed as tilt in the next section. Therefore we would expect features of hysteresis in the current and the force signals due to the positional shift of the atom positions during the bond formation on the approach and bond breaking during the retraction as predicted by Caciuc et. al. [68], [69].

A limitation of FIM is that the tip imaging can only be done before and after the STM experiments. Therefore processes like adsorption of rest gas atoms or a sample atom that might occur during the STM measurement cannot be monitored in this way. A severe rearrangement of the gap as shown in section 5.3 can be excluded during the STM scans and for non-contact approach curves, since the necessary indentation depth is avoided and the signatures in the current and force data of this restructuring have not been seen for non-contact curves. As the field evaporation method yields tips with a three atom apex, the resolution of the STM scans before non-contact sequences is not sufficient to resolve the atomic structure of the sample. However, flat terraces and a faint Au(111) herringbone can be identified. It would be useful to simulate STM scanning and approach curves of a W(111) three atom tip on a Au(111) sample in order to see how well the assumptions made here would match a calculation.

Tilt and Structural deviations

Apart from the position on the sample and the rotation of the tip versus the sample, the tip structure itself can have two trimer termination structures. Since the W(111) tip has a bcc(111) apex structure with a three fold symmetry and an ABCA stacking, two orientations of the three atom apex are possible. Figure 3.13 illustrates the possibilities. In fig. 3.13 a) a FIM image of the the first variation is shown. It was acquired at an imaging voltage of $V = 4.8$ kV and is the tip characterized in figure 3.10. The low index planes are labeled in the photo. Figure 3.13 b) shows the reduced projection map for the image shown in fig. 3.13 a). The apex structure, drawn in gray in the projection map, is characterized by

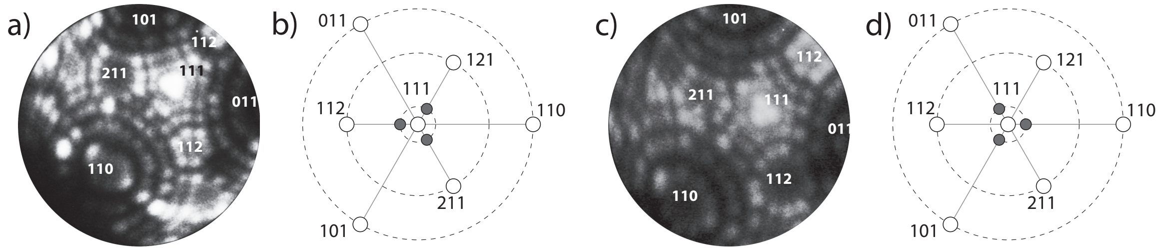

Figure 3.13 a) FIM image of tip SW tip (same picture as fig. 3.10 a) with r_{tip} = 7.3 nm). b) Reduced zone map of the structure in a). The apex atoms point into the direction of the {1 1 2} planes. c) Another tip with the same radius. d) Reduced zone map of the tip in c). The apex atoms point to the {1 1 0} planes in this case.

its orientation with respect to the low index planes. In the case shown in fig. 3.13 a) it directs to the close {1 1 2} equivalent planes. If the layer that produces this structure is labeled as A, the next layer B will have a trimer structure as illustrated in fig. 3.13 c) and d). Figure 3.13 c) shows the FIM image for this case recorded at $V = 5.2$ kV. Again the low index planes are labeled. In fig. 3.13 d) the reduced projection map indicates that the apex structure (in gray) is rotated against the one in fig. 3.13 a) and b) by 60° and directed towards the {1 1 0} equivalent planes. Atoms of layer C cannot form a trimer structure since it has an atom aligned with the symmetry center of the tip. This can be explained by the layer decomposition in figure 3.10 e). If one focusses on the center of the structure of layers one through three, it is obvious that for the first two layers a center can be found so that three atoms form a triangle around this center. For layer three an atom would be in the center and instead of a triangular structure, a hexagonal structure is formed. This phenomenon is a property of the reconstruction program and has been observed for real tips.

Another parameter that should be considered, is the tip tilt defined as the misalignment of the tip axis with respect to the wire axis as indicated in figure 3.14 a). First the tilt that is inherent to the orientation of the crystal structure will be discussed. The wire that we use has a bcc(111) orientation along the wire axis. The uncertainty of the orientation is below 2° as claimed by the manufacturer[3]. In the case of polycrystalline tungsten wire an x-ray study has been performed together with a presentation of an enlargement of grain sizes through annealing [70]. The conclusion of this study was that the grains have a preferred direction

[3] http://www.a-p-tech.com/selections.htm

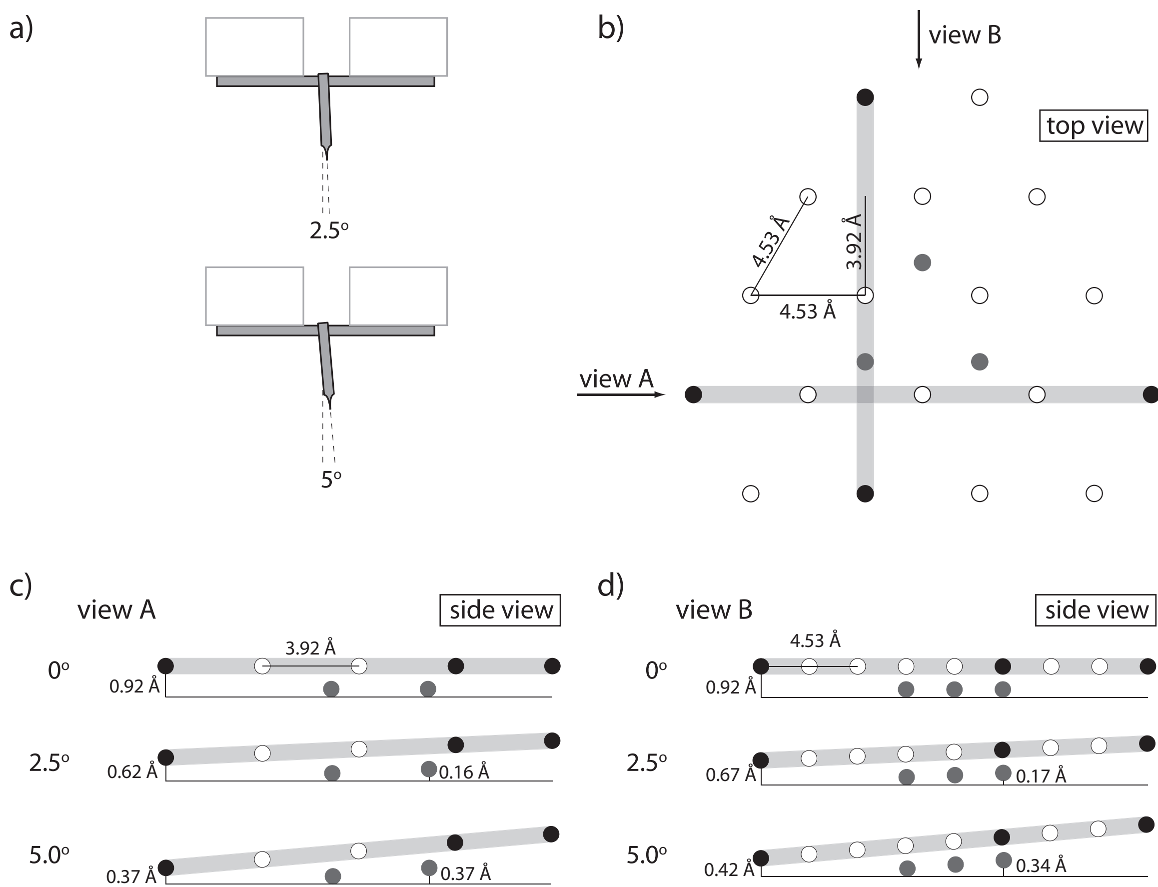

Figure 3.14 a) Tilt of the wire cross versus the perfect perpendicular orientation. b) The first two layers of a three atom tip reconstruction. The three tip atoms are drawn in red, the second layer in black and white – compare with fig. 3.10. c) Side view A of the structure shown in b). The solid line represents a perfectly flat sample. Distances of corner atoms to the sample for different tilts are given. d) Side view B of the structure shown in b) with atom-sample distances. The geometry for a one atom tip is given in figure A.3.

and are oriented within 5° in the bcc(110) direction along the wire axis. Annealing extended the grain size and therefore the single crystal domains up to centimeters and therefore the orientation of the tip apex for these annealed wires can evaluated more precisely than in the case where the wire has not been annealed.

As figure 3.14 a) displays, the wire cross that is used to hold the tip is spot welded and the orientation has a slight deviation from the perfect perpendicular case. A deviation of less than 2.5° was achieved for all of the tip that were used in the recorded data presented here. Tilts of 5° or more were detected visually and corrected for by a gentle bend with tweezers. In order to illustrate the effects of a tilt on the atomic level, the structure of a three atom tip has been drawn in figure 3.14 b). The three tip atoms are displayed in gray and the second layer in either black or white. Two views are defined to estimate the distance changes for different orientations as indicated in the drawing. Figure 3.14 c) illustrates the changes in the tip-sample distances for two corner atoms in a side view. The dimensions for a tilt around an axis parallel to the view axis B is drawn in figure 3.14 d). A tilt of 5° might bring the corner atoms of the second layer into tunneling and a DFT simulation of this case would be interesting in order to check the electronic behaviour of a non-symmetric case. The geometry for a one atom tip is given in figure A.3 in the appendix.

CHAPTER 4

Forces, Conductivity and Relaxation

The goal of this study is the characterization of atomic contacts in the form of metal-metal SPM junctions, where the atomically characterized W(111) STM tip is used as one electrode and the atomically flat Au(111) sample as second electrode. Two physical parameters during an approach are measured, namely the current via the STM circuit and the force via the cantilever deflection. Since tip-sample forces are always present if any kind of material – metal, semiconductor or non-conductor – is brought into close proximity (distances of several Å), they will be described first. These tip-sample forces can be separated into a long range background that is caused by van der Waals and electrostatic forces, which can be described by analytical models that take the mesoscopic geometry into account, and short range so-called chemical forces that arise due to the overlap of tip and sample wave functions. These short range forces can be approximated in a binding model for dimer configurations that yield interaction strength and range information as first order approach for an order of magnitude estimation. This dimer model treats the tip and sample as only two approaching atoms. In section 4.1 theoretical descriptions of long range and short range forces will be introduced and in chapter 4.2 the analytic models will be applied to experimental data with respect to the long range background and the short range scaling.

Real structures have a more complicated geometry and tip sample forces cannot be described in a closed analytical model. Numerical approaches will be mentioned in section 4.1. A realistic picture is not only taking the initial more complex structure into account but also the development of the structure due to the increasing tip-sample interaction force

upon an approach. Increasing tip-sample forces are deforming the gap structure once the tip-sample distance is on the order of inter-atomic distances (separations smaller than 5 Å). This deformation is called relaxation and is a key concept in the analysis since it accounts for deviations of measurement results from simple theoretical models [40], [41]. The amount of relaxation of the gap is dependent on the material and the approach site. It cannot be determined in a closed analytic expression and is simulated in numeric calculations as described in section 4.1. The conductive properties of the gap are strongly influenced by gap structure relaxations as discussed in section 4.3.

Since the description of tip-sample forces, the resulting relaxation and the influence on the conductance is a subject that is currently researched, a summary of recent key publications is given here in order to introduce and discuss results. These are used for the analysis of the W(111)–Au(111) system in the final chapters of this thesis.

4.1 Forces and Relaxation

The system investigated in this thesis consists of a metallic tip facing a metallic surface. Both are non-magnetic and therefore the measured force should be dominated by the electrostatic and the van der Waals force in the long range regime (from great distances down to distances on the order of inter-atomic distances) and so called chemical or short range forces that arise due to the overlap of the tip and sample wave functions in a regime where the separation of tip and sample is on the order of atomic distances. The long range forces can be determined by the analysis of parameters like the mesoscopic tip shape and the mesoscopic electric field in an analytic fashion as seen below. In the case of short range forces the situation becomes more complicated for the reason that the chemical forces are very dependent on the atomic structure of the tip-sample gap. An additional complication is the fact that short range forces themselves cause relaxations and therefore change the tip-sample gap geometry.

Figure 4.1 shows an example of the electrostatic force (F_{el}, dashed line), the van der Waals force (F_{vdW}, dashed line) and a chemical short range force (F_{chem}, solid line) for realistic parameters. These are added to show an example of a total force (F_{total}, solid line). This total force is what an AFM measures because it cannot measure the interaction forces selectively. Since the more interesting part of the measured force is the short range part, the long range forces have to be determined and subtracted before an analysis of the short range forces can be done. As shown later, in data that is analyzed in this thesis, the

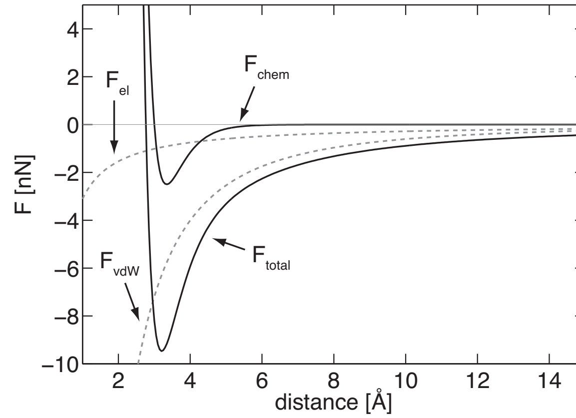

Figure 4.1 Forces in scanning probe microscopy. The curves have been calculated with the following parameters: tip-radius $r_{tip} = 10$ nm, Hamaker constant $H = 4 \cdot 10^{-19}$ J, cone opening angle $\alpha = 5$ deg, bias voltage $V_t = 0.6$ V, L = 100 nm. The geometric parameters have been confirmed experimentally by scanning electron micrographs for tips used in this thesis. The chemical force is modelled by the derivative of a Morse potential with $E_{max} = 0.5 \cdot 10^{-18}$ J, $\lambda = 0.5$ Å, $z_0 = 3$ Å. The total force is the sum of all forces that were mentioned before.

electrostatic force and the van der Waals force are not large enough to have a noticeable influence, since the radii of our tips ($r \simeq 10$ nm) and the used bias voltages ($V_t \simeq 50$ mV) were quite small.

4.1.1 Electrostatic force

In order to obtain a force distance relationship for a SPM setup, we have to assume a geometry that models the real situation quite well. Two models have been found useful to describe the electric field between a nano–tip and a flat sample as presented in appendix B. One would be the spheroidal hyperboloid model that allows a nice geometric display of equipotentials and field lines and is used in the analysis of FIM ion trajectories. As shown in figure B.1, this model is only suitable for tip–sample distances greater than $4\,r_{tip}$. The other approach assumes a flat sample and a tip that is represented by a cone that is capped with a sphere with the tip radius. This model will be used in the following. Figure 4.2 a) shows a drawing of the geometry. In order to illustrate the geometry in tunneling contact and during the spectroscopy, the insets (i)–(iii) give dimensions for various gaps. Using this model, the following force distance relationship has been developed by Hudlet et. al. [71].

The given form is taken from [72] (details are given in section B.2):

$$\begin{aligned} F_{el} &= -\pi\epsilon_0 (V_t - V_C)^2 \left\{ \frac{R}{s} + k(\alpha)^2 \left(\ln\left(\frac{L}{s+R_\alpha}\right) - 1 \right) \right. \\ &\quad \left. - \frac{R[1-k(\alpha)^2 \cos^2(\alpha/\sin(\alpha))]}{s+R_\alpha} \right\} \end{aligned} \tag{4.1}$$

with the tunneling bias voltage V_t, contact potential V_C, tip radius R, tip sample distance s, cone opening angle α, $k(\alpha) = 1/\ln(\cot(\alpha/2))$, tip length L ($\gg s$) and $R_\alpha = R(1 - \sin(\alpha))$. A good approximation can be obtained for the imaging and spectroscopy conditions used in this work. In the distance range of $0 \leq z \leq 1$ nm the approximation for $z \ll R$ is accurate enough ($z/R = 1\text{nm}/10$ nm). The bias voltage has been varied in magnitude and polarity in reference experiments and only for voltages larger than 500 mV a noticeable background due to the electrostatic force has been detected. The contact potential seemed to be centered at $V_C = 0$ V for approach curves done for the W-Au(111) system. An influence of the contact potential was not noticeable. Taking all that into account, one obtains:

$$F_{el} = -\pi\epsilon_0 R V_t^2 \frac{1}{s}. \tag{4.2}$$

Figure 4.2 b) shows curves that have been calculated for different bias voltages V_t as labeled in the graph. The solid lines show the result according to equation 4.1 and the dashed line according to equation 4.2. The simplified version describes the situation quite well. For comparison, the van der Waals force (F_{vdW}) for the same geometry is also plotted.

In the analyzed experimental results, only bias voltages below 100 mV have been applied, therefore, the electrostatic force was not distinguishable from the background.

4.1.2 Van der Waals force

The van der Waals force has also been derived for a cone–sphere tip geometry from first principles by Argento et. al. [73] and the presented form is taken from [72]. Using this geometry the van der Waals force becomes

$$F_{vdW} = -\frac{H}{6} \left\{ \frac{R}{s^2} + \frac{\tan^2\alpha}{s+R_\alpha} - \frac{R_\alpha}{s(s+R_\alpha)} \right\} \tag{4.3}$$

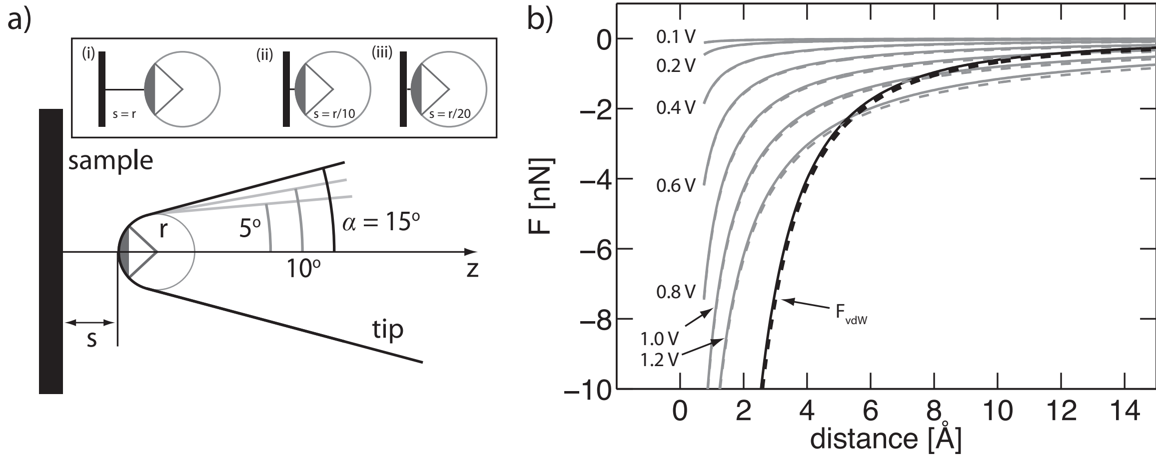

Figure 4.2 a) Tip-sample geometry as cone that is capped with a sphere. The tip sample distance is s, the apex radius is r and the cone angle α. The insets (i)–(iii) shows the geometry for a tip with radius r facing a flat sample at three distances. b) The electrostatic force for different bias voltages (V_t) in compared to the van der Waals force (F_{vdW}). Solid lines represent the results from the complete expressions and dashed lines the simplified versions as described in the text. The geometry is the same as in figure 4.1.

with the Hamaker constant H, the tip radius R, the tip-sample distance s, the cone opening angle α and $R_\alpha = R(1 - \sin(\alpha))$. Again, a simplified form including only the first term describes the situation quite well:

$$F_{vdW} = -\frac{H}{6}\frac{R}{s^2} \tag{4.4}$$

The van der Waals curves in figure 4.2 b) show the forces for both equations – the solid line represents the longer (eq. (4.3)) and the dashed line the simpler version (eq. (4.4)). It is clearly visible that the differences are marginal, especially since the error in the fitting procedure is much larger than the small deviation that is barely visible. The parameters for the plot were: tip-radius $R = 10$ nm, Hamaker constant $H = 4 \cdot 10^{-19}$ J, cone opening angle $\alpha = 5$ deg.

4.1.3 Short range forces

Once the distance between the tip apex atoms and the first layer of sample atoms is on the order of inter-atomic distances (about 5-6 Å), metallic adhesion or binding forces set in. Recent atom probe experiments [74] show that this adhesion force can lead to a contamination

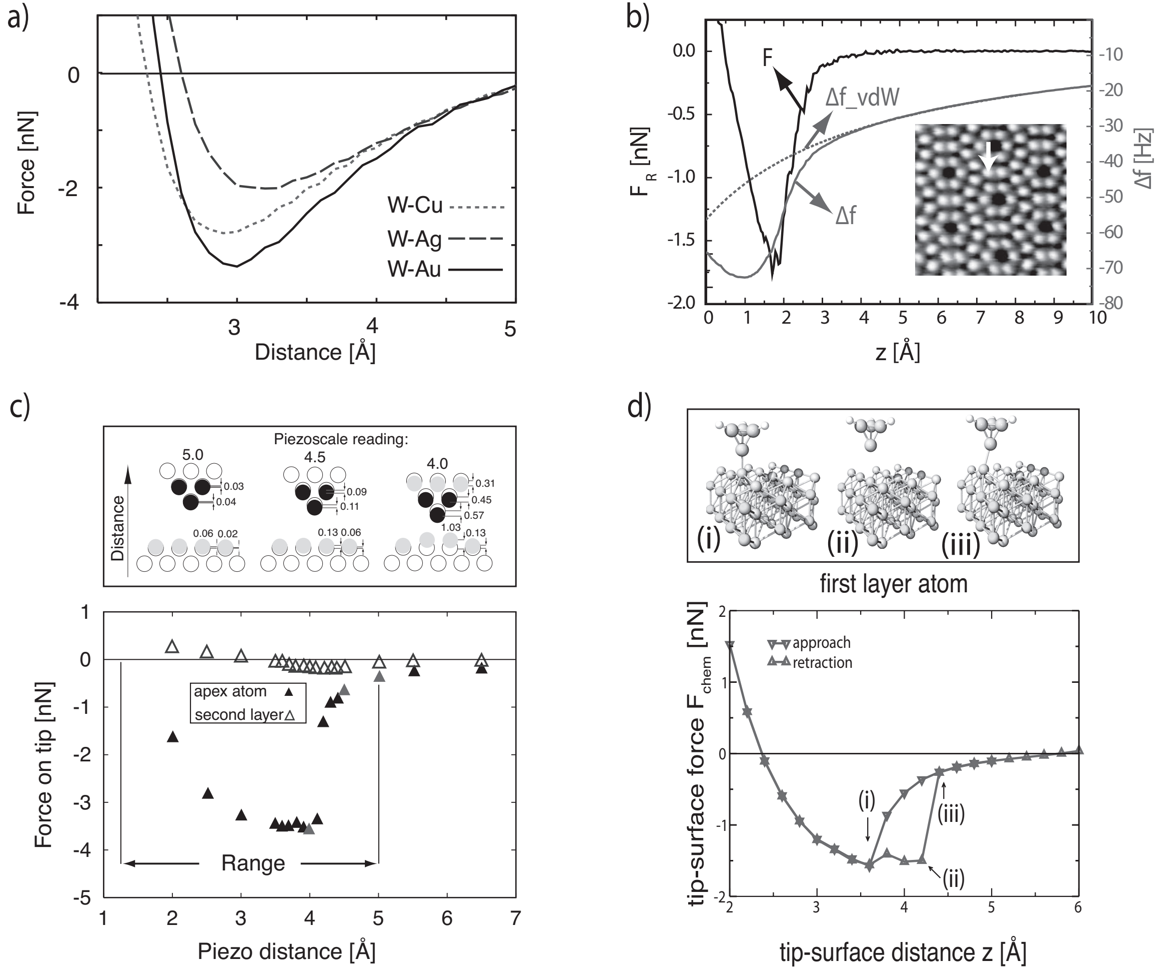

Figure 4.3 a) An example calculation for three dimer configurations. Taken from [40]. b) An experimental result for a Pt/Ir coated Si cantilever approaching a Si(7x7) sample [19]. c) Simulated force versus distance curve for a W tip approaching a Au(111) sample [40]. The drawing shows the amount of relaxation of tip and sample for the three points marked in red in the graph. d) A calculation of a Si tip approaching an Ag(110) sample. The graphic shows characteristic points of the approach-retraction cycle [68].

Copyright: a) and c): Reprinted with permission from Hofer et. al. Phys. Rev. Lett., **87**, 236104 (2001). Copyright 2001 by the American Physical Society. b) Reprinted with permission from Sawada et. al. Applied Physics Letters, **94**, 173117 (2009). Copyright 2009, American Institute of Physics. d) Reprinted with permission from Caciuc et. al. Physical Review B (Condensed Matter and Materials Physics), **77**, 045411 (2008). Copyright 2008 by the American Physical Society.

of a tungsten tip with gold sample atoms during STM measurements.

If the tip-sample gap is simplified as just one tip atom and one sample atom, it is clear that a force distance plot would behave like a derivative of a binding potential of a W-Au dimer. This assumption is a good first approximation of the binding strength and range.

Binding potentials can be described by a number of potentials. The Rydberg and the Morse potential are the most prominent ones. The derivative of the Morse potential would give the force [72]:

$$F_{Morse} = -\nabla U_{Morse} = \frac{2U_0^M}{\lambda_M}\left\{\exp(-2(z - z_0^M)/\lambda_M) - \exp(-(z - z_0^M)/\lambda_M)\right\} \quad (4.5)$$

with the Morse binding energy U_0^M, the Morse scaling length λ_M, the distance z and the Morse equilibrium distance z_0^M. An example of the chemical short range force according to the Morse potential is given in figure 4.1 (green curve). The derivative of the Rydberg potential would give the force [75], [76]:

$$F_{Ryd} = -\nabla U_{Ryd} = -\frac{U_0^R \cdot (z - z_0^R)}{\lambda_R}\exp(-(z - z_0^R)/\lambda_R) \quad (4.6)$$

with the Rydberg binding energy U_0^R, the Rydberg scaling length λ_R, the distance z and the Rydberg equilibrium distance z_0^R. Both functions produce curves that have a very similar shape. A comparison can be seen in figure 4.6. Many curves can be applied to reproduce these binding type curves. Varshni compiled a set of functions that will describe many cases of diatomic binding conditions [77].

Calculated binding energies for different dimer configurations can be found in figure 4.3 a) [40]. All curves have approximately the same range and differ in magnitude slightly. More realistic configurations that have been considered for the results in figure 4.3 c) and d) show a sharp onset of the force due to relaxation – relaxation as defined in the introduction of this chapter is the change in the atomic positions due to the tip-sample force.

Once a more realistic configuration is considered, the situation becomes more complicated since the the tip-sample interaction potential will strongly depend on the tip apex geometry and atoms in the first layers of the opposing structures (tip and sample) will relax. Numeric simulations are necessary to correct the measured force for relaxation effects. As recent publications show [68], [69], it is rather unlikely to obtain a symmetric and smooth approach and retraction curve without hysteresis if an atomically sharp tip is approached

towards a sample, unless the point of contact is of certain symmetry with respect to the bond formation and no snap like shifts occur.

Figures 4.3 b) – d) give a few examples of realistic tip-sample force distance curves. In b) an experimental result is given [19]. The force distance curve was measured with a non-contact atomic force microscope (NC-AFM). A PtIr coated silicon cantilever probed the forces while approaching a Si(7x7) sample in UHV at room temperature. The approached spot on the sample is marked in the inset of figure 4.3 b). The original frequency shift curve is labeled as Δf and the fitted van der Waals contribution as dashed line labeled as Δf_vdW. The latter was subtracted before the frequency data were converted into force data (labeled as F). The resulting force curve has a shorter range than the original data and contains the short range interaction only. In figure 4.3 c) the result of a calculation of the force distance curve for a tungsten STM tip on a gold sample is presented [40]. The tip–sample system was modeled by a tetrahedron of tungsten atoms sitting on top of a stack of Au(111) layers. Five layers of nine atoms have been considered for the tip support. For the sample, the same arrangement has been considered to complete the supercell. A drawing of the setup is given in the upper part of figure 4.3 c). The point of the approach is one of the hollow positions on the Au(111)–fcc(111) surface. The drawing leads to the conclusion that the hcp hollow position is chosen, therefore the tip apex atom would be on top of a second layer sample atom. For the simulation of the short range force a pseudopotential approach has been used – see [40] for details. The distance that is plotted refers to the rigid body separation and therefore corresponds to the piezo extension one records in a real experiment using a fixed sample. As we can see from the graph for the first layer atom, a sharp transition happens at a distance of about 4.1 Å. This is due to the relaxation of the system. The measure of the distance, the piezo reading, is not tracking the real position of the outermost atom but the position it had in the unrelaxed state, which is the situation for a tip far away from the sample where external tip-sample forces can be neglected and the atom-atom distances are equal to the bulk distances. Since the relaxation offset Δz is not taken into account in the piezo reading representation, the onset of the force looks very sharp. If the data is corrected for relaxation, the curve looks smoother as shown below. The calculations were done for the hollow position of Au(111), meaning the tip apex atom approaches the sample on top of a second layer atom. The upper part of figure 4.3 c) shows the amount of relaxation for the tip and sample atoms. In this geometry only the first layer atom is strongly affected by the tip–sample interaction.

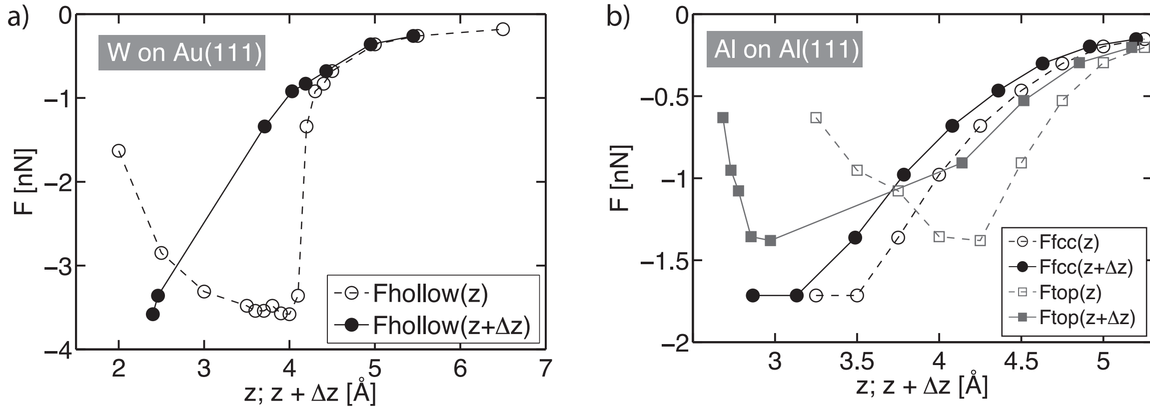

Figure 4.4 Comparison of the unrelaxted distance z and the corrected distance $z + \Delta z$ taking the relaxation into account. a) Result for the data from Hofer et. al. [40] b) Result for the data from Blanco et. al. [41].

Results of a silicon tip on a Ag(110) sample, which are presented in figure 4.3 d), show similar results. The pseudopotential method was used in this case as well [68]. The sample was represented by five layers of a Ag(110)–(3x4) surface. A Si tetrahedron terminated by hydrogen atoms at the base was used to mimic the tip. The maximum attractive force is different due to the different materials but the sharp onset due to relaxations is reflected in the resulting force distance curve as well. Another remarkable aspect is the hysteresis that is due to the differences of binding during the approach and the breaking of the bonds on the retraction (see movies in the supplemental material of [68]). The publication calculated curves for several tip positions. Only the spot on top of a second layer atom gave a force distance curve without hysteresis since in this position the bonding and bond breaking process is stabilized by the surrounding surface layer atoms and no snap like positional shifts occur. Snap like changes during the approach are therefore expected for tips that are terminated by one atom and do not approach an exact symmetry point.

Another calculation by Blanco et. al. [41] contains results for current, force and relaxation for a Al–Al(111) supercell system. This calculation is complementary to the results of Hofer [40] for the W-Au(111) system. For that reason both results are plotted in a figure side by side for a comparison. In fig 4.4 a) the result from Hofer for W-Au(111) is plotted. The dashed line shows the force in dependence of the piezo travel and the solid line replots force points considering the positional shift due to relaxation which represented as Δz.

Figure 4.4 b) is plotted with the same logic. In the case of Al-Al(111) several approach positions have been calculated. Therefore we can compare the tip approaching the fcc hollow position (black circles) and on top of a first layer sample atom (gray squares).

In both cases the sharp onset is stretched and the range is enlarged when comparing the original rigid body separation to the relaxation corrected version. In other words the force curves behave more like a force described by F_{Morse} once the relaxation is taken into account. Looking at the results of Blanco for Al–Al(111), it is obvious that the difference in the position of the force minimum for both tip positions is smaller if the relaxation is considered. Another interesting aspect is the difference in the magnitude of the minimum force for both positions. This shows that different binding processes can lead to different force magnitudes with similar range. This aspect will be discussed in the context of experimental W(111)–Au(111) results later in this thesis.

4.2 Forces in Experimental Data

4.2.1 Long range forces characterization

Experimental Data

Long range forces are not site specific and should therefore be common to all curves. For that reason it is useful to take all curves of a sequence and overlay them in one plot. This allows to distinguish between common features and short range variations. Figure 4.5 illustrates this procedure for several sequences. In parts b) – d) the alignment method is displayed. A common point was defined for all curves of one sequence. In this case $F(TSS_{align}) = -3$ nN was chosen since all curves showed the same behaviour in the distance region $TSS \geq TSS_{align}$. This point is marked by dashed lines in the plots. For each curve TSS_{align} was set to zero and therefore a plot of the curves will look like the ones presented here. Individual force distance curves are plotted in blue and the average for each set of graphs is plotted on top as black curve. In order to get a comparison between sequences, all average plots from graphs b) to d) are plotted in one graph – figure 4.5 a). FIM images of the tips used are given as well together with the tip radii evaluated by the ring counting method (eq. (3.9)). For the shown sequences different tip radii have been used, all with $r_{tip} \leq 15$ nm.

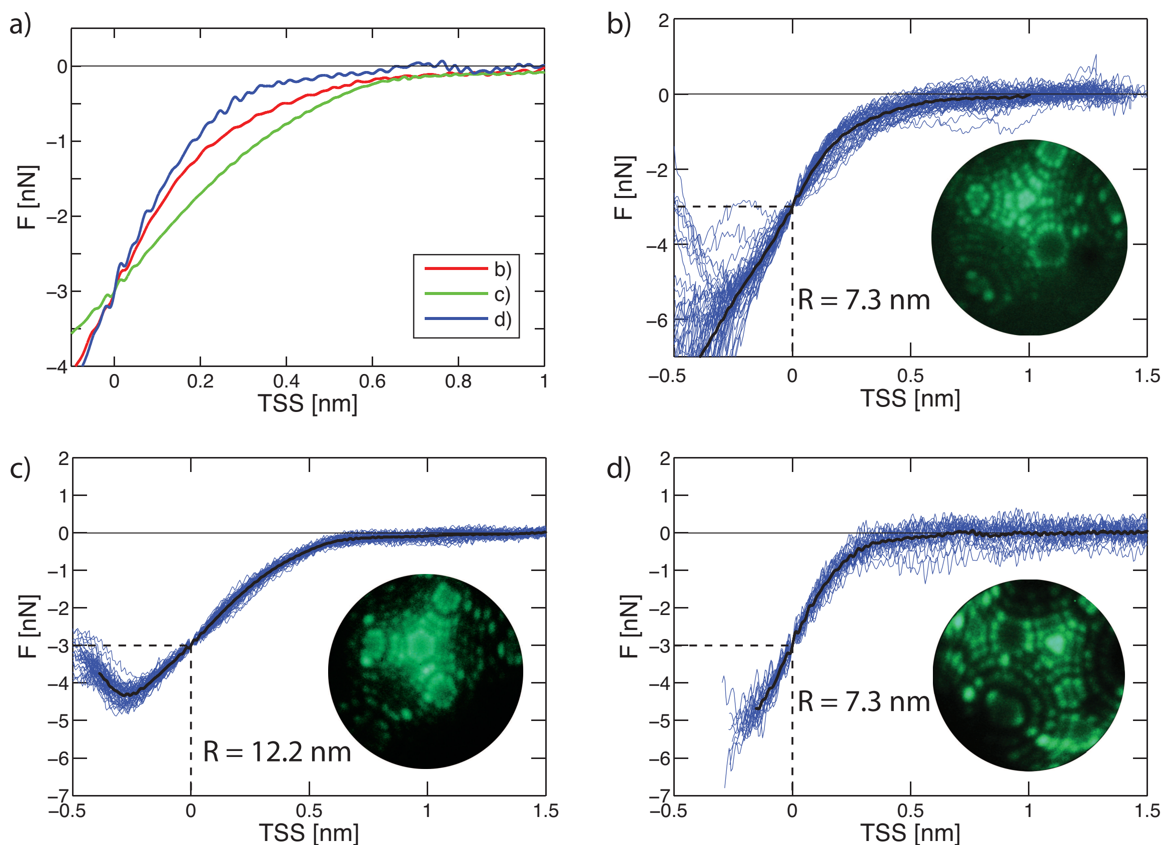

Figure 4.5 Long range characterization: a) Averages of force curves taken from three different sequences taken with four different W(111) tips. Single curves have been aligned to fall on top of each other by taking the value of F = −3 nN as arbitrary reference. The alignment is shown for each sequence in b)–d). The blue curves represent the single runs and the black curve the average of the blue curves. The alignment reference is indicated with dashed lines. For each sequence the FIM image that was taken before the data acquisition and the evaluated radius is given.

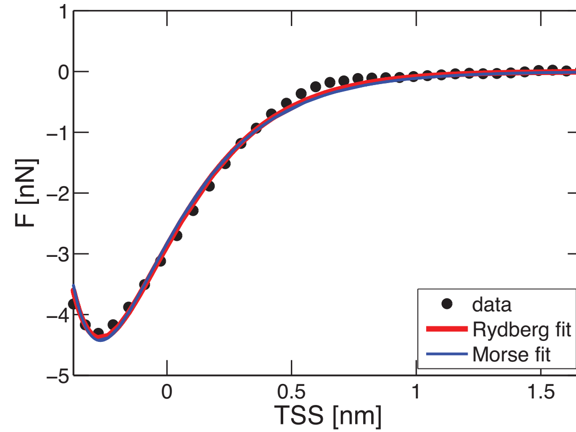

Figure 4.6 Morse and Rydberg fit to average data taken from figure 4.5 c). For details see text.

Discussion

A long range force influence is hardly detectable. The reason why we do not see a large influence of long range forces in contrast to estimations that have been made in chapter 4.1 (see F_{vdW} curve in fig. 4.1) could be explained with the fact that the zero point for the van der Waals interaction is hard to define. As other groups report [72], [78] an offset, which needs to be added to the fitting procedure in order to match the data, can shift the zero point up to 5 Å from the minimum of the measured force curve and lead to a van der Waals force value that is much smaller than a theoretical value that is calculated without the offset. As we can see from figure 4.1 this can lead to a change of several nN in the resulting magnitude of the van der Waals force and therefore a background due to the van der Waals force is not noticeable with the force detection used in this study.

For that reason it is concluded that a long range force subtraction is not necessary in the case of $r_{tip} \leq 15$ nm for the W(111) on Au(111) system and therefore stand in line with the conclusion that has been drawn by Cross [79] and Schirmeisen [80] for tips with a radius of about $r_{tip} = 3$ nm and Sun [81] for tips with $r_{tip} \simeq 15$ nm and the same tip-sample system.

A variation of the bias voltage in the range of $V_t = [-0.1\ \text{V}, +0.1\ \text{V}]$ did not show significant change within our measurement accuracy. Hence, any influence of electrostatic background forces has been neglected as well. A comparison with the curves for the electrostatic force in figure 4.1 shows that this behaviour was expected from the calculations for these voltages.

4.2.2 Short Range Scaling

Experimental Data

Leaving the possible short range atomic structure differences between runs aside, the experimental curves can be characterized with a fit to a force law that has been derived from a Morse or Rydberg potential – see equations (4.5) and (4.6). This is done to evaluate the range or scaling length λ stated in the equations.

Figure 4.6 shows the average data from figure 4.5 c)) and fitted Rydberg and Morse curves. As scaling lengths $\lambda_M = 0.29$ nm and $\lambda_R = 0.22$ nm have been evaluated from the fit. Table 4.1 shows a few examples of scaling lengths for other tip sample systems along with the result from fig. 4.6.

Discussion

It is obvious that the result from figure 4.6 falls into the lower range of scaling length values when comparing it with the reference results in table 4.1.

This is another hint that large long range background force influences are not present in the data. A force curve before background correction tends to have a longer range or scaling length, which is quite obvious from the difference of the total force curve (F_{total}) and the short chemical force (F_{chem}) in figure 4.1. Fitting a Rydberg force curve to both leads to $\lambda_R = 1.90$ nm for the total force curve (F_{total}) and $\lambda_R = 0.36$ nm for the Morse type curve (F_{Morse}). This large difference is due to the slow decay in the tail region of the van der Waals force, which makes it a long range force. This tail region is a hint for a substancial long range contribution that cannot be fitted properly with the fast decaying Rydberg/Morse type curve. Since a slow decaying tail region is not present in the the force curves recorded in the context of this thesis, it is again concluded that substancial contributions from long range forces are not present in the data.

Looking at the data in table 4.1, one can see that the scaling length for different systems is of the same magnitude and does not distinguish between different configurations of atomic species nor between atomic structure influences. One exception is the PtIr–Si(7x7) system. A reason for this discrepancy might be the difference in the chemical nature of the Si sample. In contrast to all other results, which are metal–metal systems, a metal–semiconductor system might reveal a different behaviour due to the different surface states and the different interatomic bonding of the surface atoms [19], [82].

Table 4.1 Experimentally measured scaling lengths for different tip–sample systems. The first result has been evaluated with the fit in figure 4.6.

type	value	tip–sample system
Rydberg	$\lambda_R = 0.22$ nm	W(111)–Au(111)
Rydberg	$\lambda_R = 0.20$ nm	W(111)–Au(111) [80]
Rydberg	$\lambda_R = 0.29$ nm	Al–Au(111) [83]
Rydberg	$\lambda_R = 0.30$ nm	PtIr–MgO(001) [84]
Rydberg	$\lambda_R = 0.05$ nm	PtIr–Si(7x7) [19]

4.3 Tunneling Current and Relaxation

Shortly after the invention of the STM in 1981 [6] a theory for tunneling of plane waves was developed by Tersoff and Hamman [85], [86] based on the Bardeen approach [87]. This model, which is the standard first order theory used to describe STM, assumes a one dimensional geometry and solves the Schrödinger equation for plane waves that tunnel through a barrier of height ϕ. In the result, the tunneling current I_t follows a simple exponential distance dependence:

$$I_t \propto V_t \exp(-2\kappa\, z) \tag{4.7}$$

with the bias voltage V_t between tip and sample, the decay constant κ and the distance between tip and sample z. κ is defined as

$$\kappa = \sqrt{2 m_e \phi}/\hbar \tag{4.8}$$

where m_e the rest mass of the electron, ϕ the apparent barrier height (ABH), and $\hbar$ Planck's constant over $2\,\pi$. Recent reviews of tunneling theory including a more detailed approach considering three dimensional structures, magnetic tunneling junctions and its application to STM can be found in [12], [88].

The apparent barrier height ϕ can be estimated as the average of tip and sample material workfunctions. Therefore we would expect values in the single eV range. For a clean W–Au

tunneling junction a value of $\phi \simeq 3$ to 4 eV has been established by measurements [89], [90]. In an experiment the apparent barrier height can be extracted from the slope in a $\ln(I_t)$ versus z plot, since

$$\phi = \left(\frac{1}{1.025} \frac{d \ln(I_t)}{dz} \right)^2 . \tag{4.9}$$

For current changes $d \ln(I_t)$ in ln(A) and distances dz in Å the equation will give the value of the apparent barrier height in eV.

This model is valid and widely used for tip sample distances that do not correspond to large relaxations. As shown later, it can be used up to distances that correspond to the minimum in the force distance curve to estimate the apparent barrier height. The distance dependence has been discussed since the 1980s [91] in a rigid body model that predicts a collapse of the ABH to zero at a tip sample separation of about 3.2 Å.

Besides a dependence on the tip-sample distance, the ABH is also influenced by the bias voltage as shown in a recent experimental study which is accompanied by a calculation where the ABH dependence on the bias voltage for Au(111), Ag(111) and Cu(111) was investigated [92]. The study confirmed notable changes (> 10 %) of the measured ABH from the zero voltage value for bias voltages of -1 V< $V_t < 3$ V in a range of 2 Å from the tunneling set point $I_{tSP} = 100$ pA, accompanied by an asymmetry with respect to the ABH value at zero volts. Under constant current feedback controlled conditions, a deviation of more than 10 % is notable for $|V_t| > 1$ V. Another publication [93] confirms this trend for Al(100) with a calculation. Since the bias voltages used in this thesis were always lower than 100 mV, voltage induced changes of the ABH can be excluded.

In [92] the dependence of the ABH measurements on the tip structure is mentioned (ref 25 in [92]). The first STM type measurements of the apparent barrier confirmed the relation of the ABH and the tip structure early on and showed that only tips treated *in-situ* by controlled indentation will lead to ABH values of 3-4 eV [89]. Initial ABH values at the beginning of a STM measurement are often smaller than 1.5 eV. Changing the tip from a state characterized by a low ABH into a high ABH configuration is often called tip or contact training and is discussed in section 5.3.

Figure 4.7 presents calculations for realistic structures which include relaxation effects, published by Hofer [40] and Blanco [41]. Looking at the result for the W on Au(111) system (fig. 4.7 a)), one can clearly detect that the current does not follow a simple exponential

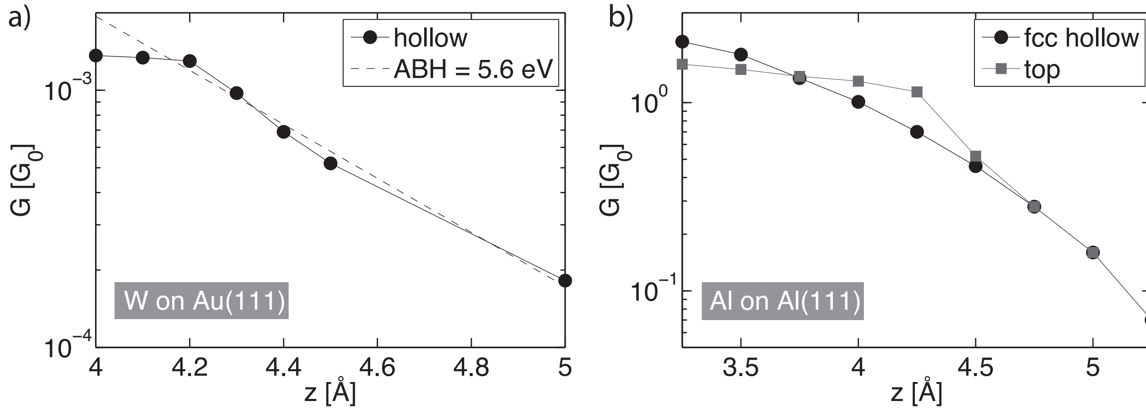

Figure 4.7 Tunneling data from simulations that includes relaxation. a) Data for W on Au(111) [40]. b) Data for Al on Al(111) [41]. Details see text.

distance dependence. A saturation effect is visible at a piezo reading of $z = 4.2$ Å. Compared to the rigid body apparent barrier height of 3.2 eV which is stated in the publication, a fit for $z > 4.2$ Å results in an ABH of 5.6 eV (dashed line in the figure).

In figure 4.7 b) traces for calculated tunneling currents for the Al–Al(111) system are plotted. Results for two positions are illustrated, the tip position on top of a sample atom and on top of the fcc hollow position. Another trace for the hcp hollow position, that is very similar to the fcc hollow position, can be found in the publication by Blanco et. al. [41]. A drawing for the tip approach positions on the fcc(111) surface is given in figure 3.12 b). For distances of $z > 4.5$ Å the two curves fall on top of each other and a fit for that region yields an apparent barrier height of ABH = 3.3 eV. The traces differ for distances $z < 4.5$ Å and the trace for the top position shows a saturation at $z = 4.25$ Å in contrast to the fcc hollow trace.

Comparing the results of Hofer and Blanco, one can see that saturation effects are visible at similar distances. The range of the conductance values is very different, while Hofer's data falls into the $[10^{-4}\, G_0, 10^{-3}\, G_0]$ region, conductance values of about G_0 are reached in the Al–Al(111) model. Blanco attributes the negligence of image potentials in the Bardeen's approach for this difference. Looking at the data presented in this thesis, Hofer's results compare very well with the real W–Au(111) system in magnitude at the point where the ABH changes to a lower value.

Calculations that include both the relaxation due to tip-sample forces and the conductive

properties are rare. Besides the work of Hofer et. al. on the W-Au system [40] and Blanco et. al. for Al-Al [41] other examples treat the force and current for a Cu tip on top of a Co adatom on a Cu surface [94] and for semiconductor surfaces [82] from the theoretical perspective. Common to these four calculation results is the qualitative development of the relaxation in the tip and sample structures. All publications predict a deformation of the structure at a distance that corresponds to the maximum attractive force. In the metal-metal systems the displacements in the tip atom agree on the value of $\Delta z \simeq 1$ Å and for the metal-semiconductor case a displacement of $\Delta z \simeq 0.5$ Å is found.[1]

Published experimental data is also relatively scarce due to the difficulty of combining the current (STM) and force (AFM) measuring techniques. For the W-Au system, two results have been published recently by Schirmeisen [80] and Sun [81]. Another metallic system consisting of a PtIr tip which probes a Ag(001) sample with atomic resolution has been published by König et. al. [96]. These studies show current and force data but do not characterize the contact region clearly.

Rubio-Bollinger combined a tuning fork AFM measurement with a break junction contact measurement to probe the contact hysteresis [97] and also shows the non-contact region. This experiment confirms that clean metal-metal contacts show an exponential increase of the conductivity according to equation (4.7) and reach saturation at $G \simeq G_0$. These findings for the current contact value in a metal-metal SPM contact are supported by STM measurements by the Berndt group [26], [98], [99]. These results have been obtained with tips that were prepared by controlled indentation and showed jump to contact features.

Finally, simultaneous AFM/STM measurements of a metal-semiconductor structure should be mentioned here as well, published by the Morita group [19], [100], [101], [102] and Özer [103]. Comparing the results of these studies, common findings are that the current follows the exponential increase predicted by equation (4.7) with a barrier height of $\phi \simeq 4$ eV. Only the result of Sawada [19] and Sugimoto [102], clearly present current data in the contact region for the PtIr-Si system with a saturation at a conductivity of $G = 3\,G_0$ and the predicted decrease of the current for indentations past the contact point [19].

Comparing these studies to the W(111)-Au(111) system that was probed in this thesis, a clear difference is visible in the current behaviour. For the W-Au case, the ABH is lower than the cited studies and the saturation of the current is not reached. Maximum conductance

[1] A study which investigates the effects of the number of atoms included in the model on the the electronic structure for a non supercell approach of the tip sample system, excluding relaxation, can be found in [95].

values of $10^{-2}\,G_0$ were reached. This could stem from the fact that the tip preparation in this study differed from the cited ones. While all experimental reference results from the literature that show the contact formation were recorded with SPM tips which were modified during the scanning or by controlled indentation in order to obtain high imaging resolution and contacts with a conductivity of about 1 G_0, the goal of this thesis was to use tips that were prepared with field evaporation as described in section 3.4.1 without further modification. In this concept the contact geometry is known, but the electronic properties vary as described in the next chapter and do not resemble the characteristics of a one-atom contact.

CHAPTER 5

Conductive States of the Tunneling Gap

As shown in chapter 4, the contact formation between a STM tip and a sample surface can be characterized by the recorded force and current. The concept of relaxation is expected to play a key role in the characterization of the tunneling gap in the short range regime. In this chapter force and conductivity will be described in order to demonstrate deviations in the behavior of a three-atom tip from the case of ideal one atomic tips that have been calculated in [40], [41].

Basic features of an ideal approach curve for a one atomic contact is given in figure 5.1. A schematic force distance curve is illustrated in gray and the corresponding natural logarithm of the conductivity in black. Black arrows indicate the approach direction. The curve is sectioned into three zones, A, B, C, according to the force signal. Zone A represents the

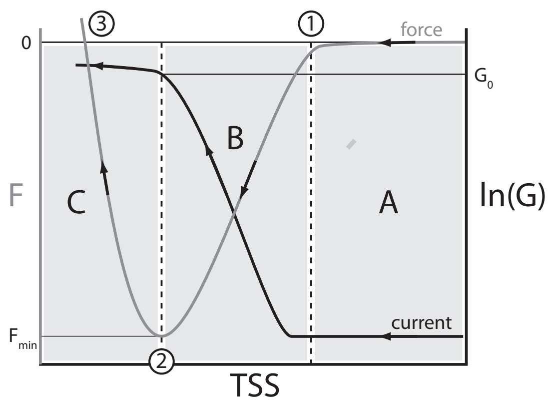

Figure 5.1 Contact formation in a one atomic system. For details see text.

long range regime with a very small interaction between tip and sample. In zone B the attractive short range force sets in and the conductance rises with a constant apparent barrier height and reaches saturation when the force reaches its minimum and a bond is established. The saturation value of the conductance is about 1 G_0. Zone C starts at the force minimum where the overall attractive interaction reaches its maximum. From this point on the conductivity rises approximately in a linear fashion with respect to the distance while repulsive forces start to dominate the total force.

Experimental data confirms this physical picture for STM tips that have been "trained" meaning that these tips have been indented into the sample material and therefore purposely contaminated with the sample material and mechanically formed until the electronic and mechanical properties of the tip behaved according to figure 5.1. Measurements of the current information for different tip-sample systems have been performed in the Berndt group [26], [98], [99] for several tip-sample systems and showed the expected exponential rise of the current up to a contact formation point where the conductivity reached about 1 G_0. Recently Giessibl et. al. [104] measured Cu-Cu and Pt-Pt SPM junctions in a simultaneous AFM/STM configuration with trained tips as well. The results indicate an ideal character of the bonding process with an electrical contact formed at the force minimum with a conductivity of about 1 G_0 matching the current and force traces in figure 5.1.

In the following the results for trained tips are compared to the clean and structurally well characterized W(111) three atom tips that were prepared with the methods presented in chapter 3 for this thesis in order to see if a similar behaviour is observed.

5.1 W(111) Three Atom Tip

The tip-sample force causes relaxations in the tip structure. These are sketched in the upper part of figure 4.3 c) for a one-atom W tip that is approaching a Au(111) sample based on the results of [40]. Situation (1) in figure 5.1 relates to the tip structure in the unrelaxed case which is the case for zero or vanishing small interaction forces. The structure is not changed and the interatomic distances are the same for the tip and sample surface layers as for the bulk. Zero force conditions occur at large distances (zone A). In zone B short range attractive forces set in and dominate the interaction until repulsive forces become larger and a force minimum is reached (point (2) in fig. 5.1). In this force regime the tip and the sample structures are stretched and since the interaction is attractive, atoms of the first layers will be displaced towards the gap (see relaxed structure in figure 4.3 c) for $z = 4.0$ Å). From the

force minimum on, the total force increases due to a domination of repulsive forces. The stretched tip and sample structures react to this decrease in the attractive interaction with a positional shift back towards the initial positions. Depending on the geometry of the tip-sample structure at the approach site, the individual position of each atom is not necessarily the same for point (3) where the total force is zero again as it was at the beginning of the curve. Examples for possible processes at different approach sites have been calculated for Si-Ag(110) and can be found in the form of movies in the supplemental material of [68]. Many different positions on the sample together with rotations around the long axis of the tip as illustrated in section 3.6 should be included in a complete analysis.

5.1.1 The Concept of Early and Late Tunneling

In order to characterize the experimental data a new terminology is introduced. To the best of the author's knowledge the correlation of *force regions* and *apparent barrier height behaviour* has not been discussed in the literature. Therefore the following suggestions are made:

- If the tunneling setpoint is reached in the "early" part of zone B (beginning to middle as defined in figure 5.1) the conductive state will be called "early tunneling state" in the following since the tunneling set point is reached "early" in the approach cycle. The corresponding ABH is at about the expected value of 2–4 eV and indicates a conductive gap.

- If for some reason the tunneling current sets in around the force minimum (end of zone B as defined in figure 5.1), the acquired current data shows a linear rise in a semi-logarithmic plot with an apparent barrier height of $ABH < 1$ eV. This conductive state is called "late" tunneling for obvious reasons.

In order to make the relation to the tunneling condition that is used for imaging, the position at which the tunneling current reaches the feedback set point value during an approach curve is set to zero ($TSS = 0$ nm) in the data representation. In all spectroscopy sequences the current setpoint was set to 50 pA.

In the following, the signatures of "early" and "late" tunneling conditions in experimental force and current versus distance curves will be discussed. Then the influence on the imaging process will be demonstrated and finally a sequence of several force and current

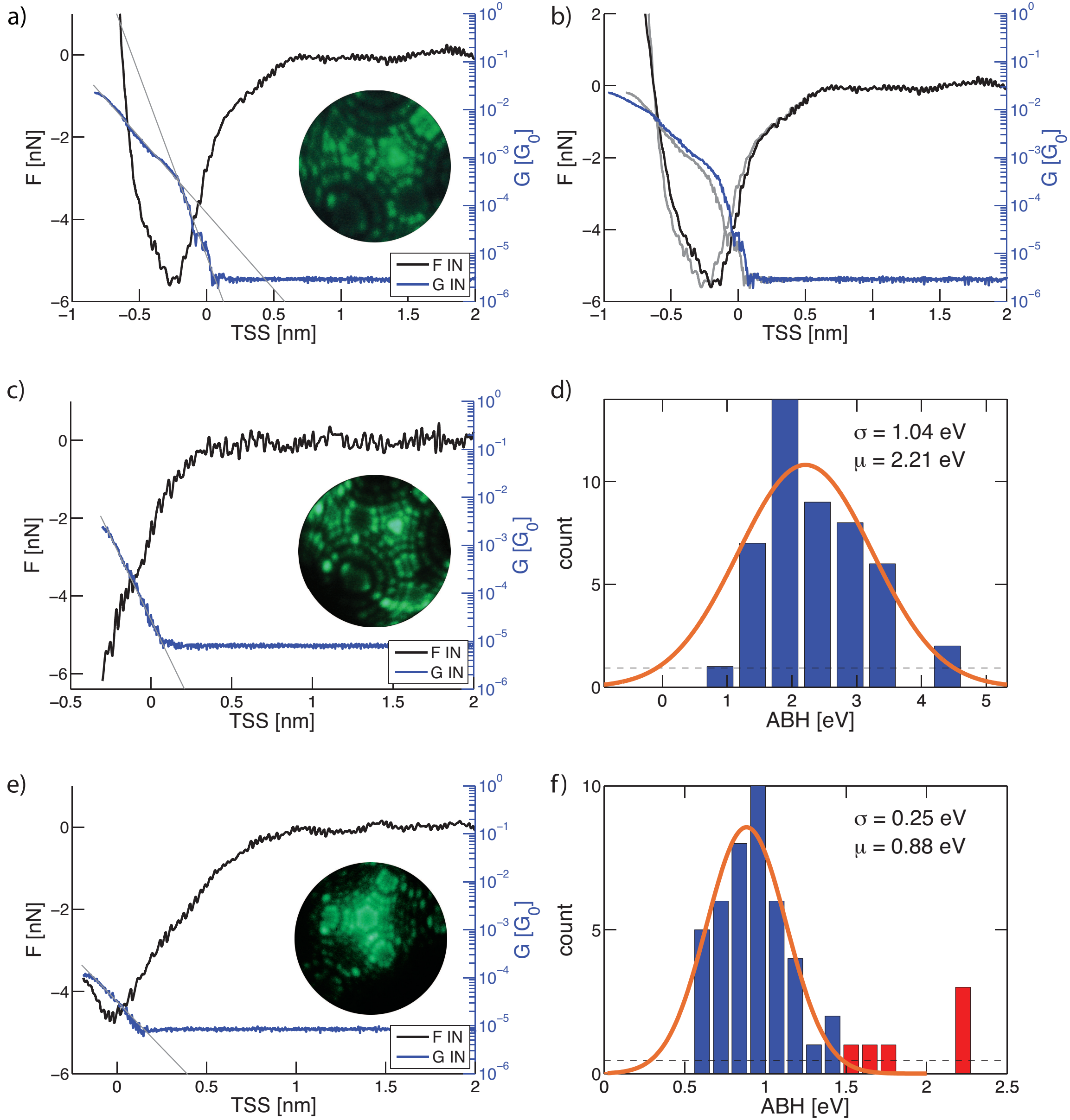

Figure 5.2 a) Force and current versus tip-sample separation curves that show early and late tunneling behaviour in one curve. b) Same data as in a) plotted against TSS and piezo extension. c) Early tunneling: the tunneling setpoint $I_{tSP} = 50$ pA ($G(50$ pA, 50 mV$) = 1.3 \cdot 10^{-5}\, G_0$) is reached at about one half of the force minimum value. d) Histogram of a sequence of "early" tunneling curves. e) Late tunneling: the tunneling setpoint $I_{tSP} = 50$ pA ($G(50$ pA, 20 mV$) = 3.3 \cdot 10^{-5}\, G_0$) is reached around the force minimum. Difference in the magnitude of the force is possibly due to the different tip structure. f) Histogram of a sequence of "late" tunneling curves.

versus distance runs will be analyzed in the context of modifying the conduction properties by controlled soft indentation.

5.1.2 Conductive States of W(111)-Au(111)

Experimental Data

Figure 5.2 shows examples of early and late tunneling data. Figure 5.2 a) illustrates a run which exhibits both early and late tunneling. The conductance rises up to about $1 \cdot 10^{-3}\mathrm{G}_0$ with an apparent barrier height of of $\phi_1 = (3.30 \pm 0.47)$ eV until the force minimum is reached. Then the conductance increase is characterized by an ABH of $\phi_2 = (0.49 \pm 0.10)$ eV. The change of the exponential behaviour is located at the force minimum as described above. The apparent barrier fit is indicated by gray lines. In order to prove that this is not an artefact introduced by the conversion of the z-piezo distance into the tip sample separation, as defined in equation (2.1), the run shown in figure 5.2 a) has been plotted in two ways in figure 5.2 b). In gray the plot against the tip-sample separation is given as reference and in black the force and in blue the current in dependence of the piezo tube extension. One can recognize the change in the data towards a steeper slope for the data that is plotted versus the piezo extension. A fit for the apparent barrier height in both regions has been performed and $\phi_1 = (6.01 \pm 0.59)$ eV for the first region and $\phi_2 = (0.30 \pm 0.01)$ eV has been obtained. As expected ϕ_1 is increased and ϕ_2 is decreased in the z-piezo plotting when compared to the TSS plots.

An example of a run that displays only early tunneling is shown in figure 5.2 c). The apparent barrier height has a value of about (2.48 ± 0.09) eV and the onset of the tunneling occurs at a distance which corresponds to about half of the minimum force. A three atom structure and a tip radius of $r_{tip} = (7.3 \pm 1.2)$ nm is evaluated from the FIM image that was recorded preceding the experimental sequence. Figure 5.2 d) displays a histogram of 46 consecutive runs that indicate the stability of this tunneling condition. The run in c) was the 25th run of the sequence. Assuming normal distributed values, the apparent barrier height of the sequence was evaluated to be $\phi = (2.21 \pm 1.04)$ eV.

In contrast to that the curves in figure 5.2 e) exhibit only late tunneling with an apparent barrier height of $\phi = (0.75 \pm 0.02)$ eV. The FIM image which is shown as inset, was recorded prior to this run and shows a tip which outermost layer corresponds to the second layer displayed in figure 3.10 e) and a tip radius of $r_{tip} = (12.2 \pm 1.2)$ nm. Figure 5.2 f) shows a histogram of 48 consecutive runs that show late tunneling, where the single run in e) was

the first of the sequence. The values that are plotted in red in the histogram were treated as outliers in the Gaussian fit. For the apparent barrier height a value of $\phi = (0.88 \pm 0.25)$ eV has been obtained.

Discussion

There are several possible explanations for this effect. Since published results are often taken with tips that are "trained" by controlled indentation/scanning/spectroscopy cycles in order to obtain high resolution imaging conditions, the atomic tip structure is unknown but stable and conductive. It is very common to assume that the actual tip which is finally used for the experiment is a coating of sample atoms or rearranged tip atom apex structures.

In our case the tip structure is known before the approach and a tip crash can be excluded for the reason that the tunneling current is monitored during the whole sequence and a tip crash would lead to significant current disturbances. But it cannot be excluded that the tip picked up a sample atom or restgas atom during the experimental procedure. Another important aspect is that a tip prepared with FIM might be a less conductive tip. Simulations are done with tetrahedrons of tip atoms [40], [41]. The structures we produce with FIM are flat at the apex and contain three or more atoms in the apex layer, as shown in chapter 3.5. This structural difference might cause differences in the orbital structure and therefore a change in the density of states. If this causes a low density of states around the Fermi energy that are available for tunneling, a low conductivity at low bias would be explained. Differential conductance measurements by recording dI_t/dV versus V spectra would allow to measure the density of states and clarify this question. Additionally, different tip structures should be simulated to shine light on this aspect.

A contamination of the sample can be excluded since "early" and "late" tunneling was reproduced for different sequences on samples which were prepared following standard recipes that routinely produced clean sample surfaces. It seems surprising that tunneling with a constant apparent barrier height is possible at distances that fall into the region where the repulsive interaction dominates the interaction because one would expect the establishing of a contact in this regime. The characteristics of the contact should be a saturation of the current at a value of about 0.1–1 G_0.

If these results are compared to the literature, one notices that the current onset of most published results is at distances that correspond to low attractive force values (beginning of zone B in figure 5.1). An example for a metal PtIr tip on a Si sample can be found in

in figure 2 in [19] where $F < 0.1$ nN at the point ($z = 4$ Å) where $I_t = 1$ nA is reached, about 2 Å from the short range minimum in the force curve. A fit for the apparent barrier height yielded a value of $\phi = (3.55 \pm 0.07)$ eV for that tip sample system. Another example can be found in figure 3 in [80] where a FIM characterized W(111) tip was approached to a Au(111) surface. The current of 2 nA was reached at a force interaction of $F = -0.6$ nN about 6 Å before the minimum of the short range force was reached in the approach cycle. An apparent barrier height of $\phi = (4 \pm 1)$ eV was evaluated for that region.

5.2 Conductive States and STM/AFM Scanning

Stable STM operation can be achieved in early and late tunneling conditions. Two examples for high resolution imaging in these states are displayed in figure 5.3. Late tunneling corresponds to a coupling of the z-piezo and the cantilever motion since the force reaches the maximum of the attractive interaction at a tip-sample distance where the current reaches the set point, which is reflected in the contrast of the different channels. Figure 5.3 a) presents a simultaneous STM/AFM scan of a Au(111) surface that resolves the herringbone reconstruction and the step edges of a screw dislocation clearly. The image size is 150 x 150 nm^2, the bias voltage was set to $V_t = -1.0$ V and the tunneling set point to $I_t = 100$ pA. All three channels, the z-piezo or topography signal, the current signal (It) and the sample cantilever deflection signal are shown. A comparison of all three images indicates that the cantilever deflection resembles the structures seen in the z-piezo data which is caused by the large tip-sample interaction force.

A scan that shows both tunneling modes in one scan is given in figure 5.3 b). It is again a STM/AFM scan of Au(111) with a W tip. Both, the STM tip and the sample were not the same as in part a). As tunneling set point $I_t = 70$ pA has been used and the bias voltage had a value of $V_t = 0.3$ V. The images are separated into a “early” (A) and a “late” (B) part as indicated. The alteration is induced by a tip change due to an interaction with some material on the sample that can be seen on the left side of the dotted line. A look at region A between the black arrows in the z-piezo and the deflection images leads to the conclusion that the step edge is imaged in the same way in both regions. In other words the cantilever deflection followed the z-piezo motion that keeps the current at its set point. A step edge in the z-piezo data is also recorded as step edge in the deflection signal. The current shows a drop at the location of the step edge followed by a small increase. This behavior is due to the delay of the feedback as explained below. It is still interesting to

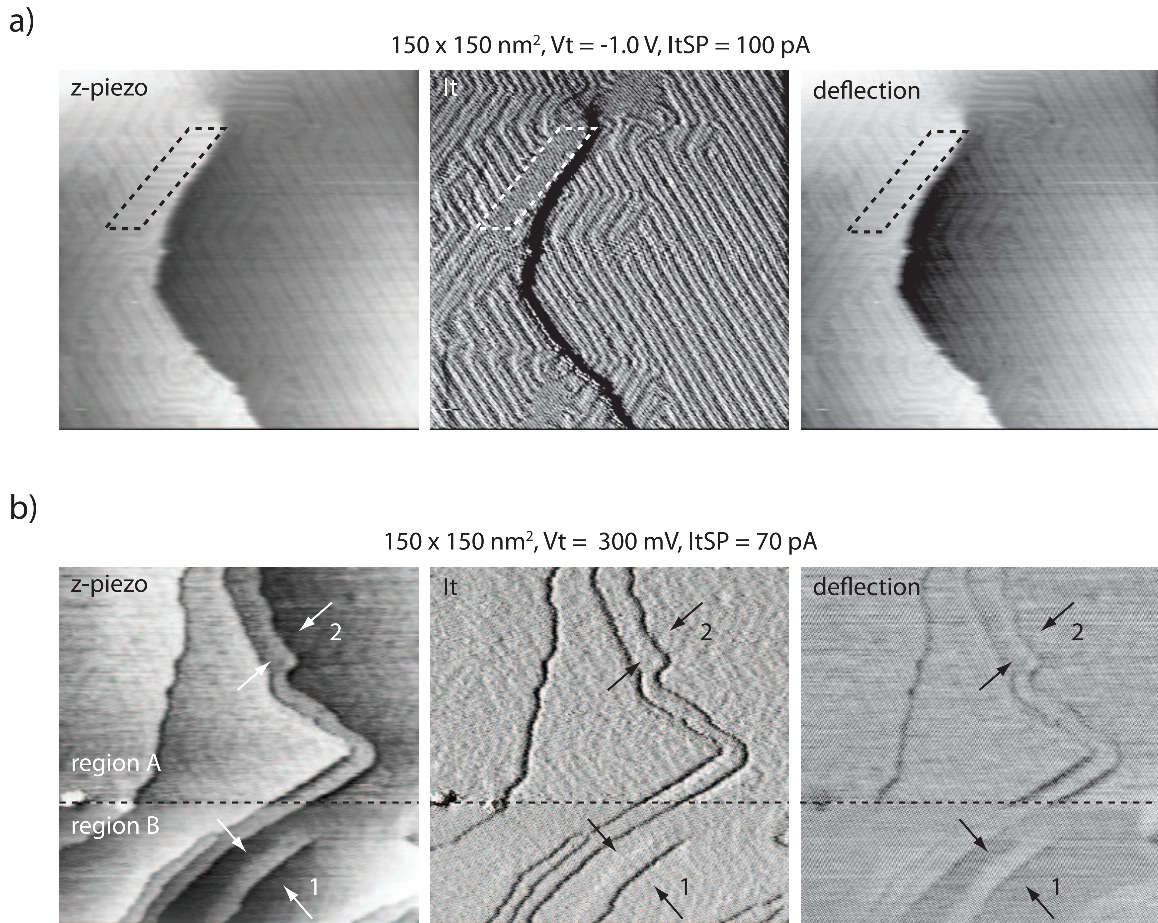

Figure 5.3 a) High resolution image acquired in the late tunneling regime. A characteristic of this tunneling condition is that the topography and the deflection show identical features. b) High resolution image that displays both imaging conditions, the "early" as well as the "late" imaging mode. The top part of the image represents the "early" mode, where the deflection resembles the features of the current channel (It). The arrows at point 1 indicate a good feature for comparison. At the dashed line the tip changes and the imaging mode changes from "early" to "late". Again a feature that displays the mode is marked (point 2).

look at the shape of the step edge features in the current signal. In region B of figure 5.3 b) the current shows only the dip at step edges while region A has a pattern that shows a dip followed by a peak. This is consistent with the step edge pattern in the current data of figure 5.3 a).

The current signal is the error signal of the feedback. If the feedback action including the mechanical extension of the piezo tube was infinitely fast, the current should be a flat line that has the value of the set point. In reality, the electronics, the piezo tube and the cantilever motion have a delay and therefore the current signal shows step edges and the herringbone stripes. In regions where the fast scanning direction (from left to right) is parallel to the herringbone stripes, the current does not show any contrast since the electronic structure is constant along those lines and therefore the feedback does not have to adjust to a sudden change. An example for this phenomenon is marked in figure 5.3 a) with the dashed box in all three images. In that sense the current measures in a differential way, meaning the current signal represents the derivative of the z-piezo signal. A consequence of this differential nature is that the step height between terraces is not measured by the I_t signal. Only the location of step edges, reconstruction lines etc. can be located in the current signal.

If the sample cantilever deflection shows this differential nature as it does in the upper part of figure 5.3 b), the imaging mode can be categorized as early tunneling. A comparison of the parts that are marked with arrows and named region 2, we see that the imaging mode changed. Here, the step edge shape is not resembled in the deflection signal, but the I_t and the deflection signal match.

It should be mentioned that the tips used for the data acquisition that is displayed in figure 5.3 were different, not imaged with FIM and have been exposed to several severe tip changes.

Contact training by controlled approach into the repulsive region has been performed in order to test if a tip can be brought from the late tunneling state into the early tunneling state. The details on this are described in chapter 5.3.

5.3 Contact Training – Switching Conductive States

As mentioned earlier, imaging the structure of the sample can be done in great detail today [13], [14]. In many cases, the tip structure remains unknown. Only indirect methods like picking up a known molecule from the surface and interpreting the image, force and/or

tunneling data gives insight into the chemical nature of the tip [42], [69]. In all of these cases the crystallographic structure of the underlying tip structure remains unknown and could be a crucial influence on the electronic properties of the tip.

Many experimenters use a well established method of tip training by light tip-sample contact, sometimes realized by an accidental "mild" tip crash [42] or approach/retraction cycles [105], and/or adsorption of single atoms from the samples (supporting online material of [14]). Controlled indentation will restructure the tip and possibly coat the tip surface with sample material and yield a useful tip after several preparation cycles. In the case of break junctions the tip training is a well known phenomenon and used to reproduce conductivity traces for statistical analysis [106]. A mechanically stable and electronically conductive tip is needed for high resolution STM. High resolution AFM operation requires a mechanically stable tip with localized force interaction. A tip that is chemically inactive with respect to the sample or which apex structure has no localized interaction cannot give atomic resolution. In some cases like magnetic studies a coating with magnetic sample material is even appreciated in order to have magnetic sensitivity [107], [105]. So far the only *in-situ* imaging of the tip structure with atomic resolution of a tip that is used in a conventional STM is realized by FIM, which is used in this work. An exception to this statement is the unique simultaneous TEM/STM/AFM realized by Kizuka [17], [18], which is dedicated to approach and retraction cycles and gives simultaneous real space atomically resolved structural and conductivity information of atomic wires, this setup misses the usual SPM scanning capabilities in order to realize the TEM measurement. Another approach employing simultaneous REM/STM with scanning capabilities was presented by Naitoh [15], [16]. This setup showed the tip atomic modifications during a STM scan of a Si(7x7) sample and the extraction of Si nano-wires using a tungsten tip.

With the method presented here, the tip apex structure can be imaged before the experiment with atomic resolution. The apex can be modified with field evaporation as shown in figure 3.8. Tips produced in this way can be sharpened up to the point where they have three atoms at the very end. Using these tips for STM scans, high resolution has never been achieved in the context of this work. Stable operation was accomplished, but tips prepared with field evaporation never seemed to be suitable for high resolution. Looking at the structure, one would be surprised if high resolution could be achieved with a three atom tip since this flat triangle integrates over several sample atoms assuming all apex atoms contribute to the tunneling current. An overview of the structural conditions

for a three atom tip facing a Au(111) sample is given in figure 3.12.

Experimental Data

In order to study the effect of the so-called tip training the following experiment was carried out. Figure 5.4 illustrates the experimental sequence. The STM tip was sharpened with field evaporation during FIM operation. The tip radius was estimated to $r_{tip} = (6.1 \pm 1.2)$ nm by the ring counting method (eq. (3.9)) for $n = 5$ steps between the [1 1 1] and the [1 1 0] plane. Once a three atom apex was formed, the tip was approached to a Au(111) cantilever sample and a STM image was taken. After completing four STM images, spectroscopy curves were taken interrupted by STM imaging as indicated in the figure. Both the force (red IN, black OUT) and the current (blue IN, green OUT, in terms of conductivity) were recorded simultaneously. The dashed line indicates the distance at which the tunneling setpoint is reached (I_{tSP} = 50 pA; $G(50\text{pA}, 50\text{mV}) = 50\text{pA} \cdot 13\text{k}\Omega \cdot G_0/50\,\text{mV} = 1.3 \cdot 10^{-5}\, G_0$) and the force minimum for the IN trace. For all curves, as done throughout this thesis, the tip sample separation (TSS) was set to zero at the point where the current reaches the set point. Therefore one can compare the points in the force and current traces at which the tunneling setpoint is reached. The runs are numbered and the first 30 runs after the FIM imaging process are shown. Additionally, the ideal current trace that reaches the conductance of G_0 at the force minimum with a barrier height of $\phi = 4$ eV is indicated by a solid black line.

Inspecting the force part first, one can see that the point of tunneling contact shifted from the minimum in the force curve to values that correspond to a smaller force values when comparing curve one and curve thirty. Earlier in this chapter, curve one would have been described as late tunneling and curve thirty as early tunneling. Another remarkable feature is the reproducibility of the curves. While a formation is seen in curves 1–16, the last nine curves are quite reproducible and do not show large hysteresis. Early curves also indicate that the tip–sample interaction is not as great as it is in later curves, seen in smaller force minima values. The process of tip structure formation seems to have happened on the way towards the sample. Inspecting the hysteresis in curves 12–21, one observes that the retraction cuve remains very stable while the approach curve shows features of structuring. A restructuring of the surface by hole formation can be excluded since a regular check of the surface was performed by STM imaging. Finally, a mechanically stable tip was prepared by controlled indentation using a maximum force of 8.1 nN during the sequence.

The conductive properties of the gap are best described by the development of the ABH.

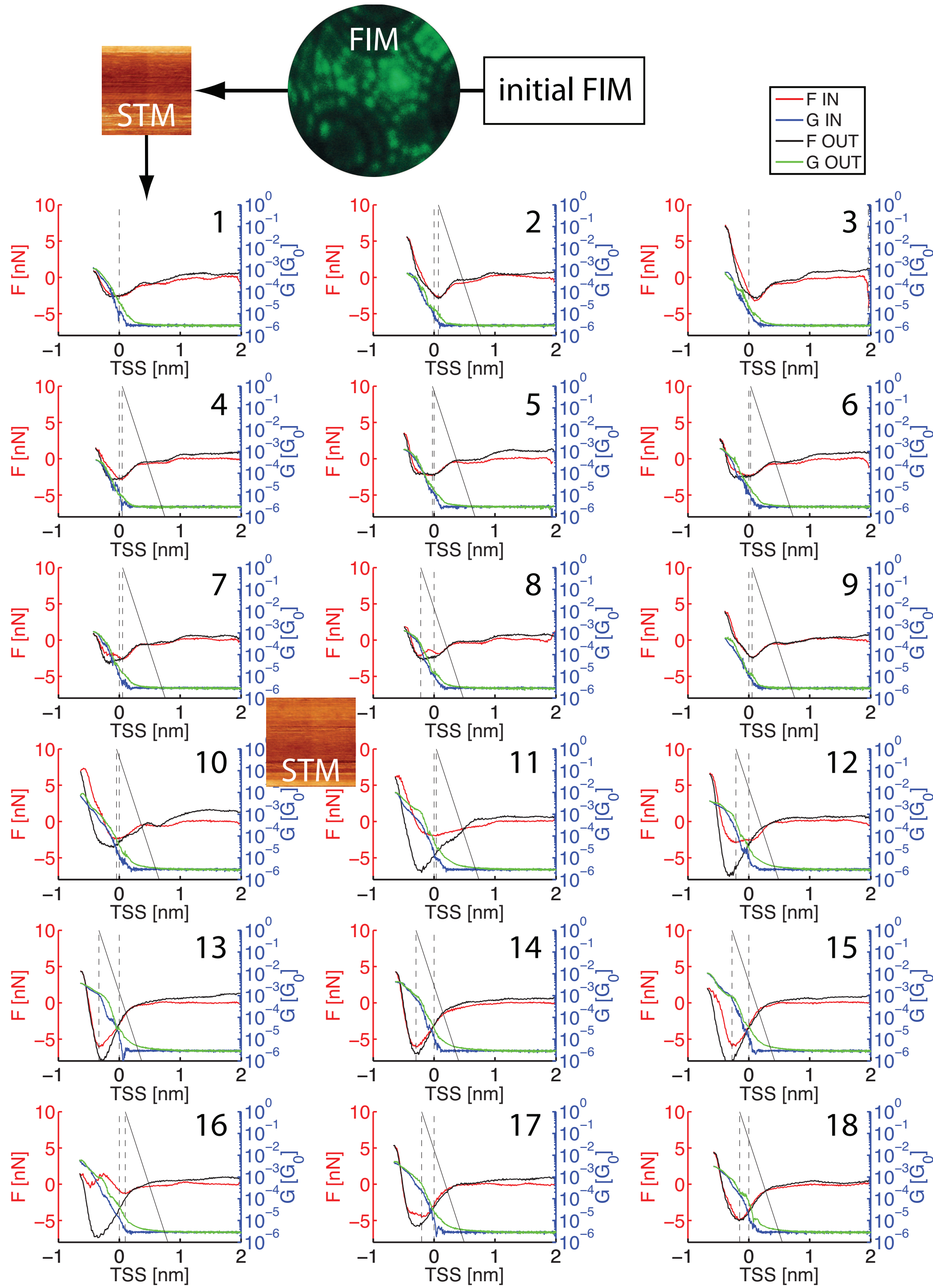

(a) FIM before and runs 1–18. (Continued on the next page)

Figure 5.4 (Continued on the next page)

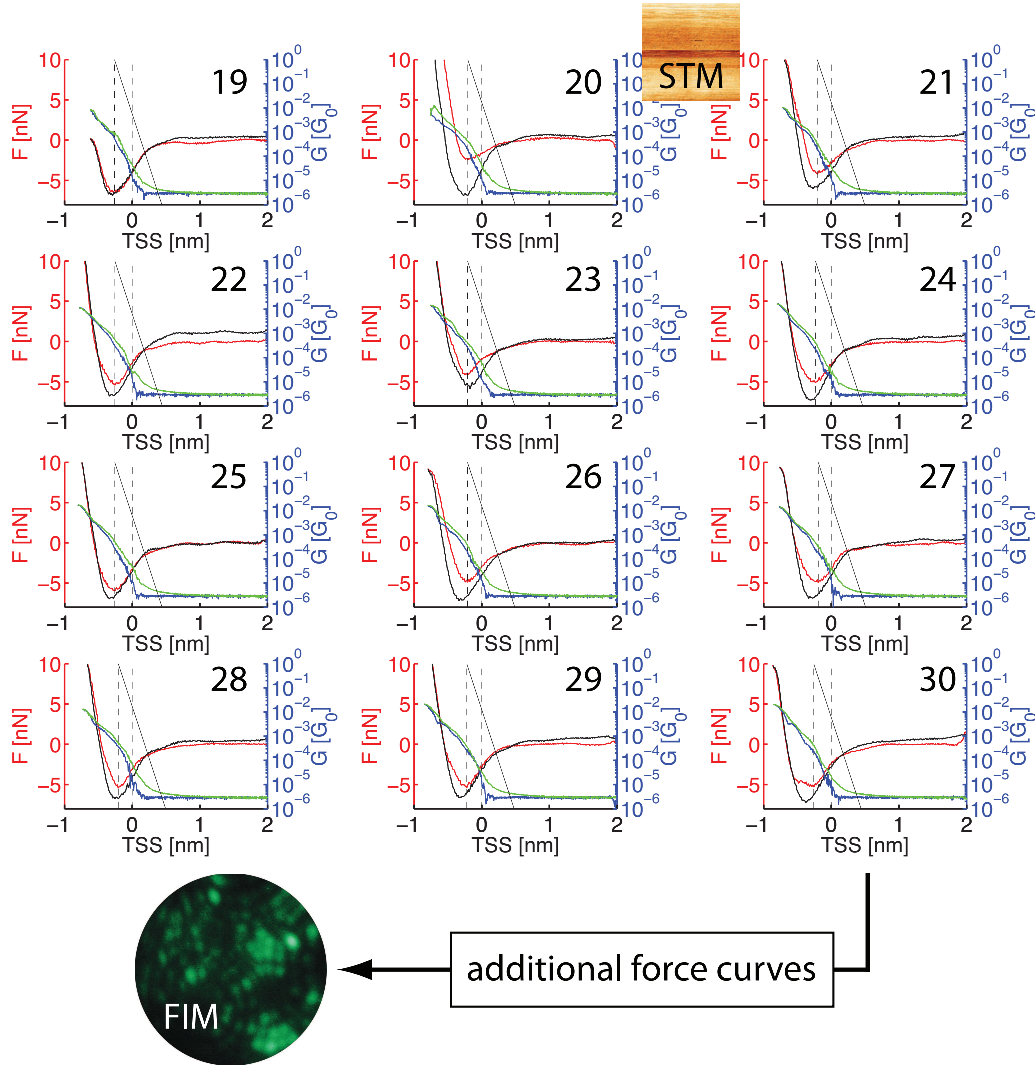

(b) Runs 19–30 and FIM afterwards.

Figure 5.4 Contact training sequence. The development of a good tunneling contact by controlled indentation. After tip imaging with FIM and sample characterization with STM, runs 1–30 show the development of the contact during the sequence. Details see text.

Using the definition of the apparent barrier height before the force minimum, ϕ_1, and after the force minimum, ϕ_2, as suggested in section 5, fits have been performed in order to evaluate both parameters for each run. A plot of the results is given in figure 5.5 a) where ϕ_1 values are plotted in black and ϕ_2 values in gray. One can see that the values of ϕ_1 stabilize towards the end and an average of $\mu_{\phi_1} = 1.95$ eV with $\sigma_{\phi_1} = 0.47$ eV has been evaluated. For the late tunneling part an average of $\mu_{\phi_2} = 0.50$ eV with $\sigma_{\phi_2} = 0.07$ eV was obtained.

The development of the current behaviour is best expressed in the relation of the current onset point to the force minimum. Figure 5.5 b) shows the position of the force minimum on the tip-sample separation axis which is set to zero at the point where the current reaches the setpoint level. In other words, if the current reaches the setpoint at the force minimum, then $TSS_{Fmin} = 0$ nm. This is the case for curves 1–11. From curve 12 on, the current onset moves to lower larger tip-sample separation values with respect to the force minimum, which correspond to an earlier current onset. One can see that the position of the current onset is more stable for runs 12–30 than runs 1–11. The corresponding mean values were $\mu_{1-11} = 0.04$ nm with $\sigma_{1-11} = 0.03$ nm and $\mu_{12-30} = -0.23$ nm with $\sigma_{12-30} = 0.04$ nm. These are indicated as dashed lines in figure 5.5 b).

When the tip structure is examined considering the information that is given in the FIM micrographs in figure 5.4 which were taken before and after the sequence, deviations are visible. The initial structure consisted of three apex atoms, then curves 1–30 were taken together with about 200 additional curves with similar approach parameters. In the final image a six-atom tip is visible. Since the tip was not imaged right after curves 1–30 were completed, the structure of the final FIM image can only be used as an upper boundary estimation of the tip structure modification. Even though repulsive forces of up to 8.1 nN were used, the tip structure only changed in the single atom arrangement and proves the stability of a typical electrochemically etched W(111) STM tip.

Discussion

This sequence shows how the force and current can be brought into stable conditions meaning that the force traces display the expected binding curve shape and with a conductivity that rises at low forces. The image resolution has not been improved in this sequence as the STM images show, further preparation would have been necessary in order to optimize the structure in a way that would improve the spacial resolution and the onset of the cur-

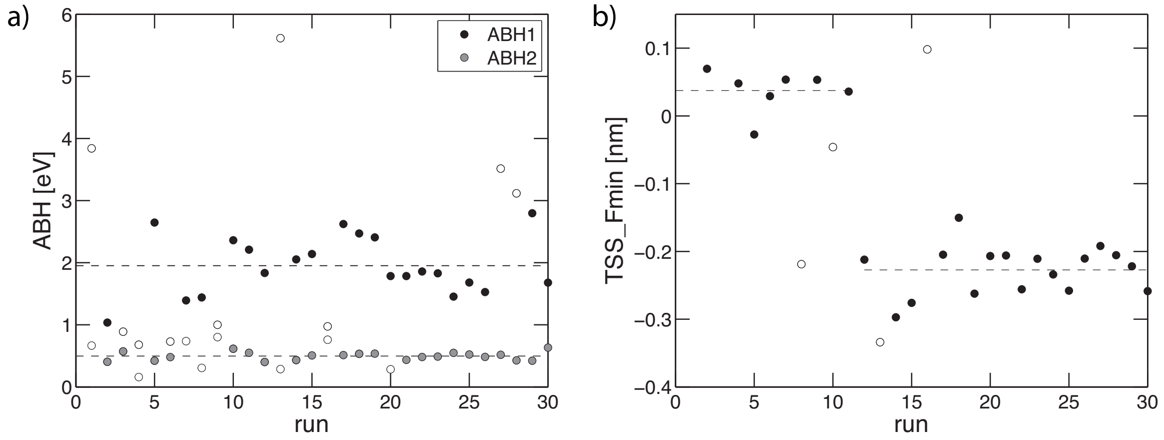

Figure 5.5 a) Development of the ABH for the runs shown in 5.4. b) Development of the current onset point for the same sequence. For both graphs outliers have been identified and plotted as empty circles. The mean for each trace is potted as dashed line.

rent would be pushed to even smaller force values. The final FIM image indicates that a one-atom tip was probably not formed which could explain the low imaging resolution.

As a follow-up to this experiments, one could implement the preparation of one atomic tips via Nitrogen etching during FIM operation as described by Rezeq et. al. [108]. This could answer the question if well defined tips that were not prepared by tip training could actually lead to atomic resolution and stable spectroscopy and if a clean tungsten tip can yield high-resolution images.

CHAPTER 6

Correlation of Force and Conductivity in the Tunneling Regime

Since the early 1990s the correlation of the tip-sample force and the tunneling current has been discussed, motivated by the possibility to gain information about the chemical nature of the tip-sample interaction while in tunneling contact. The local electronic structure can be derived from this correlation, if the experimental contact geometry is known and the theoretical treatment includes the chemical nature of tip and sample. These aspects will be discussed in this chapter.

Chen proposed a model that correlates the force and current and predicts a proportional relation for the short range attractive force region in the form of $I_t \propto F^2$ using Fermi's golden rule in 1991 [109]. Hofer proposed a different approach to this problem in 2003 that predicts a proportional relation with $I_t \propto F$ employing Bardeen's formulation [110]. Based on an experiment by Schirmeisen et. al. published in 2000 [111] both models have been debated by the authors [112], [113]. Lately the group of Jelinek [114], [115] presented new theoretical evidence which shows that both results can be valid. In the presentation it was argued that the $I_t \propto F$ case describes metal-metal contacts and the $I_t \propto F^2$ result metal-semiconductor junctions. New experimental simultaneous force and current data for metal-metal adatom contacts [104] and metal-semiconductor contacts [102] support Jelinek's statement.

In the following the models by Chen and Hofer will be summarized. Then a sequence of data recorded in the context of this thesis will be presented together with a statistical

analysis to underline the validity of the results and finally these results will be compared with other published simultaneous AFM/STM data and discussed in the context of the underlying physics.

6.1 Theoretical Models

6.1.1 Chen's model

Chen's model employs Fermi's golden rule and the assumption that the density of states in the sample ρ_S and in the tip ρ_T are constant around the Fermi energy for small bias voltages V_t. Furthermore constant tunneling matrix elements in the energy range eV_t and the definition $G = I/V_t$ are assumed. In this framework Chen obtained the following expression for the conductivity

$$G = \frac{4\pi^2}{R_K} \rho_S \rho_T |M|^2 \tag{6.1}$$

with the von Klitzing constant $R_K = h/e^2 = 1/(2G_0) \simeq 25.8$ kΩ and the tunneling matrix element M [116]. A relation between the tunneling matrix and the energy state can be found for the states near the Fermi level

$$G = \frac{f\, \rho_S \rho_T}{R_K} |\Delta E|^2 \tag{6.2}$$

with a geometrical tip shape factor f, which can be set to one for a spherical tip [39]. Using the fact that the force can be expressed as the derivative of the energy with respect to the distance $F = -\partial \Delta E / \partial z$ and the the exponential distance dependence of the conductance $G = G(z) \propto \exp(-2\kappa z)$ as defined for the current in equation (4.7), the following relation between force and conductivity can be derived from equation (6.2).

$$F \simeq -\kappa \sqrt{\frac{R_K G(z)}{\rho_S \rho_T}}. \tag{6.3}$$

Or in a form that expresses the proportionality

$$F^2 \propto G(z) \propto I_t(z). \tag{6.4}$$

6.1.2 Hofer's model

Hofer did employ Fermi's golden rule using a Gaussian instead of the delta function in order to include the non-zero temperature effect of state broadening [110]. For the current between the tip and sample states μ and ν he used

$$I\mu\nu = \frac{2\pi}{\hbar\sqrt{\sigma^2\pi}}\,|M_{\mu\nu}|^2 \exp\left(-\frac{(E\nu - E\mu)^2}{\sigma^2}\right) \tag{6.5}$$

with the Gaussian variance σ^2, the energies E, E_μ associated with the states ν, μ and the tunneling matrix element

$$M_{\mu\nu} = \left(\chi_\nu^*, V\psi_\mu\right). \tag{6.6}$$

Using a second order perturbation theory approach, and only considering the change in energy due to tunneling between tip and sample states μ and ν, he states

$$-\Delta E_{\mu\nu} = \frac{|M_{\mu\nu}|^2}{E_\nu - E_\mu}. \tag{6.7}$$

Combining equations (6.5), (6.7) and setting $E_\nu - E_\mu = \sigma$ as justified in [110] one obtains

$$I_{\mu\nu} \simeq \frac{8}{h}\Delta E_{\mu\nu}. \tag{6.8}$$

Using again the relation of force and distance ($F = -\partial\Delta E/\partial z$) and current and distance ($I_t(z) \propto \exp(-2\kappa z)$), the following proportionality between force and current is established

$$F \propto I_t(z) \propto G(z) \tag{6.9}$$

for absolute force values.

6.1.3 Comparative model by Jelinek

Inspired by the controversy around the force and current scaling, Jelinek proposed a model that includes both effects [115]. Starting from Fermi's golden rule that describes the tunneling current

$$I_t \simeq (T^B)^2\,\delta(\epsilon_\alpha - \epsilon_\beta) \tag{6.10}$$

with the tunneling matrix T^B and the energy of the tip state ϵ_α and the sample state ϵ_β. He used the S^2 expansion [117] in order to orthogonalize the tip and sample states and to derive the interaction energy of tip and sample in that case

$$E^{int} \simeq S^2 \Delta\epsilon - S\,T^B + \frac{(T^B)^2}{\Delta\epsilon} \tag{6.11}$$

where S corresponds to the orthogonalization process and $\Delta\epsilon$ expresses the energy change for a transition of the electron from a tip state to a sample state (or reverse depending on the bias settings). In this model S decays fast with increasing tip-sample distance. Therefore the first term is neglected. The magnitude of the second and third term decide if the proportionality is of $F^2 \propto I_t$ or $F \propto I_t$ character. For degenerate states or bands and where the atomic potentials overlap at small tip-sample gaps, S is large and $F^2 \propto I_t$ describes the situation. In cases where the tunneling happens via dangling non-degenerate bonds or large distances, the tail regions of the interatomic potentials, $F \propto I_t$ is a good approximation since S is small in that case.

In general some of the input parameters are not easy to estimate. Distance dependencies of different orbitals and the local atomic structure for each tip-sample distance including relaxations has to be known and implemented in the electronic structure in order to match the experimental situation. The density of states might change and scattering conditions might occur as well [41].

6.2 Experimental study: W(111)-Au(111)

6.2.1 Experimental Data

The presentation of the experimental results is straightforward. If one plots the force and conductance data in a semilog plot versus the distance, the scaling for each can be determined and then compared in order to obtain the scaling factor n in the relation $F^n \propto I_t$. Figure 6.1 shows the result for one sequence. In order to have a better overview, the results have been plotted in two separate graphs so each trace can be followed without graphical interference. In figure 6.1 a) one scaling plot for the current is shown. The linear fit has been performed to the natural logarithm of the data, since the exponential decay can be directly related to the apparent barrier height using equation (4.9). For this run a current decay constant of 2.01 ln(A)/Å has been evaluated which relates to an apparent barrier height of $\phi = 3.8$ eV. The data region that was used for the fit is indicated by dashed

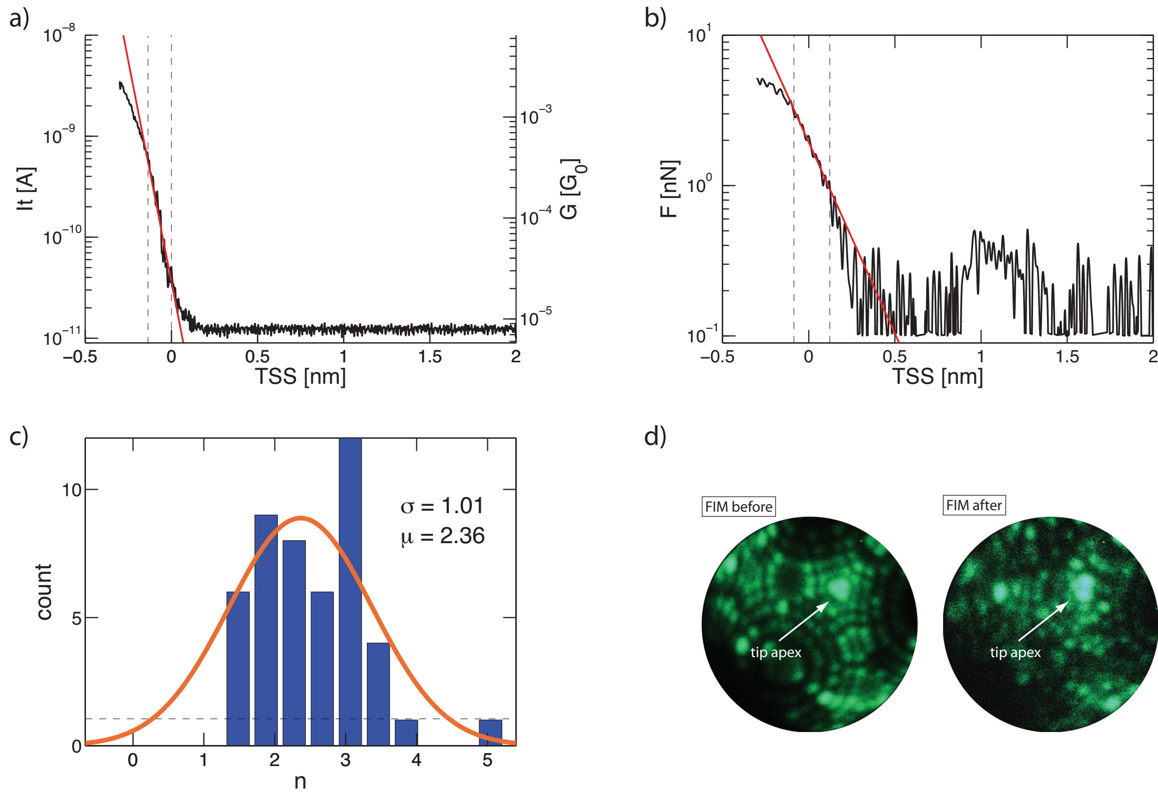

Figure 6.1 a) Scaling graph for the current with respect to the distance. An exponential decay constant of 2.01 ln(A)/nm is found. b) Scaling graph for the force with respect to the distance. An exponential decay constant of 0.59 ln(nN)/nm is evaluated. c) A histogram of the scaling exponent n and a Gaussian fit for 46 consecutive runs all taken with the same tip. d) FIM images of the tip before the sequence of 46 runs and after this experiment and additional runs – details see text.

vertical lines and is determined by a current value in interval around the current set point. The fit for the current decay is very robust.

The same fitting procedure has been applied to absolute values of the force with a resulting decay constant of 0.59 ln(nN)/Å which is illustrated in figure 6.1 b). Only force values larger than $2 \cdot 10^{-1}$ nN have been used for the analysis.

The scaling parameter n can be calculated by assuming an exponential dependence of the chemical short range force on the tip-sample separation in the form of $F \propto \exp(\lambda_F \cdot TSS)$ together with the exponential distance dependence of the tunneling current $I_t \propto \exp(\lambda_{I_t} \cdot TSS)$:

$$F^n \propto I_t \tag{6.12}$$

$$\lambda_F = \frac{\partial \ln F}{\partial TSS} \tag{6.13}$$

$$\lambda_{I_t} = \frac{\partial \ln I_t}{\partial TSS} \tag{6.14}$$

$$n = \frac{\lambda_{I_t}}{\lambda_F}. \tag{6.15}$$

Using the results of the decay constants evaluated from the graphs, a proportionality of $F^n \propto I_t$ with $n = 2.01/0.59 = 3.33$ is supported in this case. The data region that was used for the fit is indicated by dashed vertical lines in the force plot as well. The choice of the fit region is crucial to the quality of the fit, in contrast to the current fit, a careful visual check is necessary for each curve.

In figure 6.1 c) a histogram of the fitting results for a sequence of 46 runs is shown. The resulting mean value from the Gaussian fit for the scaling is $\mu_n = 2.36$ with a standard deviation of $\sigma_n = 1.01$ and the corresponding uncertainty $\delta\mu_n = \sigma_n/\sqrt{N} = 0.15$, where $N = 46$ is the number of runs. The average apparent barrier height has been evaluated in the same way, resulting in $\mu_\phi = 2.61$ eV and $\sigma_\phi = 0.47$ eV.

Figure 6.1 d) displays the tip structure before (left) and after (right) the experiment. The initial structure on the left has been analyzed in chapter 3.5 and the structural details are illustrated in figure 3.10. A tip radius of $r_{tip} = (7.3 \pm 1.2)$ nm is evaluated by the ring counting method. As described earlier the tip has a three atom apex structure. This structure has been used for the 46 runs that have been analyzed and presented here, then additional 860 runs have been performed that showed signatures of minor re-arrangements, which made them impossible to use for this analysis for the fact that the force signal in the

fit region was not smooth enough to justify a linear fit. The right FIM image was taken after all runs have been performed and the apex structure still shows a three atom configuration.

6.2.2 Discussion

As already mentioned, simultaneous force and current data is still rarely published due to the fact that this type of experiment has not become a routine procedure yet because of its difficulty. Nevertheless, some references are available. Schirmeisen [111] evaluated $n \simeq 1$ for currents below 20 nA and $n \simeq 2$ for currents larger than 20 nA for a W-Au tip-sample system. The tip was FIM characterized to be a three atom tip and untrained, meaning it was not modified by indentation cycles prior to the actual contact formation experiment as discussed in section 5.3. A contamination of the tip was also unlikely since it was cleaned by field evaporation before the experiment. Rubio-Bollinger [97] measured a Au-Au system employing a break junction tuning fork AFM type setup using a notched gold wire as tip material. This system gave $n \simeq 1$ where the current was measured at tip-sample separations that correspond to the onset of the short range interaction forces. Recent experiments by Giessibl et. al. [104] did yield $n \simeq 1$ for Cu-Cu and Pt-Pt systems from the onset of the short range forces until contact formation. The contact was formed by a tip contaminated with sample material and an adatom placed on top of the first sample layer which was taken from the sample bulk.

A number of experiments on a Si sample have been performed by the Morita group [102] where a NC-AFM silicon cantilever was approached to a Si(7x7) sample. These measurements gave $n \simeq 2$.

All of the values that were mentioned above for n have been evaluated by rounding the fitting results. The result for the three atom tungsten tip contacting a Au(111) sample has been listed with the reference results in table 6.1 for a better overview.

As Jelinek describes in [115], either scaling can be valid depending on the physical nature of the gap. In the distance regime that corresponds to the onset of the interatomic potentials, a $F \propto I_t$ scaling should be present which is confirmed by the results of Schirmeisen [111] for currents smaller than 20 nA. At distances that correspond to larger chemical short range forces, the nature of the orbitals should influence the scaling relation of current and force. In the case of degeneracy as it is the case in a Si-Si system, the scaling matches the assumption that $n = 2$ in that case. For pure metal-metal one atomic contacts the scaling seems to be in clear support of $n = 1$. The one atomic character in the reference results is attributed

Table 6.1 Experimentally measured force and current scaling values as defined in the text. The first result was evaluated in the context of this thesis.

system	n	published by
W-Au	(2.36 ± 0.15)	this thesis
W-Au	1 and 2	Schirmeisen [111]
Au-Au	1	Rubio-Bollinger [97]
Cu-Cu	1	Giessibl [114]
Pt-Pt	1	Giessibl [114]
Si-Si	2	Sugimoto [102]

to both the tip side and the sample side, since a one atomic tip is contacting an ad atom (Giessibl [104]) or a trained one atomic break junction is used (Rubio-Bollinger [97]).

The result of this thesis matches Schirmeisen's results [111] for smaller tip-sample gaps and opposes the findings for one atomic contacts. Taking the tip and sample structure into account, it might be argued that a three atom tip facing a flat sample could be a contact that shows characteristics of two surfaces instead of a more dimer binding type which is the case in the one atomic contact. Therefore the orbital structure or even a band formation has to be taken into account. In the case of Au, the d-states are completely filled and lie below the Fermi energy, while the s-states are only partially filled and interact. For W d-states are only partially filled and therefore more likely to play a role together with the s-states in the overall process. At close distances all the possible interactions have to be considered, including the hybridization of tip-sample orbitals that could take place when the electron exchange of the binding process occurs. A degenerate band or orbital structure would justify $n = 2$ for tunneling at close distances [114]. In order to justify these assumptions, numeric calculations for the three atomic tip approaching a flat Au(111) sample should be performed.

CHAPTER 7

Conclusion and Future Work

7.1 Conclusion

The scope of this thesis was the controlled contact formation of two nano-objects, namely a STM tip and an atomically flat sample. Force and current signals were employed to characterize the contact formation. In order to reduce the contact size to atomic dimensions, the tip was prepared to be terminated by three atoms and the sample was atomically flat.

Experimental difficulties included the design and implementation of a new coarse approach mechanism to bring the STM tip safely in close proximity to the sample. The tip preparation was reviewed and the design of a novel tip etching container was introduced. Several modifications to the wiring of the measurement system had to be performed in order to reduce the electrical and mechanical noise.

Findings based on the experimental data for the W-Au contact included a study of the contact development during scanning and an induced change of the tip-sample interaction force and electrical conduction by controlled indentation, called tip training. Finally, a sequence of simultaneous force and current versus distance data was related to the $F^n \propto I_t$ scaling theory. The scientific outcomes of this thesis are summarized in the following in more detail, sorted by their appearance in the thesis.

7.1.1 STM tips etched and prepared with FIM

A preparation technique was developed based on past group experience to prepare atomically sharp tips with a tip radius of less than $r_{tip} = 15$ nm as presented in chapter 3. Using the described method, the yield for such tips was increased to 90 % for single crystalline tungsten tips. A limitation to a three-atom tip was posed by the employed field evapora-

tion technique at room temperature since a one-atom tip configuration is not stable under field evaporation conditions at room temperature as further described in chapter 3. The presented results were obtained with a contact geometry that differs from the one atomic case where each of the leads consists of only one atom. These one atomic leads are used in simulations and expected to be the tip structure that produces high-resolution imaging. The consequences for the current and force characteristics are discussed below.

7.1.2 Atomic W(111)-Au(111) contact

Long and Short Range Forces

Since a SPM force measurement is a measurement of the total tip-sample interaction force, all the components of this force have to be analyzed and their contributions identified. An overview of current models and their relation to the tip-sample geometry that was used in this thesis is given in chapter 4. The background or long range force contributions were estimated for a set of fifty curves for three experimental sequences using a different tip for each sequence. The contribution from long range forces were negligible within our measurement precision as shown in figure 4.5 and the related text.

As mentioned before, the results presented in this thesis were recorded measuring a contact that involved a three-atom tip and a flat sample. A detailed analysis of the geometry was presented taking the position of the tip apex on the sample (illustrated in fig. 3.12) and the tilt of the tip against the sample plane into account (shown in fig. 3.14).

The experimental results showed the expected binding type force distance behaviour for all curves. Mechanical stability of the tip-sample structure is thereby proven for the reason that jumps in the signal that are attributed to a sudden restructuring of the gap were absent. The values of the force minimum correspond to the calculated results by Hofer [40] and the range of the force falls into the expected regime as demonstrated by the scaling values in table 4.1.

Conductive States and STM/AFM Scanning

The current did show a deviation from published reference results which show a saturation of the current at the tip-sample distance that corresponds to the force minimum. These reference results were measured with trained tips. Structural differences of the contact might be responsible for that deviation. As discussed at the end of chapter 6, the possible differences in the electronic properties of a three-atom tip compared to a one-atom tip

have to be investigated further to describe the situation more accurately. A more thorough treatment of the presented contact geometry would include the calculation of the local density of states and possible changes in the orbital geometry due to binding. Three-atom tips might form a more surface like electronic structures than a single atom terminating the apex.

Contact Training

Modifying the conductive behaviour of the junction was demonstrated using controlled indentation. As shown in figure 5.4 the onset of the current was shifted to lower force values and the force trace was stabilized in a sense that the IN and OUT traces fell on top of each other, were smooth and had a clear minimum. Besides the earlier onset of the current for later curves of the sequence, the apparent barrier height was changed from low values at the beginning to higher values as well, indicating a higher conductivity as shown in figure 5.5.

Correlation of Force and Current in the Tunneling Regime

Deeper information about the chemical nature of the tip-sample contact can be determined from the correlation of force and current as described in chapter 6. The results obtained for this thesis support a $F^2 \propto I_t$ relation. As described in the discussion of that chapter, the chemical nature of a SPM contact in the contact region – the distance that corresponds to the force minimum – is not completely understood and fine details as electron states that are negligible at regular tunneling distances could play a role in that distance regime. In addition, surface states and hybridization should to be investigated.

7.2 Future Work

7.2.1 Tip preparation

In order to reduce the contact to a one atomic system (one tip-atom and one sample atom), the nitrogen assisted etching technique presented by Rezeq et. al. [108] is now being tested in the FIM system to sharpen the tip apex to only one atom. Cooling to nitrogen temperatures poses an option for more stable experimental conditions. As mentioned in chapter 3, cooling would allow to image adsorbates since the threshold field required for field evaporation of adsorbed atoms is reduced at lower temperatures, and therefore contamination issues by adsorbates could be addressed.

He atoms remaining from the FIM imaging procedure might contaminate the tip apex. As described in [64] the field induced He adsorption takes place on the tungsten tip surface and is needed to create the ionization sites for the field ionization of the imaging gas. The physical and chemical situation of the adsorbed He atoms after the tip voltage is switched off has not been studied in detail yet. One would assume that regular gas kinetics would apply in the absence of the electric field. Since the measurement chamber is pumped to UHV again after the FIM imaging is completed, the probability for He to remain on the tip surface should be low considering the low pressure ($p_{uhv} \leq 10^{-10}$ mbar) and the fact that He is an inert gas. This aspect should be studied in more detail in the future to rule out the possibility of a He monolayer covering the STM-tip after FIM operation.

Some SPM experimenters use voltage pulses while the tip is in proximity to the sample in order to field evaporate contaminations. This method would not be suitable for this type of study since the structure of the FIM characterized tip would change to an unknown structure if atoms were field evaporated from the tip surface.

7.2.2 Atomic contacts

If the preparation of one atomic tips by nitrogen etching succeeds, these could be used to perform tunneling and imaging experiments similar to the ones presented in this thesis. One would expect a better STM imaging resolution using these tips and the force and current characteristics should be closer to the one atomic case presented in figure 5.1; however, stability might be an issue. Another aspect to probe would be if experiments with these tips also show signs of low conductance labeled as late tunneling in section 5.1.1 and structure formation which was described as contact training in section 5.3.

In addition to that, mild indentation could be used to force a contact with saturation features and subsequent FIM micrographs could reveal the structure that is needed to produce these features. An extension to different tip materials like iridium would allow to judge the properties of tungsten as tip material in comparison to iridium. Varying the sample material would permit to extend the material composition further. Micro-fabricated silicon cantilevers are considered as the next step in sample preparation and would extend this study to metal-semiconductor contacts.

Measuring the conduction for a current that passes through a single molecule is possible using the FIM-STM/AFM system. Preliminary experiments were performed by former group members [32]. Using the methods presented in this thesis, a future experiment could

be the measurement of a C_{60} molecule that is confined between the STM tip and the sample. Simultaneous current and force information would reveal chemical information about the binding process. Additionally, the dependence of the conductance on pressure could be probed in this way and possible future applications of this system could be judged. In order to suppress the diffusion of the C_{60} molecule on the surface, the measurement apparatus should be cooled during these experiments.

References

[1] Mierzecki, R. *Dalton's atoms or Dalton's molecules? Journal of Chemical Education*, **58**, 1006 (1981).

[2] Thomson, J. *Cathode Rays. Philosophical Magazine Series 5*, **44**, 293 (1897).

[3] Rutherford, E. *The scattering of α and β particles by matter and the structure of the atom. Philosophical Magazine Series 6*, **21**, 669 (1911).

[4] Einstein, A. *Über einen die Erzeugung und Verwandlung des Lichtes betreffenden heuristischen Gesichtspunkt. Annalen der Physik*, **322**, 132 (1905).

[5] Feynman, R. *There's Plenty of Room at the Bottom. Journal of Microeleciromechanical Systems*, **1**, 60 (1992 (re-print of the original talk held in 1959)).

[6] Binnig, G., Rohrer, H., Gerber, C. and Weibel, E. *Surface Studies by Scanning Tunneling Microscopy. Phys. Rev. Lett.*, **49**, 57 (1982).

[7] Binnig, G., Quate, C. F. and Gerber, C. *Atomic Force Microscope. Phys. Rev. Lett.*, **56**, 930 (1986).

[8] Barth, J. V., Brune, H., Ertl, G. and Behm, R. J. *Scanning tunneling microscopy observations on the reconstructed Au(111) surface: Atomic structure, long-range superstructure, rotational domains, and surface defects. Phys. Rev. B*, **42**, 9307 (1990).

[9] Albers, B. J., Schwendemann, T. C., Baykara, M. Z., Pilet, N., Liebmann, M., Altman, E. I. and Schwarz, U. D. *Three-dimensional imaging of short-range chemical forces with picometre resolution. Nature Nano*, **4**, 307 (2009).

[10] Krause, S., Herzog, G., Stapelfeldt, T., Berbil-Bautista, L., Bode, M., Vedmedenko, E. Y. and Wiesendanger, R. *Magnetization Reversal of Nanoscale Islands: How Size and Shape Affect the Arrhenius Prefactor*. *Phys. Rev. Lett.*, **103**, 127202 (2009).

[11] Repp, J., Meyer, G., Paavilainen, S., Olsson, F. E. and Persson, M. *Imaging Bond Formation Between a Gold Atom and Pentacene on an Insulating Surface*. *Science*, **312**, 1196 (2006).

[12] Hofer, W. A., Foster, A. S. and Shluger, A. L. *Theories of scanning probe microscopes at the atomic scale*. *Rev. Mod. Phys.*, **75**, 1287 (2003).

[13] Repp, J., Meyer, G., Stojković, S. M., Gourdon, A. and Joachim, C. *Molecules on Insulating Films: Scanning-Tunneling Microscopy Imaging of Individual Molecular Orbitals*. *Phys. Rev. Lett.*, **94**, 026803 (2005).

[14] Gross, L., Mohn, F., Moll, N., Liljeroth, P. and Meyer, G. *The Chemical Structure of a Molecule Resolved by Atomic Force Microscopy*. *Science*, **325**, 1110 (2009).

[15] Naitoh, Y., Takayanagi, K., Hirayama, H. and Ohsima, Y. *Simultaneous observation of scanning tunneling microscopy and reflection electron microscopy image of the Si(111)77 surface*. *Surface Science*, **433-435**, 627 (1999).

[16] Naitoh, Y., Takayanagi, K., Oshima, Y. and Hirayama, H. *Simultaneous STM and UHV electron microscope observation of silicon nanowires extracted from Si(111) surface*. *J Electron Microsc (Tokyo)*, **49**, 211 (2000).

[17] Kizuka, T. *Atomic configuration and mechanical and electrical properties of stable gold wires of single-atom width*. *Phys. Rev. B*, **77**, 155401 (2008).

[18] Kizuka, T. and Monna, K. *Atomic configuration, conductance, and tensile force of platinum wires of single-atom width*. *Phys. Rev. B*, **80**, 205406 (2009).

[19] Sawada, D., Sugimoto, Y., ichi Morita, K., Abe, M. and Morita, S. *Simultaneous measurement of force and tunneling current at room temperature*. *Applied Physics Letters*, **94**, 173117 (2009).

[20] Meindl, J. D., Chen, Q. and Davis, J. A. *Limits on Silicon Nanoelectronics for Terascale Integration*. *Science*, **293**, 2044 (2001).

[21] AgraÔt, N., Yeyati, A. L. and van Ruitenbeek, J. M. *Quantum properties of atomic-sized conductors*. *Physics Reports*, **377**, 81 (2003).

[22] Reed, M. A., Zhou, C., Muller, C. J., Burgin, T. P. and Tour, J. M. *Conductance of a Molecular Junction*. *Science*, **278**, 252 (1997).

[23] Tans, S. J., Devoret, M. H., Dai, H., Thess, A., Smalley, R. E., Geerligs, L. J. and Dekker, C. *Individual single-wall carbon nanotubes as quantum wires*. *Nature*, **386**, 474 (1997/04/03/print).

[24] Lu, X., Grobis, M., Khoo, K. H., Louie, S. G. and Crommie, M. F. *Spatially Mapping the Spectral Density of a Single C_{60} Molecule*. *Phys. Rev. Lett.*, **90**, 096802 (2003).

[25] Lu, X., Grobis, M., Khoo, K. H., Louie, S. G. and Crommie, M. F. *Charge transfer and screening in individual C_{60} molecules on metal substrates: A scanning tunneling spectroscopy and theoretical study*. *Phys. Rev. B*, **70**, 115418 (2004).

[26] Limot, L., Kröger, J., Berndt, R., Garcia-Lekue, A. and Hofer, W. A. *Atom Transfer and Single-Adatom Contacts*. *Phys. Rev. Lett.*, **94**, 126102 (2005).

[27] Kuekes, P. J., Stewart, D. R. and Williams, R. S. *The crossbar latch: Logic value storage, restoration, and inversion in crossbar circuits*. *Journal of Applied Physics*, **97**, 034301 (2005).

[28] Strukov, D. B., Snider, G. S., Stewart, D. R. and Williams, R. S. *The missing memristor found*. *Nature*, **453**, 80 (2008/05/01/print).

[29] Tour, J. M. and He, T. *Electronics: The fourth element*. *Nature*, **453**, 42 (2008).

[30] Stadler, A. *Mechanics and Electronics on the Atomic Scale: A Study using Scanning Probe Methods*. Ph.D. thesis, University of Fribourg (1995).

[31] Cross, G. *Mechanics and Electronics on the Atomic Scale: A Study using Scanning Probe Methods*. Ph.D. thesis, McGill University (1999).

[32] Sun, Y. *Study of Interactions at the Atomic Scale*. Ph.D. thesis, McGill University (available online: eScholarship@McGill) (2004).

[33] El Ouali, M. *Nanometre scale indentation of Gold: Effect of very sharp indenters on adhesion, plasticity and transport.* Phd thesis, McGill University (2010).

[34] Oliva, A. I., Anguiano, E., Denisenko, N., Aguilar, M. and Pena, J. L. *Analysis of scanning tunneling microscopy feedback system. Review of Scientific Instruments*, **66**, 3196 (1995).

[35] Anguiano, E., Oliva, A. I., Aguilar, M. and Pena, J. L. *Analysis of scanning tunneling microscopy feedback system: Experimental determination of parameters. Review of Scientific Instruments*, **67**, 2947 (1996).

[36] Anguiano, E., Oliva, A. I. and Aguilar, M. *Optimal conditions for imaging in scanning tunneling microscopy: Experimental. Review of Scientific Instruments*, **69**, 3875 (1998).

[37] Krystek, M. and Anton, M. *A weighted total least-squares algorithm for fitting a straight line. Measurement Science and Technology*, **18**, 3438 (2007).

[38] Grabe, M. *Measurement Uncertainties in Science and Technology.* Springer Berlin Heidelberg (2005).

[39] Chen, C. J. *Introduction to Scanning Tunneling Microscopy.* Oxford University Press, New York (1993).

[40] Hofer, W. A., Fisher, A. J., Wolkow, R. A. and Grütter, P. *Surface Relaxations, Current Enhancements, and Absolute Distances in High Resolution Scanning Tunneling Microscopy. Phys. Rev. Lett.*, **87**, 236104 (2001).

[41] Blanco, J. M., González, C., Jelínek, P., Ortega, J., Flores, F. and Pérez, R. *First-principles simulations of STM images: From tunneling to the contact regime. Phys. Rev. B*, **70**, 085405 (2004).

[42] Ruschmeier, K., Schirmeisen, A. and Hoffmann, R. *Atomic-Scale Force-Vector Fields. Physical Review Letters*, **101**, 156102 (2008).

[43] Gross, L., Mohn, F., Moll, N., Meyer, G., Ebel, R., Abdel-Mageed, W. M. and Jaspars, M. *Organic structure determination using atomic-resolution scanning probe microscopy. Nat Chem*, **advance online publication**, (2010).

[44] Bulou, H. and Goyhenex, C. *Local strain analysis of the herringbone reconstruction of Au(111) through atomistic simulations. Physical Review B*, **65**, 045407 (2002).

[45] Giessibl, F. J. *Atomic resolution on Si(111)-(7 x 7) by noncontact atomic force microscopy with a force sensor based on a quartz tuning fork. Applied Physics Letters*, **76**, 1470 (2000).

[46] Ibe, J. P., P. P. Bey, J., Brandow, S. L., Brizzolara, R. A., Burnham, N. A., DiLella, D. P., Lee, K. P., Marrian, C. R. K. and Colton, R. J. *On the electrochemical etching of tips for scanning tunneling microscopy. Journal of Vacuum Science & Technology A: Vacuum, Surfaces, and Films*, **8**, 3570 (1990).

[47] Melmed, A. J. *The art and science and other aspects of making sharp tips. Fifth international conference on scanning tunneling microscopy/spectroscopy*, **9**, 601 (1991).

[48] Kulawik, M., Nowicki, M., Thielsch, G., Cramer, L., Rust, H.-P., Freund, H.-J., Pearl, T. P. and Weiss, P. S. *A double lamellae dropoff etching procedure for tungsten tips attached to tuning fork atomic force microscopy/scanning tunneling microscopy sensors. Review of Scientific Instruments*, **74**, 1027 (2003).

[49] Yu, Z. Q., Wang, C. M., Du, Y., Thevuthasan, S. and Lyubinetsky, I. *Reproducible tip fabrication and cleaning for UHV STM. Ultramicroscopy*, **108**, 873 (2008).

[50] Lucier, A.-S., Mortensen, H., Sun, Y. and Grutter, P. *Determination of the atomic structure of scanning probe microscopy tungsten tips by field ion microscopy. Physical Review B (Condensed Matter and Materials Physics)*, **72**, 235420 (2005).

[51] Lucier, A.-S. *Preparation and Characterization of Tungsten Tips Suitable for Molecular Electronics Studies.* Master's thesis, McGill University, 3600 Rue University, Montreal, QC, Canada H3A 2T8 (2004).

[52] Schrimeisen, A. *Metallic Adhesion and Tunneling at the Metallic Adhesion and Tunneling at the Atomic Scale.* Ph.D. thesis, McGill University, 3600 Rue University, Montreal, QC, Canada H3A 2T8 (1999).

[53] Ekvall, I., Wahlström, E., Claesson, D., Olin, H. and Olsson, E. *Preparation and characterization of electrochemically etched W tips for STM. Measurement Science and Technology*, **10**, 11 (1999).

[54] Johnson, J. W. and Wu, C. L. *The Anodic Dissolution of Tungsten. Journal of The Electrochemical Society*, **118**, 1909 (1971).

[55] Nakamura, Y., Mera, Y. and Maeda, K. *A reproducible method to fabricate atomically sharp tips for scanning tunneling microscopy. Review of Scientific Instruments*, **70**, 3373 (1999).

[56] Anwei, L., Xiaotang, H., Wenhui, L. and Guijun, J. *An improved control technique for the electrochemical fabrication of scanning tunneling microscopy microtips. Review of Scientific Instruments*, **68**, 3811 (1997).

[57] Muller, A.-D., Muller, F., Hietschold, M., Demming, F., Jersch, J. and Dickmann, K. *Characterization of electrochemically etched tungsten tips for scanning tunneling microscopy. Review of Scientific Instruments*, **70**, 3970 (1999).

[58] Ottaviano, L., Lozzi, L. and Santucci, S. *Scanning Auger microscopy study of W tips for scanning tunneling microscopy. Review of Scientific Instruments*, **74**, 3368 (2003).

[59] Binh, V. T. and Uzan, R. *Tip shape evolution: Capillarity-induced matter transport by surface diffusion. I. Surface Science*, **179**, 540 (1987).

[60] R. H. Fowler, L. N. *Electron Emission in Intense Electric Fields. Proceedings of the Royal Society of London. Series A, Containing Papers of a Mathematical and Physical Character (1905-1934)*, **119**, 173 (1928).

[61] Fink, H. W. *Mono-atomic tips for scanning tunneling microscopy. IBM Journal of Research and Development*, **30**, 460 (1986).

[62] Muller, E. W. *Resolution of the Atomic Structure of a Metal Surface by the Field Ion Microscope. Journal of Applied Physics*, **27**, 474 (1956).

[63] Miller, M. K., Cerezo, A., Hetherington, M. G. and Smith FRS, G. D. W. *Atom Probe Field Ion Microscopy.* Oxford University Press (1996).

[64] Tsong, T. T. *Atom-probe field ion microscopy.* Cambridge University Press (1990).

[65] de Castilho, C. M. C. and Kingham, D. R. *Resolution of the field ion microscope. Journal of Physics D: Applied Physics*, **20**, 116 (1987).

[66] Moore, A. *The structure of atomically smooth spherical surfaces. Journal of Physics and Chemistry of Solids*, **23**, 907 (1962).

[67] Rao, P. V. M., Jensen, C. P. and Silver, R. M. *Enhanced model for scanning tunneling microscope tip geometry measured with field ion microscopy. Journal of Vacuum Science & Technology B: Microelectronics and Nanometer Structures*, **22**, 636 (2004).

[68] Caciuc, V., Holscher, H., Weiner, D., Fuchs, H. and Schirmeisen, A. *Noncontact atomic force microscopy imaging mechanism on Ag(110): Experiment and first-principles theory. Physical Review B (Condensed Matter and Materials Physics)*, **77**, 045411 (2008).

[69] Caciuc, V. and Hölscher, H. *Ab initio simulation of atomic-scale imaging in noncontact atomic force microscopy. Nanotechnology*, **20**, 264006 (2009).

[70] Greiner, M. and Kruse, P. *Recrystallization of tungsten wire for fabrication of sharp and stable nanoprobe and field-emitter tips. Review of Scientific Instruments*, **78**, 026104 (2007).

[71] Hudlet, S., Jean, M. S., Guthmann, C. and Berger, J. *Evaluation of the capacitive force between an atomic force microscopy tip and a metallic surface. Eur. Phys. J. B*, **2**, 5 (1998).

[72] Guggisberg, M., Bammerlin, M., Loppacher, C., Pfeiffer, O., Abdurixit, A., Barwich, V., Bennewitz, R., Baratoff, A., Meyer, E. and Güntherodt, H.-J. *Separation of interactions by noncontact force microscopy. Phys. Rev. B*, **61**, 11151 (2000).

[73] Argento, C. and French, R. H. *Parametric tip model and force–distance relation for Hamaker constant determination from atomic force microscopy. Journal of Applied Physics*, **80**, 6081 (1996).

[74] Fian, A. and Leisch, M. *Study on tip-substrate interactions by STM and APFIM. Ultramicroscopy*, **95**, 189 (2003).

[75] Rose, J. H., Smith, J. R. and Ferrante, J. *Universal features of bonding in metals. Phys. Rev. B*, **28**, 1835 (1983).

[76] Banerjea, A., Smith, J. R. and Ferrante, J. *Universal aspects of adhesion and atomic force microscopy. Journal of Physics: Condensed Matter*, **2**, 8841 (1990).

[77] Varshni, Y. P. *Comparative Study of Potential Energy Functions for Diatomic Molecules. Rev. Mod. Phys.*, **29**, 664 (1957).

[78] Kawai, S., Glatzel, T., Koch, S., Such, B., Baratoff, A. and Meyer, E. *Ultrasensitive detection of lateral atomic-scale interactions on graphite (0001) via bimodal dynamic force measurements. Phys. Rev. B*, **81**, 085420 (2010).

[79] Cross, G., Schirmeisen, A., Stalder, A., Grütter, P., Tschudy, M. and Dürig, U. *Adhesion Interaction between Atomically Defined Tip and Sample. Phys. Rev. Lett.*, **80**, 4685 (1998).

[80] Schirmeisen, A., Cross, G., Stalder, A., Grtter, P. and Drig, U. *Metallic adhesion forces and tunneling between atomically defined tip and sample. Applied Surface Science*, **157**, 274 (2000).

[81] Sun, Y., Mortensen, H., Schar, S., Lucier, A.-S., Miyahara, Y., Grutter, P. and Hofer, W. *From tunneling to point contact: Correlation between forces and current. Physical Review B (Condensed Matter and Materials Physics)*, **71**, 193407 (2005).

[82] Jelínek, P., Švec, M., Pou, P., Perez, R. and Cháb, V. *Tip-Induced Reduction of the Resonant Tunneling Current on Semiconductor Surfaces. Phys. Rev. Lett.*, **101**, 176101 (2008).

[83] Gotsmann, B. and Fuchs, H. *Dynamic Force Spectroscopy of Conservative and Dissipative Forces in an Al-Au(111) Tip-Sample System. Phys. Rev. Lett.*, **86**, 2597 (2001).

[84] Heyde, M., Sterrer, M., Rust, H.-P. and Freund, H.-J. *Frequency modulated atomic force microscopy on MgO(001) thin films: interpretation of atomic image resolution and distance dependence of tipÄìsample interaction. Nanotechnology*, **17**, S101 (2006).

[85] Tersoff, J. and Hamann, D. R. *Theory and Application for the Scanning Tunneling Microscope. Phys. Rev. Lett.*, **50**, 1998 (1983).

[86] Tersoff, J. and Hamann, D. R. *Theory of the scanning tunneling microscope. Phys. Rev. B*, **31**, 805 (1985).

[87] Bardeen, J. *Tunnelling from a Many-Particle Point of View. Phys. Rev. Lett.*, **6**, 57 (1961).

[88] Blanco, J. M., Flores, F. and PÈrez, R. *STM-theory: Image potential, chemistry and surface relaxation. Progress in Surface Science*, **81**, 403 (2006).

[89] Binnig, G., Rohrer, H., Gerber, C. and Weibel, E. *Tunneling through a controllable vacuum gap. Applied Physics Letters*, **40**, 178 (1982).

[90] Olesen, L., Brandbyge, M., Sørensen, M. R., Jacobsen, K. W., Lægsgaard, E., Stensgaard, I. and Besenbacher, F. *Apparent Barrier Height in Scanning Tunneling Microscopy Revisited. Phys. Rev. Lett.*, **76**, 1485 (1996).

[91] Lang, N. D. *Apparent barrier height in scanning tunneling microscopy. Phys. Rev. B*, **37**, 10395 (1988).

[92] Becker, M. and Berndt, R. *Influence of band structure on the apparent barrier height in scanning tunneling microscopy. Phys. Rev. B*, **81**, 035426 (2010).

[93] Totsuka, H., Gohda, Y., Furuya, S. and Watanabe, S. *Theoretical analysis of the bias-voltage dependence of the apparent barrier height. Phys. Rev. B*, **70**, 155405 (2004).

[94] Huang, R. Z., Stepanyuk, V. S., Klavsyuk, A. L., Hergert, W., Bruno, P. and Kirschner, J. *Atomic relaxations and magnetic states in a single-atom tunneling junction. Phys. Rev. B*, **73**, 153404 (2006).

[95] Saha, K. K., Henk, J., Ernst, A. and Bruno, P. *Multiple-scattering theoretical approach to scanning tunneling microscopy. Phys. Rev. B*, **77**, 085427 (2008).

[96] König, T., Simon, G. H., Rust, H.-P. and Heyde, M. *Atomic resolution on a metal single crystal with dynamic force microscopy. Applied Physics Letters*, **95**, 083116 (2009).

[97] Rubio-Bollinger, G., Joyez, P. and Agraït, N. *Metallic Adhesion in Atomic-Size Junctions. Phys. Rev. Lett.*, **93**, 116803 (2004).

[98] Neel, N., Kröger, J., Limot, L. and Berndt, R. *Conductance of single atoms and molecules studied with a scanning tunnelling microscope*. *Nanotechnology*, **18**, 044027 (2007).

[99] Néel, N., Kröger, J. and Berndt, R. *Quantized Conductance of a Single Magnetic Atom*. *Phys. Rev. Lett.*, **102**, 086805 (2009).

[100] Sugimoto, Y., Namikawa, T., Miki, K., Abe, M. and Morita, S. *Vertical and lateral force mapping on the* $Si(111)-(7\times 7)$ *surface by dynamic force microscopy*. *Phys. Rev. B*, **77**, 195424 (2008).

[101] Sugimoto, Y., Nakajima, Y., Sawada, D., Morita, K.-i., Abe, M. and Morita, S. *Simultaneous AFM and STM measurements on the* $Si(111)-(7\times 7)$ *surface*. *Phys. Rev. B*, **81**, 245322 (2010).

[102] Sugimoto, Y., Yi, I., ichi Morita, K., Abe, M. and Morita, S. *Simultaneous force and current mapping of the Si(111)-(7 x 7) surface by dynamic force microscopy*. *Applied Physics Letters*, **96**, 263114 (2010).

[103] Özer, H. Ö., O'Brien, S. J. and Pethica, J. B. *Local force gradients on Si(111) during simultaneous scanning tunneling/atomic force microscopy*. *Applied Physics Letters*, **90**, 133110 (2007).

[104] Giessibl, F. J. *Simultaneous force and current measurements on single adatoms*. *NC-AFM 2010 proceedings*.

[105] Berbil-Bautista, L., Krause, S., Bode, M. and Wiesendanger, R. *Spin-polarized scanning tunneling microscopy and spectroscopy of ferromagnetic Dy(0001)/W(110) films*. *Phys. Rev. B*, **76**, 064411 (2007).

[106] Trouwborst, M. L., Huisman, E. H., Bakker, F. L., van der Molen, S. J. and van Wees, B. J. *Single Atom Adhesion in Optimized Gold Nanojunctions*. *Phys. Rev. Lett.*, **100**, 175502 (2008).

[107] Wiesendanger, R. *Spin mapping at the nanoscale and atomic scale*. *Rev. Mod. Phys.*, **81**, 1495 (2009).

[108] Rezeq, M., Pitters, J. and Wolkow, R. *Tungsten nanotip fabrication by spatially controlled field-assisted reaction with nitrogen. The Journal of Chemical Physics*, **124**, 204716 (2006).

[109] Chen, C. J. *Attractive interatomic force as a tunnelling phenomenon. Journal of Physics: Condensed Matter*, **3**, 1227 (1991).

[110] Hofer, W. A. and Fisher, A. J. *Signature of a Chemical Bond in the Conductance between Two Metal Surfaces. Phys. Rev. Lett.*, **91**, 036803 (2003).

[111] Schirmeisen, A., Cross, G., Stalder, A., Grutter, P. and Durig, U. *Metallic adhesion and tunnelling at the atomic scale. New Journal of Physics*, **2**, 29 (2000).

[112] Chen, C. J. *Comment on "Signature of a Chemical Bond in the Conductance between Two Metal Surfaces". Phys. Rev. Lett.*, **96**, 069701 (2006).

[113] Hofer, W. A. and Fisher, A. J. *Hofer and Fisher Reply:. Phys. Rev. Lett.*, **96**, 069702 (2006).

[114] Jelinek, P. *Theoretical understanding of the current and the chemical force in atomic scale contacts. NC-AFM 2010 proceedings* (2010).

[115] Jelinek, P. and Flores, F. *Relation between chemical force and tunneling current in point contacts: a simple model. ArXiv e-prints* (2010).

[116] Chen, C. J. *A universal relation in NC-AFM, STM, and atom manipulation. Nanotechnology*, **16**, S27 (2005).

[117] Goldberg, E. C., Martín-Rodero, A., Monreal, R. and Flores, F. *Molecular orbital theory for chemisorption and physisorption: The case of He on metals. Phys. Rev. B*, **39**, 5684 (1989).

[118] Russell, A. M. *Electron Trajectories in a Field Emission Microscope. Journal of Applied Physics*, **33**, 970 (1962).

[119] Patil, S., Kulkarni, A. V. and Dharmadhikari, C. V. *Study of the electrostatic force between a conducting tip in proximity with a metallic surface: Theory and experiment. Journal of Applied Physics*, **88**, 6940 (2000).

[120] http://laacg1.lanl.gov/laacg/services/download_sf.phtml.

[121] Jian, H., Lanping, W., Yue, C. and Guowen, W. *Magnetically controlled coarse approach device for STM. Measurement Science and Technology*, **1**, 1116 (1990).

[122] MacLeod, J. M., Moffat, A., Miwa, J. A., Mark, A. G., Mullins, G. K., Dumont, R. H. J., Constant, G. E. and McLean, A. B. *Two linear beetle-type scanning tunneling microscopes. Review of Scientific Instruments*, **74**, 2429 (2003).

[123] Silveira, W. R. and Marohn, J. A. *A vertical inertial coarse approach for variable temperature scanned probe microscopy. Review of Scientific Instruments*, **74**, 267 (2003).

[124] Mugele, F., Kloos, C., Leiderer, P. and Möller, R. *A simple, ultrahigh vacuum compatible scanning tunneling microscope for use at variable temperatures. Review of Scientific Instruments*, **67**, 2557 (1996).

APPENDIX A

Tip Reconstruction

As mentioned earlier in chapter 3 the reconstruction of a tip imaged with FIM is based on the assumption that the shape of the tip appex is spherical. Therefore we need to construct a cube of tip atoms that can be cut by a sphere. The following describes how to construct cubes of bcc 111 (for tungsten single crystalline tips) and bcc 110 (for tungsten polycrystalline tips).

A.1 Construction of a bcc 111 oriented cube

Figure A.1 a) shows the usual representation of a bcc 111 cube. Additionally the layers that are 111 oriented are shown for a full 111 translation. Atoms lying outside the cube are colored in light gray. The 111 direction is indicated by the red vector. There are six 111 layers when we go from (0,0,0) to (1,1,1) therefore the plane spacing is

$$a_W * |(1,1,1)|/6 = a_W * \sqrt{3}/6 \simeq 0.092 \text{ nm}. \tag{A.1}$$

As seen from the figure the stacking is ABCA (colored red, green, blue, red). In order to construct a bcc 111 oriented cube we need to find the base vectors i and j that describe the plane atoms, as well as the vector k that introduces the shift between planes. The author chose the following

$$\overrightarrow{i} = (0,-1,1) \tag{A.2}$$
$$\overrightarrow{j} = (-1,0,1) \tag{A.3}$$
$$\overrightarrow{k} = (0.5,-0.5,0.5). \tag{A.4}$$

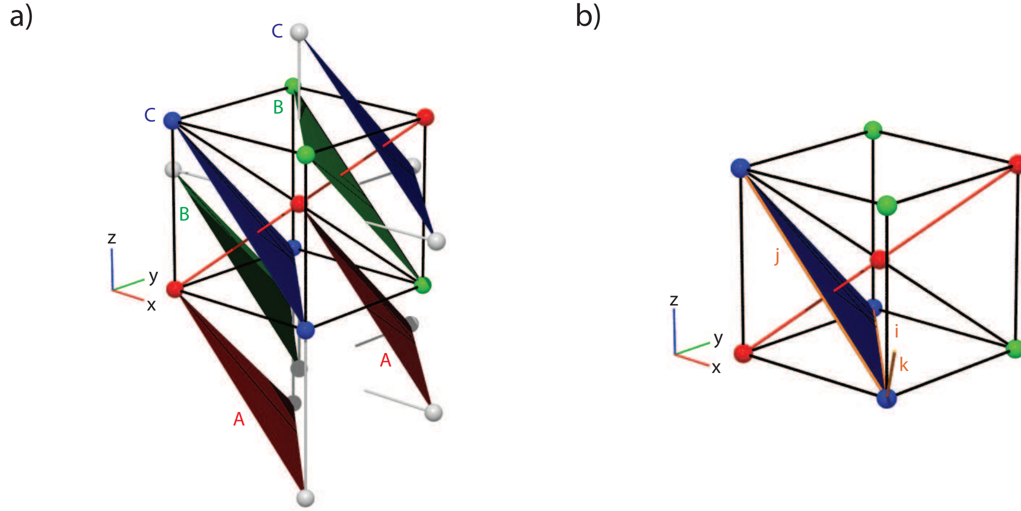

Figure A.1 a) Visualization of the bcc 111 planes. b) Illustration of the ijk vectors for the cube construction.

Figure A.1 b) shows these vectors in orange.

A.2 Construction of a bcc 110 oriented cube

The procedure is analogous to the one showed before. The plane distance in the bcc 110 direction is

$$a_W * |(1,1,0)|/2 = a_W * \sqrt{2}/2 \simeq 0.23 \text{ nm} \tag{A.5}$$

And as seen from figure A.2 a) the stacking is ABA (colored red, green, red). The base vectors

$$\overrightarrow{i} = (1,-1,0) \tag{A.6}$$

$$\overrightarrow{j} = (0.5,-0.5,0,5) \tag{A.7}$$

$$\overrightarrow{k} = (1,0,0) \tag{A.8}$$

are shown in orange and the 110 direction is shown in red.

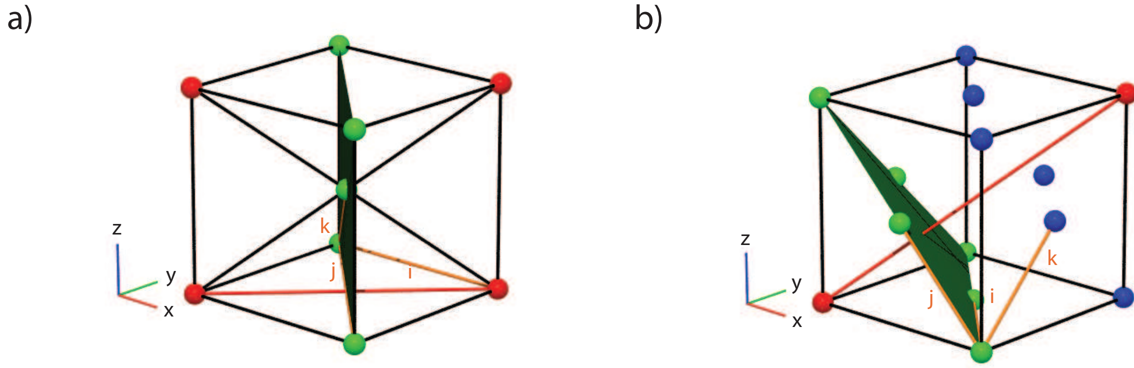

Figure A.2 a) Visualization of the bcc 110 ijk vectors (in orange). b) ijk for the fcc 111 Au model.

A.3 Construction of a fcc 111 oriented cube

The Au surface was constructed in a similar way. As base vectors the author chose

$$\overrightarrow{i} = (-0.5, 0.5, 0) \quad \text{(A.9)}$$

$$\overrightarrow{j} = (-0.5, 0, 0.5) \quad \text{(A.10)}$$

$$\overrightarrow{k} = (0, 0.5, 0.5) \quad \text{(A.11)}$$

Since the fcc 111 layers are stacked in an ABCA fashion, we obtain

$$a_{Au} * |(1, 1, 1)|/3 = a_{Au} * \sqrt{3}/3 \simeq 0.24 \text{ nm} \quad \text{(A.12)}$$

as layer spacing – see figure A.2 b).

A.4 Tilt for a W(111) one atom tip

As an addition to figure 3.14 that showed the effect of a relative tilt of tip and sample for a three atom tip structure, here the situation for a tip which is terminated by one atom is demonstrated in figure A.3.

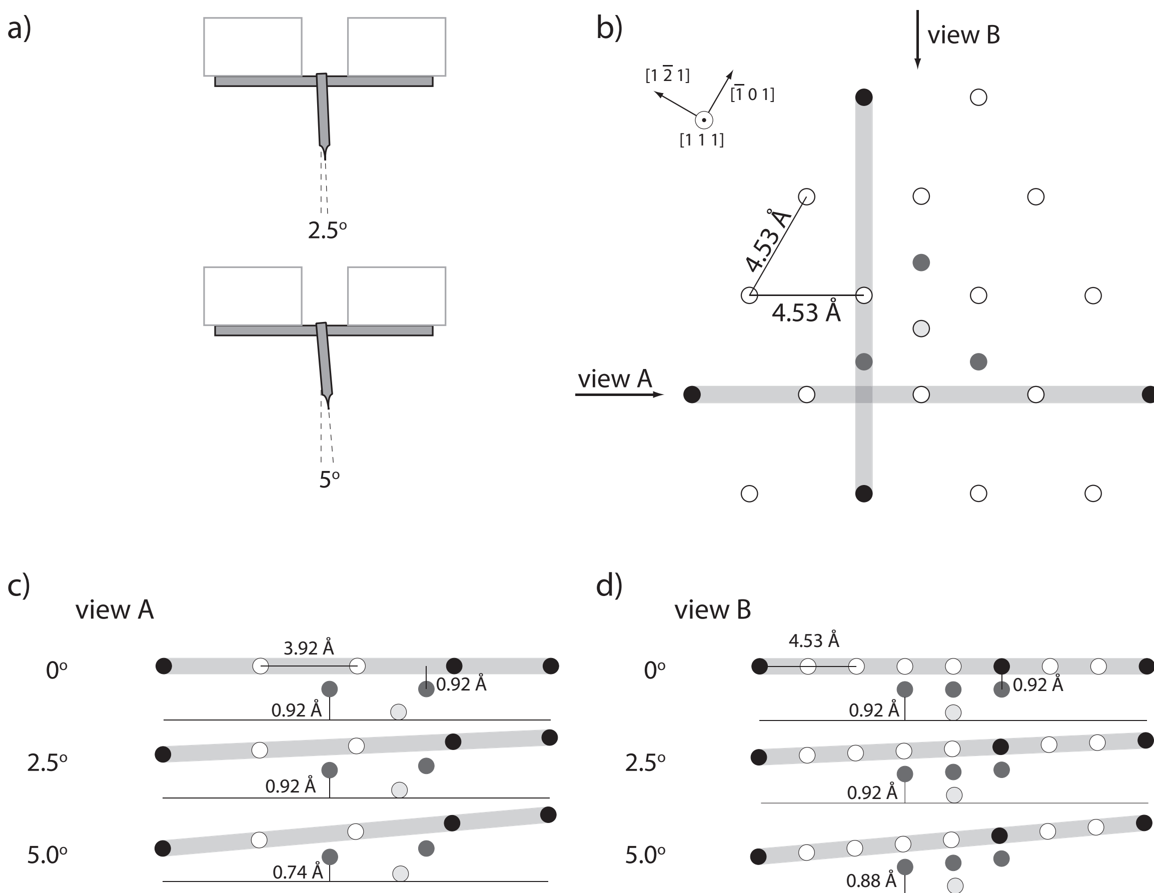

Figure A.3 a) Tilt of the wire cross versus the perfect perpendicular orientation. b) The first three layers of a one atom tip reconstruction. The tip atom is drawn in yellow, the three atoms of the second layer in red and the third layer in black and white – compare with fig. 3.10 and fig. 3.14. c) Side view A of the structure shown in b). The solid line represents a perfectly flat sample. Distances of corner atoms to the sample for different tilts are given. d) Side view B of the structure shown in b) with atom-sample distances.

APPENDIX B

Electric Field and Electrostatic Force for two geometries

In this section the electric field and the potential of a nano-tip in the FIM and STM configuration will be described in two useful coordinate systems. The first being prolate spheriodal coordinates, which have been used to project the trajectories of electrons in a FIM setup by Russel [118] and to describe the electrostatic force in SPM configurations by Patil et. al. [119]. As it turns out this geometry cannot be applied to the configuration that is used for the SPM measurements in this thesis since the description with prolate spheriodal coordinates does not represent the situation for tip–sample distances smaller than four times the tip radius, but it is discussed in order to describe the electric field between tip and sample during FIM operation and might be useful for future investigations of FIM image features.

The second coordinate system is a geometry that treats the tip as a cone that is capped with a sphere and has been derived by Hudlet et. al. [71]. Both derivations can be found in the full version in [119] and [71]. Some details given here are steps in the derivation that were not mentioned explicitly in the original derivations and are useful if one wants to follow the whole derivation in detail.

The assumption that both models are based on is the fact that the tip surface is smooth and that the actual shape is closely related to the assumed model shape. For tips that are electrochemically etched and annealed afterwards this model is a good approximation when looking at SEM images of tips that have been used for the experiments described in this work. Another fact that supports this approach is the fact that we have to treat

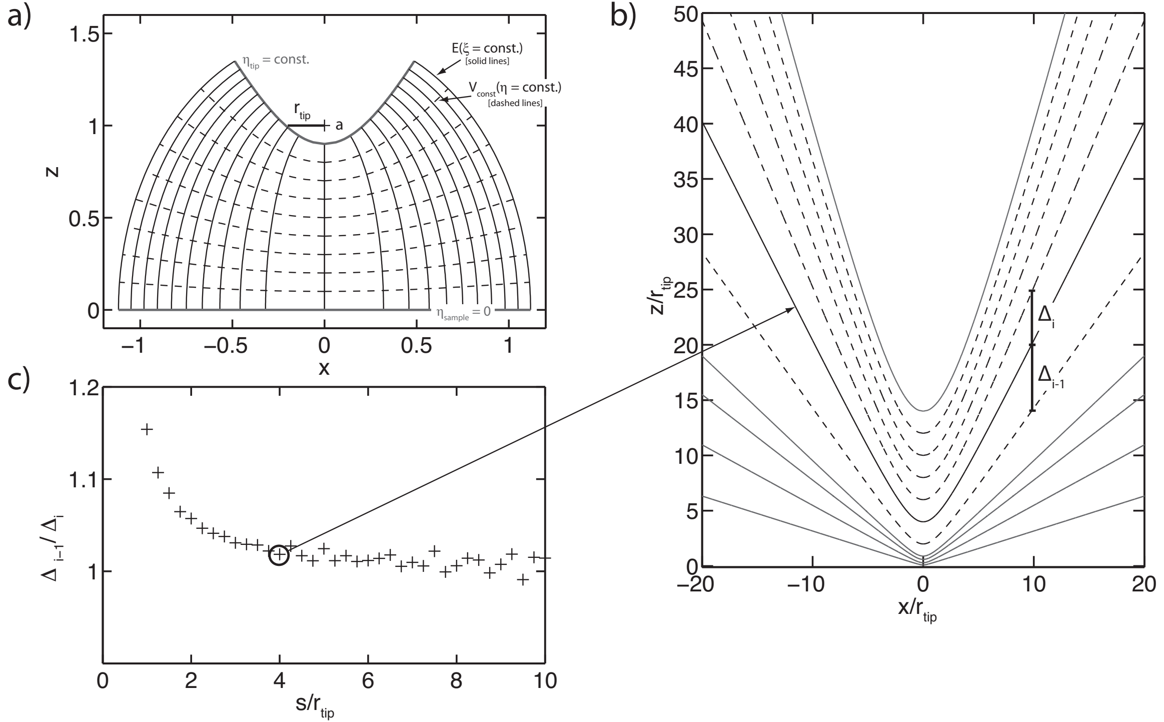

Figure B.1 a) The electric field and equipotential lines for a hyperbolid geometry. The tipshape is given by a constant η_{tip}, the sample by $\eta_{sample} = 0$. Lines of constant ξ represent the electric field lines and lines of constant η equipotentials. b) The tip shape is not maintained for small tip-sample distances. The tip shape diverges at a tip-sample distance of $s = 4\,r_{tip}$. (The blue shapes are not separated by a constant distance increment. All other curves are.) c) A plot of differences of z(x=10 r_{tip}) for consecutive plots with equal spacing in s – see indication in b). The differences become very similar for distances with $s \geq 4r_{tip}$.

the electrostatic force as long range force, meaning that for small tip–sample distances, where atomic corrugations become important, chemical forces will dominate the overall force. Hence, the electrostatic force does not have to be accurate up to atomic details and it is a good approximation to assume a smooth tip surface on the mesoscopic scale.

B.1 Prolate Spheriodal Coordinates

The transformation from prolate spheriodal coordinates to cartesian ones is given by:

$$x = a[(\xi^2 - 1)(1 - \eta^2)]^{1/2} \cos\phi \qquad \text{(B.1)}$$

$$y = a[(\xi^2 - 1)(1 - \eta^2)]^{1/2} \sin\phi \tag{B.2}$$

$$z = a\xi\eta \tag{B.3}$$

with $1 \leq \xi \leq \infty$, $-1 \leq \eta \leq 1$ and the angle around the z axis $0 \leq \phi \leq 2\pi$. Figure B.1 a) shows a plot of the tip-sample geometry in prolate spheriodal coordinates. The advantage of this coordinate system becomes obvious once we look at the plot. Lines of constant ξ display the electric field lines and lines of constant η display equipotentials. The line for $\eta = 0$ is a straight line along $z = 0$ and is conveniently chosen as STM sample or FIM screen representation. Any constant η value that resembles the tip structure can be chosen as η_{tip}. It is useful to obtain a quantitative equation for the potential dependence on the distance in terms of η. Therefore we have to solve the Laplace equation in prolate spheriodal coordinates:

$$\nabla^2\psi = 0 \tag{B.4}$$

$$\nabla^2 = \frac{1}{a^2(\xi^2 - \eta^2)}\left\{\frac{\partial}{\partial\xi}\left[(\xi^2 - 1)\frac{\partial}{\partial\xi}\right] + \frac{\partial}{\partial\eta}\left[(1 - \eta^2)\frac{\partial}{\partial\eta}\right]\right\} + \frac{1}{a^2(\xi^2 - 1)(1 - \eta^2)}\frac{\partial^2}{\partial\phi^2} \tag{B.5}$$

since we are looking for equipotential lines, there will be no dependence on ξ and ϕ and we have to consider only the variation with η:

$$\nabla^2\psi(\eta) = \frac{1}{a^2(\xi^2 - \eta^2)} + \frac{\partial}{\partial\eta}\left[(1 - \eta^2)\frac{\partial\psi(\eta)}{\partial\eta}\right] = 0 \tag{B.6}$$

Doing an integration with respect to η twice (details in [118]) and using $\eta_{sample} = 0$, $V(\eta_{tip}) = V_t$ and $V(\eta_{sample} = 0) = 0$ we obtain:

$$V(\eta) = \alpha \ln\left[\frac{1 + \eta}{1 - \eta}\right] \tag{B.7}$$

with

$$\alpha = \frac{V_t}{\ln\left[\frac{1+\eta_{tip}}{1-\eta_{tip}}\right]} \tag{B.8}$$

Following the derivation in Patil [119] now, we obtain the electric field by:

$$\mathbf{E} = -\vec{\nabla} V(\eta) \tag{B.9}$$

where

$$\vec{\nabla} = \frac{\mathbf{n}_\xi}{h_\xi}\frac{\partial}{\partial \xi} + \frac{\mathbf{n}_\eta}{h_\eta}\frac{\partial}{\partial \eta} + \frac{\mathbf{n}_\phi}{h_\phi}\frac{\partial}{\partial \phi} \tag{B.10}$$

with the unit vectors $\mathbf{n}$, and the scaling factors h:

$$h_\xi = a[(\xi^2 - \eta^2)/(\xi^2 - 1)]^{1/2} \tag{B.11}$$

$$h_\eta = a[(\xi^2 - \eta^2)/(1 - \eta^2)]^{1/2} \tag{B.12}$$

$$h_\phi = a[(\xi^2 - 1)/(1 - \eta^2)]^{1/2}. \tag{B.13}$$

We know from equation (B.7) that the potential varies with η only. Therefore we continue with:

$$\vec{\nabla}_\eta V(\eta) = \frac{\alpha \mathbf{n}_\eta}{a}\sqrt{\frac{(\xi^2 - \eta^2)}{(1 - \eta^2)}}\frac{\partial}{\partial \eta} \ln\left(\frac{1+\eta}{1-\eta}\right). \tag{B.14}$$

Using $\partial \ln x/\partial x = 1/x$ and the chain rule plus $(u/v)' = (u'v - uv')/v^2$, we obtain an expression for the electric field:

$$\mathbf{E}(\eta, \xi) = \frac{2\alpha \mathbf{n}_\eta}{a}[(\xi^2 - \eta^2)(1 - \eta^2)]^{-1/2} \tag{B.15}$$

In order to calculate the force for this electric field along the z axis we have to integrate

$$d\mathbf{F}_z = dq(\mathbf{E} \cdot \mathbf{n}_z) \tag{B.16}$$

with the surface charge $dq = \sigma_p \epsilon_0 (\mathbf{n}_\eta \cdot \mathbf{E}) = \sigma_p dA$. σ_p is the surface charge at a point p on the surface of the tip ($\eta = \eta_{tip}$). The surface element dA at constant η is

$$dA = h_\xi h_\phi d\xi d\phi = a^2[(\xi^2 - \eta^2)(1 - \eta^2)]^{1/2} d\xi d\phi. \tag{B.17}$$

For a full ring around the z axis ($0 \leq \phi \leq 2\pi$) we obtain

$$dA = 2\pi a^2[(\xi^2 - \eta^2)(1 - \eta^2)]^{1/2} d\xi \tag{B.18}$$

through integration. Using all the above, we obtain an expression for the force:

$$dF_z = 8\pi a^2 \epsilon_0 [(\xi^2 - \eta^2)(1 - \eta^2)]^{-1/2} (\mathbf{n}_{\eta_{tip}} \cdot \mathbf{n}_z) d\xi. \tag{B.19}$$

This can be integrated from $\xi = 1$ to $\xi = \xi_{max}$ (for details see [119]) in order to get:

$$F_z = 4\pi a^2 \epsilon_0 \ln \left[\frac{\xi_{max}^2 - \eta_{tip}^2}{1 - \eta_{tip}^2} \right] \tag{B.20}$$

We need to define a ξ_{max} as cutoff since the Force does not converge with growing ξ. A maximum radius can be defined in dependence of ξ, meaning the x value for $\phi = 0$, $\xi = \xi_{max}$:

$$r_{max}(\xi) = a[(\xi_{max}^2 - 1)(1 - \eta_{tip}^2)]^{1/2} \tag{B.21}$$

$$\tag{B.22}$$

Using

$$z(\xi = 1, \eta = \eta_{tip}) = a\eta_{tip} = s \tag{B.23}$$

$$z(\xi = 1/\eta_{tip}, \eta = \eta_{tip}) = a \tag{B.24}$$

$$\tag{B.25}$$

we get

$$x(\xi = 1, \eta = \eta_{tip}, \phi = 0) = a[(\frac{1}{\eta_{tip}^2} - 1)(1 - \eta_{tip}^2)]^{1/2} = r_{tip} \tag{B.26}$$

$$= \frac{a}{\eta_{tip}} - a\eta_{tip} \tag{B.27}$$

which can be written as using eq (B.23):

$$a = \sqrt{s(s + r_{tip})} \tag{B.28}$$

$$\eta_{tip} = \sqrt{s/(r_{tip} + s)}. \tag{B.29}$$

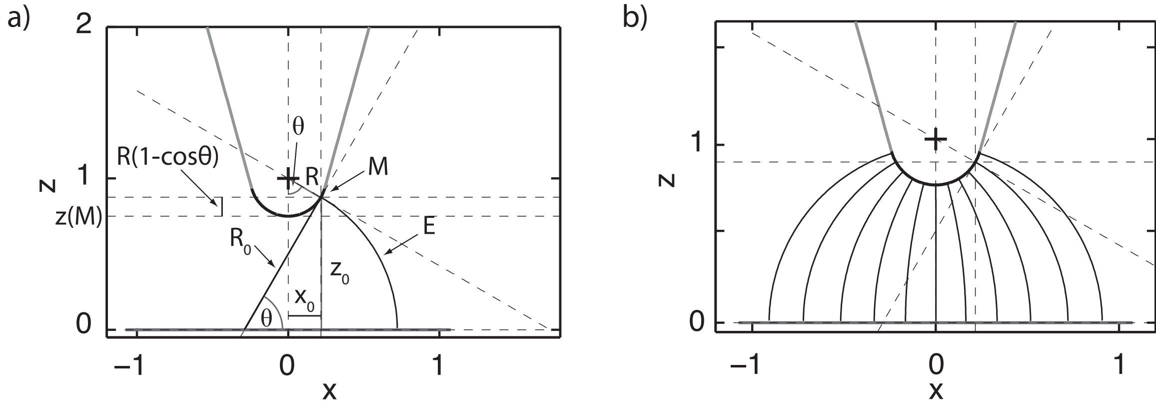

Figure B.2 a) Sphere-cone model for the tip shape. The cone part is drawn in red and the spherical cap in blue. An example for a field line is given in blue. The related parameters are also shown. See text for details. b) The shape of the electric field in this geometry.

Substituting (B.28) and (B.29) into (B.20) leads to:

$$F_z(s) = 4\pi\epsilon_0 V_t^2 \left[\frac{\ln[1 + (r_{max}/r_{tip})^2(1 + r_{tip}/s)]}{\ln^2(\frac{1+\eta_{tip}}{1-\eta_{tip}})} \right]. \tag{B.30}$$

We can see from figure B.1 b) and c), defining the tip shape through eq. (B.29) will have an effect on the tip shape for tip sample distances smaller than $4r_{tip}$. Then the shape diverges towards a larger opening angle. Another difference between the two models is that the distance dependence is logarithmic in the hyperbolid case. That model has some agreement with measurements of the electric force for large distances as shown in [119]. But for SPM measurements of atomic interactions at small tip-sample gaps it cannot be used. The approach is very useful to describe the electron/field ion trajectories in a FE/FIM setup, in which case $s \gg r_{tip}$, as shown by Russel et. al. [118].

B.2 Sphere-Cone geometry

The electric field E can be described by:

$$E = -\frac{V}{l(M)} \tag{B.31}$$

with the potential difference V between tip and sample and the field line length l corresponding to a point M on the tip surface. As indicated in figure B.2 a) any field line in this geometry can be described by a circle with radius R_0. Defining

$$z_0(M) = z(M) + R\,(1 - \cos\theta) \tag{B.32}$$

$$\theta = \frac{l(M)}{R_0(M)} \tag{B.33}$$

and using

$$\sin\theta = \frac{z(M) + R\,(1 - \cos\theta)}{R_0} \tag{B.34}$$

we obtain an expression for the length of a field line at point M:

$$l(M) = \frac{\theta[z + R\,(1 - \cos\theta)]}{\sin\theta} \tag{B.35}$$

For the field lines of the cone part the expression for z_0 has to be changed correspondingly. But as we will see later on, for small tip–sample gaps the spherical cap is dominating the interaction. Now the spherical contribution can be calculated. The details of the calculation for a sphere and a cone combined with a spherical cap can be found in a paper of Hudlet et. al. [71]. Using a notation of Guggisberg et. al. [72], we obtain a form of the electric force that has been used by many groups now and showed good agreement with experimental data for usual SPM tip-sample distances:

$$F_{el} = -\pi\epsilon_0(V_t - V_C)^2 \left\{ \frac{R}{s} + k(\alpha)^2 \left(\ln\left(\frac{L}{s + R_\alpha} \right) - 1 \right) - \frac{R[1 - k(\alpha)^2 \cos^2(\alpha/\sin(\alpha))]}{s + R_\alpha} \right\} \tag{B.36}$$

with tunneling bias voltage V_t, contact potential V_C, tip radius R, tip sample distance s, cone opening angle α, $k(\alpha) = 1/\ln(\cot(\alpha/2))$, tip length L ($\gg s$) and $R_\alpha = R(1 - \sin(\alpha))$. As shown in chapter 4.1.1, an approximation that only takes the spherical contribution into account

$$F_{el} = -\pi\epsilon_0(V_t - V_C)^2 \frac{R}{s} \tag{B.37}$$

describes the situation well.

B.3 Finite Element Analysis of the Electric Field in FIM

In order to estimate the field distribution in the actual microscope during FIM operation, the geometry of the apparatus was approximated in cylindrical symmetry and then calculated in Poisson Superfish [120] with finite element methods. The result is illustrated in figure B.3 showing the equipotentials as black solid lines. Due to time constraints the tip has been representes by a sphere with a radius of 1 mm and the rest of the apparatus in its real dimensions, which can be found in [30]. Since the tip in the real setup was six orders of magnitude smaller than the setup dimensions a more sophisticated mesh would have been needed in order to obtain a conversion for these dimensions. Another deviation of this approach is that the real three dimensional structure does not have cylindrical symmetry. Nevertheless in this simulation the bending effect of the interferometer plates that confine the path of the He ions from the tip to the multichannel plate on the equipotentials is noticeable in this approximation.

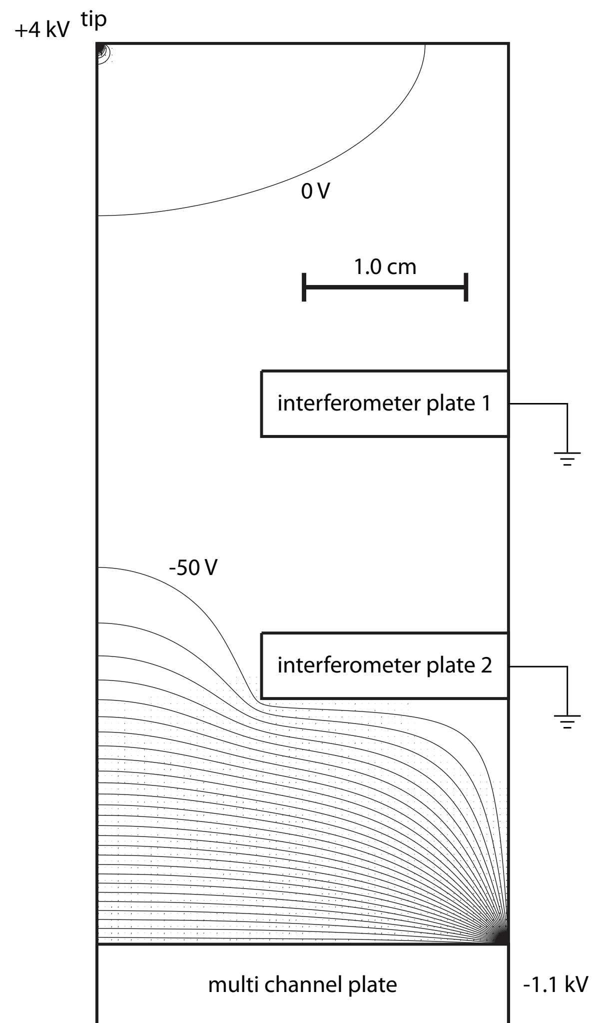

Figure B.3 Finite element modeling with Poisson Superfish [120]. The tip radius is set to $r_{tip} = 1$ mm and the voltage to $V_{tip} = 4$ kV. The multichannel plate was set to $V = -1.1$ kV.

APPENDIX C

New SPM Coarse Approach

Before an STM experiment can be started, one has to bring the tip close enough to the sample so that the tip-sample gap can be controlled by the piezo tube extension. The piezo tube used in this thesis has a range of 800 nm. In order to bring the tip in the piezo range, a step motor is used, the so called coarse approach. SPM groups use different designs, a summary of the predominant designs in the 1980s can be found in [121], more recent designs can be found in [122], [123], [124].

For the experiments in this thesis a new coarse approach has been designed and implemented by the author in close collaboration with Yoichi Miyahara. The design is using a hexagon that is moved by piezo stacks and pressed into contact by a leaf spring. Figure C.1 shows the actual device in an exploded view. This version has been used for five years up until now and has operated reliably. If the system is cooled with liquid nitrogen, about every fourth cooling cycle the leaf spring has to be retightened due to the thermal expansion and contraction of the device.

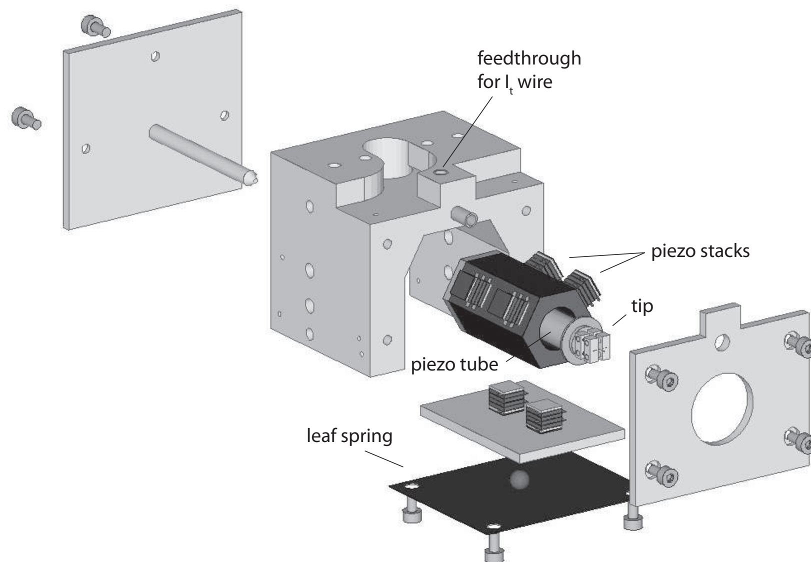

Figure C.1 New STM coarse approach.